Spin squeezing in Bose-Einstein condensates

Yun Li

Yun Li. Spin squeezing in Bose-Einstein condensates. Atomic Physics [physics.atom-ph]. Ecole Normale Supérieure de Paris - ENS Paris, 2010. English. NNT : . tel-00506592

HAL Id: tel-00506592

https://theses.hal.science/tel-00506592

Submitted on 28 Jul 2010

Thèse de Doctorat de
l'Université Pierre et Marie Curie

Spécialité : Physique Quantique

présentée par

Mlle. Yun LI

pour obtenir le grade de

Docteur de l'Université Pierre et Marie Curie

États comprimés de spin dans un condensat de Bose-Einstein

~

Spin squeezing in Bose-Einstein condensates

---

soutenue le 06 juillet 2010 devant le Jury composé de :

M.	Claude FABRE	Président du Jury
M.	Markus OBERTHALER	Rapporteur
M.	Li YOU	Rapporteur
Mlle.	Isabelle BOUCHOULE	Examinatrice
Mme.	Alice SINATRA	Directrice de thèse
M.	Weiping ZHANG	Directeur de thèse
Mme.	Yanling XUE	Examinatrice

University Code 10269

Student Number 52060602027

華東師範大學

East China Normal University

Spin squeezing in Bose-Einstein condensates

玻色–爱因斯坦凝聚中的自旋压缩

Department: Department of Physics
Major: Optics
Field: Atom Optics
Supervisor: Weiping Zhang & Alice Sinatra
Student: Yun Li

Completed in May, 2010

Spin squeezing in Bose-Einstein condensates

Yun Li

Abstract

Spin squeezed states are multi-particle entangled states that have practical interest in quantum metrology and atomic interferometer. In this thesis, we study theoretically realistic schemes for the production of spin squeezed states using the coherent interactions between cold atoms in a bimodal Bose-Einstein condensate. In particular, we include decoherence process such as particle losses, as well as spatial dynamics which limit the maximum squeezing reachable in a real experiment. We find that the effect of losses cannot be neglected as soon as the lost fraction of particles is of the order of the squeezing parameter. The analytical solution that we find, using Monte-Carlo wave functions approach, allows us to perform an optimization for the spin squeezing with respect to the experiment parameters. The method that we develop to study the entangled spatial and spin dynamics of interacting bimodal BEC allows a full analytical treatment for spin squeezing in some cases and can be used in the general case without the need of heavy numerics. We apply our theoretical studies to an experiment for spin squeezing recently realized successfully on an atom chip. Finally, we study the spin squeezing in a related but different system of a BEC with two external modes coherently coupled by the tunnel effect. We study this problem with a dynamical two-mode model for $T \ll T_c$ and within a multimode approach in thermal equilibrium for $T \gtrsim T_c$.

Keywords: Bose-Einstein condensates, spatial dynamics and the phase of the condensates, spin squeezing, quantum metrology, entangled states, decoherence

Résumé

Les états comprimés de spin sont des états intriqués qui ont intérêt pratique dans la métrologie quantique et l'interférométrie atomique. Dans cette thèse, nous étudions théoriquement les schémas réalistes pour la production des états comprimés de spin utilisant l'interaction cohérente entre les atomes froids dans un condensat de Bose-Einstein bimodal. En particulier, nous incluons les processus de décohérence tels que les pertes de particules, ainsi que la dynamique spatiale, qui limitent la compression maximale accessible dans une expérience réelle. Nous trouvons que l'effet des pertes ne peut être négligé dès que la fraction de particules perdue est de l'ordre du paramètre de compression. La solution analytique que nous trouvons, en utilisant des fonctions d'onde Monte-Carlo, nous permet d'effectuer une optimisation pour la compression de spin en ce qui concerne les paramètres de l'expérience. D'autre part, nous avons développé une méthode pour étudier la dynamique spatiale et la dynamique de spin intriquées dans un condensat bimodal, ce qui permet un traitement complet analytique dans certains cas, et peut être utilisée dans le cas général, sans nécessiter de calculs numériques lourds. Nous appliquons nos études théoriques à une expérience de compression de spin récemment réalisée avec succès sur une puce à atomes. Enfin, nous étudions la compression de spin dans un système lié mais différent d'un BEC avec deux modes spatiaux couplés de façon cohérente par effet tunnel. Nous étudions ce problème avec un modèle dynamique à deux modes pour $T \ll T_c$ et avec une approche multimode à l'équilibre thermique pour $T \gtrsim T_c$.

Mots clés: Condensats de Bose-Einstein, dynamique spatiale et de phase des condensats, compression de spin, métrologie quantique, états intriqués, décohérence

摘要

自旋压缩态是一个多体纠缠态，它对于原子干涉仪，精密光谱测量以及量子信息有着重要意义。本文研究了双模冷原子（玻色-爱因斯坦凝聚）中自旋压缩的产生。压缩的机制是依靠冷原子之间的弹性相互作用。在实际实验中，伴随这一作用同时存在的其它因素，诸如退相干效应，凝聚体模式的集体激发（空间动力学）等，将严重影响着最终获得的自旋压缩量。为符合实际实验情况，在研究中我们考虑了由粒子损失导致的退相干效应，以及冷原子的空间动力学对于压缩量的影响。我们发现，当粒子损失的百分比与压缩参数可比拟时，粒子损失带来的效应不可忽略。通过运用波函数蒙特-卡洛方法，我们得到了一个能够定量描述粒子损失对于自旋压缩影响的解析表达式，它使我们能够对实验参数进行优化，以逼近可获得的最大压缩极限。另一方面，我们发展了一套半解析方法，用于研究压缩过程中相互关联的自旋动力学与外部空间空力学。这一方法使得原本为计算相应结果所依赖的庞大数值模拟得以大大简化。在某些特殊情况下，我们的方法甚至可以得到完全解析的理论结果。我们将理论研究应用于实际情况，并在最近实现的原子芯片上的自旋压缩实验中取得了成功。最后，我们研究了另一种与自旋压缩有关的冷原子系统，冷原子的两个自旋分量由两个外部的空间模式构成，它们通过隧穿效应相干偶合。在 $T \ll Tc$ 的低温条件下，基于双模模型我们计算了该系统可获得的自旋压缩量；而在 $T \gtrsim Tc$ 的高温区域，我们研究了该系统在巨正则系宗下跟自旋压缩相关的平衡态统计性质。

关键词：玻色-爱因斯坦凝聚，空间动力学与凝聚体相位，自旋压缩，量子测量，纠缠态，退相干

Contents

Chapter 1

Introduction

A Bose-Einstein condensate (BEC) as originally predicted by Bose and Einstein [1, 2], is a state of matter in which a large number of bosons, when cooled to temperatures such that $n\lambda_{dB} \gtrsim 1$ (with n the atomic density and $\lambda_{dB} = \sqrt{2\pi\hbar^2/Mk_BT}$ the thermal de Broglie wavelength), condense in a single quantum mechanical state. The quantum effects then become apparent on a macroscopic scale.

Since the first achievement of BEC in atomic gases in 1995 [3, 4, 5], a new chapter has been opened in atomic physics. For a number of years, Bose-Einstein condensates have proven to be powerful in exploring a wide range of questions in both fundamental physics and applications. Such examples include the observation of interference of two independent condensates [6, 7], long-range phase coherence [8], four-wave mixing for the atomic field [9], superradiance [10], amplification [11, 12], atom laser [13, 14], dark and bright solitons [15, 16, 17, 18], and quantized vortices and vortex lattice [19, 20, 21]. Common to all of these phenomena is the existence of a coherent macroscopic matter wave analogous to the laser field for light, opening up the field of coherent atom optics [22]. Various potential applications have been identified such as interferometry and frequency standards, detection of inertial effects and a host of related technological tasks.

Unlike the photons in quantum optics that do not interact in the absence of a nonlinear medium, interactions in BEC furnish natural nonlinearities to the atomic field, which provide a useful tool to produce nonclassical states, such as spin squeezed states [23] or Schrödinger cat-like states [24, 25]. These multi-particle entangled states [26] can be created in BEC in analogy to the nonclassical states of light created by the Kerr effect in quantum optics. Exploring the possibility of using quantum-mechanical entanglement to improve the precision of atomic interferometer has been one of the most interesting research topics for many years [27, 28, 29]. First evidences of nonclassical atomic states with BEC were obtained in [30, 31].

At low temperatures in the mean-field picture, the interaction potential energy for each atom is determined by the density and a single atomic parameter, the s-wave scattering length a. The remarkable facts is that in cold atoms experiments, one can tune the interactions in a controllable way. By applying an external magnetic field with the help of so-called Feshbach resonances [32], the scattering length can be modified within a wide range, from negative to positive. On the other hand, the fact that the atomic matter waves can, to a large extent, be manipulated in space provides an alternative way besides Feshbach resonances to tune the interactions. By changing the trapping potential, one can modify the density distribution, as well as the dimension of space resulting in a change of the effective scattering length [33].

In the context of this thesis, we address the problem of producing spin squeezed states in Bose-Einstein condensates by using the atomic elastic interactions. The original motivation is to use these cold atomic samples in quantum metrology and high precision spectroscopy to overcome the standard quantum limit [29, 34]. The first proposal for achieving spin squeezing in a bimodal BEC was given by [23], in which it was shown that squeezing will be created with a rate scaling as $a_{aa} + a_{bb} - 2a_{ab}$, where a_{ij} is the scattering length describing the interaction of an atom in state i and an atom in state j. According to the predictions of a simple two-mode model, a large amount of spin squeezing can be obtained with this scheme. However, there still remained two fundamental problems to be solved. The first is related to decoherence processes such as inelastic interactions always present in a real experiment. The fundamental limit to spin squeezing set by particle losses was not known in the literature. The second is how the spatial degrees of freedom, which are not taken into account in the two-mode model, affect the squeezing in a situation in which the dynamics is significantly excited. This happens in general when the mean-field seen by the atoms is greatly changed concomitantly with the origination of spin dynamics, for example in the case of sudden spatial separation of the two previously overlapped components of a bimodal BEC with large atom number. Therefore, one would desire an efficient model which calculates squeezing while accounting for this dynamics.

In the first half of this thesis, we will show our solutions to these two problems. In chapter 2 we review the basic theory of spin squeezing in the framework of a two-mode model, and the state of the art for achieving spin squeezing in atomic systems. The work described in chapter 3 concerns the production of spin squeezed states in a bimodal BEC in presence of one, two and three-body losses [35, 36]. The investigation is linked to the fragility of the entangled state due to losses relevant to metrology. We show that this problem is analytically solvable within the two-mode model after some approximations. In some cases, one can carry out analytically an optimization to approach the ultimate spin squeezing obtainable in presence of particle losses. We also consider the survival of squeezing after the nonlinearity is "switched off". In this case, the squeezing is only affected by the losses. Very recently, the entanglement lifetime in a squeezed atomic clock has been studied experimentally [37]. In chapter 4 we will address the problem of spatial dynamics. We develop a semi-analytical method to study the entangled spin and spatial dynamics of interacting bimodal BEC [36]. For some particular cases even a full analytical expression giving a physical insight of these effect can be obtained with our approach. The theoretical treatment we developed enabled us to calculate efficiently the maximum spin squeezing achievable in experimentally relevant situations with Sodium or Rubidium bimodal condensates, including the effect of spatial dynamics, and of one, two and three-body losses, which we do in chapter 5.

Since 2009, we started to collaborate with the experimental group of P. Treutlein in Munich on a project to achieve the spin squeezed state on an atom chip using a condensate of ^{87}Rb in two internal states whose wave function can be selectively manipulated. The states used for squeezing $|F = 1, m_F = -1\rangle$ and $|F = 2, m_F = 1\rangle$ can also be used in an atomic clock [38, 39] so that the spin squeezing would find naturally its application there. The result of the experiment shows the first realization of spin squeezed state with Bose-Einstein condensates on an atom chip [40]. Simultaneously spin squeezing in a bimodal BEC was observed using a Feshbach resonance in an optical trap [41]. We expose in chapter 6 the theoretical part of this work, giving the physical explanation of the observed squeezing signals.

Another possibility to achieve spin squeezed states, using two external modes instead of two internal states, is to coherently split a condensate in a double well potential [42]. A corresponding experiment using an atom chip is carried out in our group in Paris directed by J. Reichel [43]. We present our theoretical work on this project in chapter 7. At low temperature regime ($T \ll T_c$), we calculate the obtainable spin squeezing based on two-mode model with the experimental parameters. For the regime $T \gtrsim T_c$, we study the crossover from sub- to super-Poissonian fluctuations observed in the experiment with a thermal equilibrium approach in a grand canonical ensemble. Finally, conclusions and outlook will be given in chapter 8.

Chapter 2

Basic theory for spin squeezing

In this chapter, we give a basic introduction to spin squeezing within a very simple two-mode model. We will briefly describe how this model applies to the case of a bimodal Bose-Einstein condensate.

2.1 General introduction on spin squeezing

2.1.1 The Spin squeezing parameter

The concept of spin squeezing was firstly introduced by Kitagawa and Ueda [44], generalizing to spin operators the idea of squeezing developed in quantum optics. A system which contains N particles in two orthogonal modes $|a\rangle$ and $|b\rangle$ can be considered as a $N/2$ spin system. The collective spin operators (sum of the individual spin-1/2 of each atom) can be defined as

$$S_x = \frac{1}{2}\sum_i \left(|b\rangle\langle a|_i + |a\rangle\langle b|_i\right); \tag{2.1}$$

$$S_y = \frac{i}{2}\sum_i \left(|b\rangle\langle a|_i - |a\rangle\langle b|_i\right); \tag{2.2}$$

$$S_z = \frac{1}{2}\sum_i \left(|a\rangle\langle a|_i - |b\rangle\langle b|_i\right). \tag{2.3}$$

The commutation relations between the operators, S_x, S_y and S_z, are the same as the angular momentum ones $[S_i, S_j] = i\epsilon_{ijk} S_k$, where $i, j, k = x, y, z$ and ϵ_{ijk} is the Levi-Civita symbol. Physically S_z represents the population difference between the two spin components, while S_x and S_y give the coherence between the two components. The uncertainty relations between the three orthogonal spin components can be written as

$$\Delta S_i \Delta S_j \geqslant \frac{1}{2} | \, [S_i, S_j] \, | = \frac{1}{2} | \langle S_k \rangle | \, . \tag{2.4}$$

Consider an eigenstate of the operator S_x with the eigenvalue $N/2$,

$$|S_x = N/2\rangle = \frac{1}{\sqrt{N!}} \left(\frac{a^\dagger + b^\dagger}{\sqrt{2}} \right)^N |\mathrm{vac}\rangle \tag{2.5}$$

where operators $a^\dagger$ and $b^\dagger$ create a particle in the states a and b respectively. In this case $\Delta S_x^2 = 0$, and the transverse components, S_y and S_z have a nonzero variance,

$$\Delta S_z^2 = \Delta S_y^2 = N/4 \tag{2.6}$$

satisfying the uncertainty principle (2.4). For this particular state, the variance is evenly distributed in the perpendicular plane (yz-plane) to the mean spin. Rewriting Eq.(2.6) for the z component, one finds

$$\langle S_z^2 \rangle = \sum_{j,l} \langle s_{zj} s_{zl} \rangle = \sum_j \langle s_{zj}^2 \rangle + \sum_{j \neq l} \langle s_{zj} s_{zl} \rangle = \frac{N}{4} \, . \tag{2.7}$$

The first term is simply the sum of the variances of the individual spins equal to $N/4$. The second term is zero, meaning that there is no correlation between the individual spins.

As the two spin components in state (2.5) have a well defined relative phase, such state is also referred as coherent spin state (CSS), or phase state. The state can be illustrated as in Fig.2.1 (a). Each individual spin is aligned along axis-x, and the components orthogonal to x are completely random, having a variance of $1/4$. If appropriate correlations are established among the individual spins, it is possible to partly cancel out fluctuations in one direction at the expense of enhancing them in the orthogonal direction. Then quantum noise is redistributed in the plane orthogonal to the mean spin, as illustrated in Fig.2.1(b).

We say that state is spin squeezed if the variance of one spin component orthogonal to the mean spin vector is smaller than the standard quantum limit (SQL), i.e. $|\langle S_k \rangle|/2$. More precisely, we can define a squeezing parameter [29],

$$\xi^2 = \frac{N \Delta S_{\perp,\,\mathrm{min}}^2}{\langle S \rangle^2} \tag{2.8}$$

where $S_\perp$ represents the spin component in the plane orthogonal to the mean spin, and $\Delta S_{\perp,\,\mathrm{min}}^2$ is the minimum of the variance in this plane. When

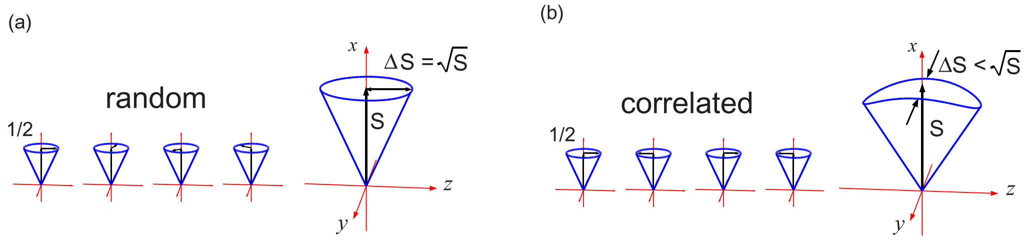

Figure 2.1: Schematic illustrations of $N/2$ spins system. (a) Coherent spin state in which all N individual spins are aligned along x with no correlations between them. (b) Squeezed spin state in which the individual spins are correlated, reducing the fluctuation of one component transverse to the mean spin below the standard quantum limit.

$\xi^2 < 1$, the state is referred as spin squeezed state (SSS). As clear from (2.7) spin squeezing implies correlations among the atoms. As we shall see, the definition (2.8) is also directly connected to the reduction of projection noise in Ramsey spectroscopy [45].

2.1.2 Spin squeezing for quantum metrology

Spin squeezed states have practical interest in atom interferometry, and high precision spectroscopy [29, 28]. In spectroscopy, we want to measure the transition frequency between two internal states. And this is done by measuring the accumulated relative phase difference between the two states during a free precession time.

As illustrated in Fig.2.2, a typical Ramsey spectroscopy experiment consists in the following steps: (a) at the beginning, all the atoms are prepared in one of the internal states, for example a. On the Bloch sphere, the state can be described as a vector pointing to the pole. (b) we apply a $\pi/2$-pulse to create a CSS. It is equivalent to rotate the state around axis-y from the pole to the equatorial plane. (c) the system evolves freely for some interrogation time T, during which the mean spin rotates around axis-z, and the atomic states accumulate a relative phase; (d) another $\pi/2$-pulse is applied. It convert the relative phase into population difference. Finally, the population difference between the two states, i.e. $\langle S_z \rangle$, is read out. Steps (a)-(d) can be described by the unitary transformation

$$U(T) = e^{-i\pi/2 S_y} e^{-i\omega T S_z} e^{-i\pi/2 S_y} \tag{2.9}$$

where ωT is the accumulated phase during the interrogation time T. The

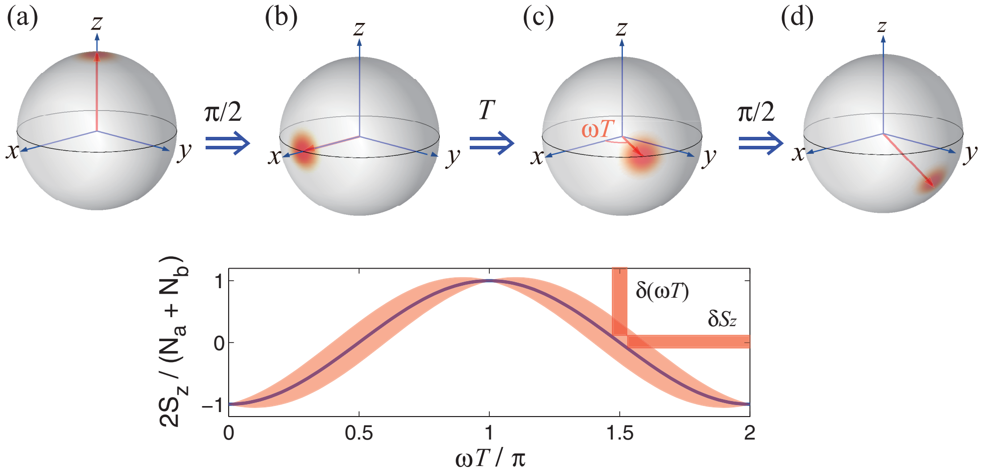

Figure 2.2: (Top) Illustration of the Ramsey sequence on the Bloch sphere. The red (blue) arrow represents the direction of the mean spin in present (previous) step. (a) All the atoms are initially prepared in state a, therefore the state vector $\hat{S}$ points along z direction. (b) A $\pi/2$-pulse rotates the state vector into the equatorial plane, where each atom is in the superposition state. (c) During the interrogation time, the relative phase between the two states is accumulated, which results in the rotation of the vector around z-axis. (d) The second $\pi/2$-pulse is applied, rotating the vector around y-axis again. And the mean value of $\langle S_z \rangle$ is measured. (Bottom) Normalized relative atom number $2\langle S_z \rangle/(N_a + N_b)$ as a function of the Ramsey phase. The red shaded area is the standard deviation of the measurement due to quantum projection noise.

final observable can be written as (see appendix B)

$$\begin{aligned} \langle S_z(T) \rangle &= \langle U^\dagger(T) S_z(0) U(T) \rangle \\ &= -\langle S_z(0) \rangle \cos(\omega T) + \langle S_y(0) \rangle \sin(\omega T) \end{aligned} \tag{2.10}$$

with fluctuations

$$\begin{aligned} \Delta S_z^2(T) = &\Delta S_z^2(0) \cos^2(\omega T) + \Delta S_y^2(0) \sin^2(\omega T) \\ &- \Delta_{yz}(0) \sin(\omega T) \cos(\omega T) \end{aligned} \tag{2.11}$$

where $\Delta_{yz} = \langle S_y S_z + S_z S_y \rangle - 2\langle S_y \rangle \langle S_z \rangle$. For the case described in step (a), $\langle S_y(0) \rangle = \Delta S_z^2(0) = 0$ and $\langle S_z(0) \rangle = N/2$, so that $\langle S_z(T) \rangle = -N\cos(\omega T)/2$ and $\Delta S_z^2(T) = \Delta S_y^2(0) \sin^2(\omega T)$. In this case, the highest phase sensitivity is reached when $\omega T = \pi/2$, and the variance of the measured frequency can be expressed as [29]

$$|\Delta\omega|^2 = \frac{\Delta S_z^2(T)}{|\partial \langle S_z(T) \rangle / \partial \omega|^2} = \frac{\Delta S_y^2(0)}{T^2 \langle S_z(0) \rangle^2} \tag{2.12}$$

Here we have assumed that state preparation and detection time are small compared to the Ramsey interrogation time T, and the measurement noise is only limited by projection noise. We have to mention that a standard quantum limited signal in atomic clocks has already been reached [46]. From Eq.(2.12) we find that, if one could use a spin squeezed state instead of using a coherent spin state at the beginning of the interrogation time, the uncertainty of the measured frequency $\Delta\omega$ would be reduced. By using the definition (2.8), one has

$$\Delta\omega = \frac{\xi(0)}{\sqrt{N}T} \tag{2.13}$$

The squeezing parameter ξ gives the gain for the uncertainties with respect to the phase state where $\xi = 1$. For this reason, the achievement of large squeezing in atomic ensembles is a major challenge in our field.

2.1.3 Different paths to spin squeezing and state of the art

Spin squeezed states were firstly achieved [47, 48], and used to improve the precision of spectroscopic measurement with trapped ions [49]. For neutral atoms, there are two classes of schemes which are presently under investigation to create spin squeezing. The first class of schemes relies on the interaction between matter and light. The explored paths are transfer of squeezing from light to atoms [50, 51, 52], quantum coherent feedback in a cavity [53, 54], and quantum non demolition (QND) measurements of one spin component [55, 56, 57, 58], as recently implemented in spectroscopy [59, 60].

The second class of squeezing schemes does not need light and relies on atomic interactions in a bimodal Bose-Einstein condensates. The nonlinearities provided by atomic interactions for the atomic field can be used to create both spin squeezed state [23] and Schrödinger cat-like states [24, 25]. The first demonstrations of spin squeezing in BEC were observed with the atoms trapped in a double well [42]. By slowly increasing the height of the barrier in the trap in presence of interactions, spin squeezed states were prepared where relative number squeezing in the two wells simultaneously to a good phase coherence was observed. In these cases, the squeezing does not occur on an atomic transition but on two spatial modes for the same internal state. We will study this scheme in chapter 7.

On the other hand, in the following four chapters, we will focus on a dynamical squeezing scheme using condensates that would in principle allow to create a large amount of spin squeezing [23]. In this scheme an initially factorized state, where each atom is in an equal superposition of the two orthogonal modes dynamically evolves into an entangled spin squeezed state. This scheme was recently achieved with ^{87}Rb condensates by using a Feshbach resonance [41] in an optical trap and by using state-dependent potential on an atom chip to tune the atomic nonlinearity [40].

2.2 Dynamical spin squeezing in a BEC

Bose-Einstein condensates are macroscopic quantum states in which to the lowest order approximation all atoms occupy the same state. A condensate involving two internal states or bosonic modes besides its external degrees of freedom, has *internal* degrees of freedom that are equivalent to those of N indistinguishable pseudo spins. Such system can be mapped on the Bloch sphere, and one can rotate the spins on the Bloch sphere by applying a pulse which couples the two internal states or by coherent tunneling for condensates into two spatial modes. On the other hand, the collisional interactions between atoms furnish a nonlinearity to the atomic field analogous to a Kerr nonlinearity in optics. In this case, quantum correlations are established between the atoms. Large amount of entanglement and spin squeezing then can be achieved [23].

Here we show a two-mode model as a starting point to understand how squeezing is created in the condensate with the dynamical scheme. In this model, we focus on the spin dynamics of the system, neglecting the dynamics of the spatial modes. A more detailed model in which the spatial dynamics is also included will be given in Chapter 4.

2.2.1 Quadratic Hamiltonian

We consider a two-component weakly interacting Bose-Einstein condensate consisting of N atoms in two orthogonal modes for example two different hyperfine states $|a\rangle$ and $|b\rangle$. We assume that the interactions do not change the internal state of the atoms, i.e., the interactions between the particles are elastic. The second quantized Hamiltonian is

$$\begin{aligned}\mathcal{H} = \sum_{\varepsilon=a,\,b} \int d^3r\, \hat{\Psi}^{\dagger}_{\varepsilon}(\mathbf{r}) h_{\varepsilon} \hat{\Psi}_{\varepsilon}(\mathbf{r}) + \sum_{\varepsilon=a,\,b} \frac{g_{\varepsilon\varepsilon}}{2} \int d^3r\, \hat{\Psi}^{\dagger}_{\varepsilon}(\mathbf{r}) \hat{\Psi}^{\dagger}_{\varepsilon}(\mathbf{r}) \hat{\Psi}_{\varepsilon}(\mathbf{r}) \hat{\Psi}_{\varepsilon}(\mathbf{r}) \\ + g_{ab} \int d^3r\, \hat{\Psi}^{\dagger}_{a}(\mathbf{r}) \hat{\Psi}^{\dagger}_{b}(\mathbf{r}) \hat{\Psi}_{b}(\mathbf{r}) \hat{\Psi}_{a}(\mathbf{r}), \qquad (2.14)\end{aligned}$$

where $h_{\varepsilon} = -\hbar^2 \nabla^2/(2M) + U^{(\varepsilon)}_{\text{ext}}(\mathbf{r})$, is the one-particle Hamiltonian for atoms in state ε including the kinetic energy and external trapping potential, and

$g_{\varepsilon\varepsilon'} = 4\pi\hbar^2 a_{\varepsilon\varepsilon'}/M$ is the strength of the interactions between particles of type ε and ε', $a_{\varepsilon\varepsilon'}$ is the scattering length for a two-body collision, M is the mass of the atom. $\hat{\Psi}_\varepsilon(\mathbf{r})$ and $\hat{\Psi}^\dagger_\varepsilon(\mathbf{r})$ are boson field annihilation and creation operators for atoms in the state ε.

We adopt here the two-mode approximation in which we neglect the excitations out of the two condensate modes. The field operators can then be approximated as

$$\hat{\Psi}_a(\mathbf{r}) = a\,\phi_a(\mathbf{r})\,, \qquad \hat{\Psi}_b(\mathbf{r}) = b\,\phi_b(\mathbf{r}) \tag{2.15}$$

where a ($a^\dagger$) and b ($b^\dagger$) are annihilation (creation) operators for the component a and b. Using the Hamiltonian (2.14) we obtain the Heisenberg equation of motion for the field operator:

$$\begin{aligned} i\hbar\frac{d}{dt}\hat{\Psi}_\varepsilon(\mathbf{r}) &= \left[\hat{\Psi}(\mathbf{r}), \mathcal{H}\right] \\ &= h_\varepsilon\hat{\Psi}_\varepsilon(\mathbf{r}) + g_{\varepsilon\varepsilon}\hat{\Psi}^\dagger_\varepsilon(\mathbf{r})\hat{\Psi}_\varepsilon(\mathbf{r})\hat{\Psi}_\varepsilon(\mathbf{r}) + g_{\varepsilon\varepsilon'}\hat{\Psi}^\dagger_{\varepsilon'}(\mathbf{r})\hat{\Psi}_{\varepsilon'}(\mathbf{r})\hat{\Psi}_\varepsilon(\mathbf{r}) \end{aligned} \tag{2.16}$$

where $\varepsilon \neq \varepsilon'$. For a state with a given number of atoms in a and b respectively, we can rewrite the operator $\hat{N}_\varepsilon$ as a C-number N_ε. Inserting Eq.(2.15) into Eq.(2.16), we derive the equations for the two wave functions, i.e. the coupled Gross-Pitaevskii equations

$$i\hbar\frac{\partial}{\partial t}\phi_\varepsilon(\mathbf{r}) = \left[h_\varepsilon + (N_\varepsilon - 1)g_{\varepsilon\varepsilon}|\phi_\varepsilon(\mathbf{r})|^2 + N_{\varepsilon'}g_{\varepsilon\varepsilon'}|\phi_{\varepsilon'}(\mathbf{r})|^2\right]\phi_\varepsilon(\mathbf{r})\,. \tag{2.17}$$

where the operators $\hat{N}_\varepsilon$ have been replaced by C-numbers. The stationary solutions for above equations satisfy

$$\mu_\varepsilon\phi_\varepsilon(\mathbf{r}) = \left[h_\varepsilon + (N_\varepsilon - 1)g_{\varepsilon\varepsilon}|\phi_\varepsilon(\mathbf{r})|^2 + N_{\varepsilon'}g_{\varepsilon\varepsilon'}|\phi_{\varepsilon'}(\mathbf{r})|^2\right]\phi_\varepsilon(\mathbf{r})\,, \tag{2.18}$$

where μ_ε is the chemical potential, and both μ_ε and ϕ_ε depend on N_a and N_b. It is convenient to introduce Fock states, that are states with a well-defined number of particles in a and in b, these numbers being preserved by the time evolution. By using the Fock basis, the chemical potential can be written as

$$\mu_\varepsilon(N_a, N_b) = \frac{d\,\langle N_a, N_b|\mathcal{H}|N_a, N_b\,\rangle}{d\,N_\varepsilon}\,. \tag{2.19}$$

In the squeezing scheme that interests us, the initial state can be prepared by a mixing pulse, starting from N atoms in a single condensate. After the pulse the state can be described by

$$|\psi(0)\rangle = |\varphi\rangle_N = \frac{1}{\sqrt{N!}}\left[C_a\,a^\dagger + C_b\,b^\dagger\right]^N|\text{vac}\rangle \tag{2.20}$$

where all atoms are in the superposition state $C_a|a\rangle + C_b|b\rangle$. C_a, C_b are mixing coefficients with $|C_a|^2 + |C_b|^2 = 1$. The initial state has a well defined relative phase $\varphi = \arg(C_a^* C_b)$ between the components. When we expand the initial state over Fock states,

$$|\varphi\rangle_N = \frac{1}{\sqrt{N!}} \sum_{N_a=0}^{N} \left(\frac{N!}{N_a! N_b!}\right)^{1/2} C_a^{N_a} C_b^{N_b} |N_a, N_b\rangle \tag{2.21}$$

where $N_a + N_b = N$, the binomial coefficients in Eq.(2.21), for large N, will be peaked around the average number of particles in a and b, i.e. $\bar{N}_a$ and $\bar{N}_b$. We can use this fact to expand the Hamiltonian of the system to the second order around $\bar{N}_a$ and $\bar{N}_b$

$$\begin{aligned}\mathcal{H}_0 \simeq{} & E(\bar{N}_a, \bar{N}_b) + \sum_{\varepsilon=a,\, b} \mu_\varepsilon (\hat{N}_\varepsilon - \bar{N}_\varepsilon) + \frac{1}{2} \partial_{N_\varepsilon} \mu_\varepsilon (\hat{N}_\varepsilon - \bar{N}_\varepsilon)^2 \\ & + \frac{1}{2} \left(\partial_{N_b} \mu_a + \partial_{N_a} \mu_b\right) (\hat{N}_a - \bar{N}_a)(\hat{N}_b - \bar{N}_b)\end{aligned} \tag{2.22}$$

where the chemical potentials μ_ε and all the derivatives of μ_ε should be evaluated in $\bar{N}_a$ and $\bar{N}_b$. We can rewrite (2.22) as

$$\begin{aligned}\mathcal{H}_0 &= f_{\hat{N}} + \hbar\, v_{\hat{N}} (\hat{N}_a - \hat{N}_b) + \frac{\hbar \chi_d^{\mathrm{2m}}}{4} (\hat{N}_a - \hat{N}_b)^2 \\ &= f_{\hat{N}} + 2\hbar\, v_{\hat{N}} S_z + \hbar \chi_d^{\mathrm{2m}} S_z^2\end{aligned} \tag{2.23}$$

with

$$v_{\hat{N}} = \frac{1}{2\hbar} \left[(\mu_a - \mu_b) - \hbar \chi_d^{\mathrm{2m}} (\bar{N}_a - \bar{N}_b) + \hbar \chi_s^{\mathrm{2m}} (\hat{N} - \bar{N}) \right] \tag{2.24}$$

$$\chi_d^{\mathrm{2m}} = \frac{1}{2\hbar} \left(\partial_{N_a} \mu_a + \partial_{N_b} \mu_b - \partial_{N_b} \mu_a - \partial_{N_a} \mu_b\right)_{\bar{N}_a, \bar{N}_b} \tag{2.25}$$

$$\chi_s^{\mathrm{2m}} = \frac{1}{2\hbar} (\partial_{N_a} \mu_a - \partial_{N_b} \mu_b)_{\bar{N}_a, \bar{N}_b}\,. \tag{2.26}$$

The function $f_{\hat{N}}$ of the total number of particles, $\hat{N} = \hat{N}_a + \hat{N}_b$, commutes with the spin operators of the system and can be omitted. The second term in equation (2.23) proportional to S_z describes spin precession around z with velocity $v_{\hat{N}}$. The third term due to elastic collisional interactions in BEC provides the nonlinearity responsible for spin squeezing. It also provides a second contribution to the drift of the relative phase between the two condensates in the case $\bar{N}_a \neq \bar{N}_b$.

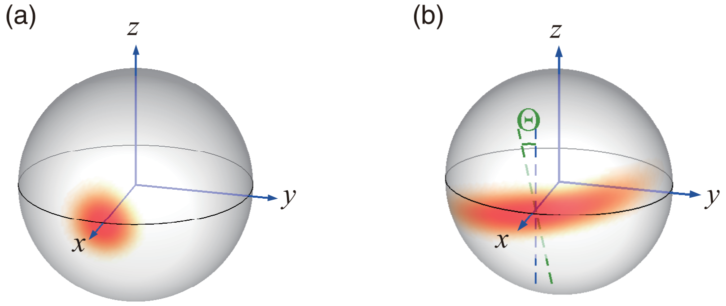

Figure 2.3: State evolution by one-axis twisting on the Bloch sphere for $N = 100$. (a) The initial state Eq.(2.5) is the eigenstate of S_x. (b) The state twisted around axis-z with the Hamiltonian (2.27), $t = 0.05/\chi$.

2.2.2 Solution of the symmetric case

To show the mechanism of squeezing, in this subsection, we study the Hamiltonian from Eq.(2.23) in the symmetric case. Such model has also been discussed in [44]. In the next subsection, we will extend the discussion to a more general non symmetric case.

Consider Eq.(2.5) as the initial state. Assume that the two components of the condensate have the same scattering length, then the Hamiltonian (2.23) can be simplified as

$$\mathcal{H}_0 = \hbar\chi_d^{2\mathrm{m}} S_z^2 \tag{2.27}$$

where the spin operators (2.1)-(2.3) in the second quantized version can be written as

$$S_x = \frac{1}{2}(b^\dagger a + a^\dagger b), \tag{2.28}$$

$$S_y = \frac{i}{2}(b^\dagger a - a^\dagger b), \tag{2.29}$$

$$S_z = \frac{1}{2}(a^\dagger a - b^\dagger b). \tag{2.30}$$

Mapped on the Bloch sphere, such state is pictorially represented as a round circle perpendicular to the axis-x, as shown in Fig.2.3 (a).

During the evolution, the states with different S_z on the Bloch sphere will rotate around axis-z with a velocity proportional to S_z. Therefore the quantum fluctuations are deformed on the Bloch sphere, so-called one axis twisting effect, as shown in Fig.2.3 (b). The uncertainties in the plane orthogonal to the mean spin can be written as

$$\Delta S_\perp^2(\Theta) = \cos^2\Theta \Delta S_y^2 + \sin^2\Theta \Delta S_z^2 + \sin(2\Theta)\left(\mathrm{Re}\langle S_y S_z\rangle - \langle S_y\rangle\langle S_z\rangle\right) \tag{2.31}$$

where $S_\perp(\Theta)$ is the spin component in the plane orthogonal to the mean spin, along the direction which has an angle Θ with respect to axis-z (see Fig.2.3 (b)). Minimizing $\Delta S_\perp^2$ with respect to Θ, we get

$$\Delta S^2_{\perp,\,\mathrm{min}} = \frac{1}{2}\left[2\Delta S_z^2 + \tilde{A} - \sqrt{\tilde{A}^2 + \tilde{B}^2}\right], \tag{2.32}$$

where

$$\tilde{A} = \Delta S_y^2 - \Delta S_z^2 = 1 - \cos(2\chi_d^{2\mathrm{m}} t)^{N-2} \tag{2.33}$$

$$\tilde{B} = 2\mathrm{Re}\langle S_y S_z\rangle - 2\langle S_y\rangle\langle S_z\rangle = 4\sin(\chi_d^{2\mathrm{m}} t)\cos(\chi_d^{2\mathrm{m}} t)^{N-2} \tag{2.34}$$

and $\Delta S_z^2 = N/4$ is unchanged during the evolution. In the limit of large N, the squeezing parameter Eq.(2.8) can be approximated as

$$\xi^2(t) = \frac{1}{N^2(\chi_d^{2\mathrm{m}} t)^2} + \frac{1}{6}N^2(\chi_d^{2\mathrm{m}} t)^4, \tag{2.35}$$

From Eq.(2.35) one notes that there exists a time at which the squeezing parameter ξ^2 reaches its minimum,

$$\xi^2 \sim N^{-2/3}\,. \tag{2.36}$$

This time is referred to as the best squeezing time

$$|\chi_d^{2\mathrm{m}}|\, t_{\mathrm{best}} \simeq N^{-2/3} \tag{2.37}$$

From above expressions, we find that when $N \to \infty$, one has $\xi^2 \to 0$. There is no limit to the amount of squeezing that can be reached by increasing N. However, we will see in the next chapter that this is only the case when there are no decoherence present such as particle losses.

Besides spin squeezing, the nonlinearity will introduce another effect which makes the relative phase between the two components collapse. The time scale for such effect, compared with spin squeezing, is much longer. Note that, squeezing and phase spreading are indeed caused by the same physical process, namely the nonlinear term in the Hamiltonian. For the simple case which we consider here, the term describing the relative phase coherence is

$$\langle b^\dagger a\rangle = \langle S_x\rangle = \frac{N}{2}\cos^{N-1}\left(\chi_d^{2\mathrm{m}} t\right) \simeq \frac{N}{2}\exp\left[-\frac{1}{2}N\left(\chi_d^{2\mathrm{m}} t\right)^2\right], \tag{2.38}$$

which has a Gaussian decay. The phase coherence will collapse in a time scale

$$|\chi_d^{2\mathrm{m}}|\, t_c \sim N^{-1/2} \tag{2.39}$$

For large number of atoms, t_c is much longer than t_{best}, meaning that at the best squeezing time we still have very good phase coherence.

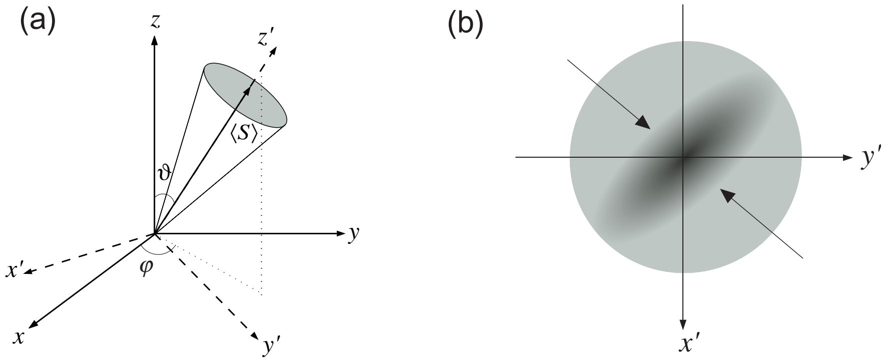

Figure 2.4: (a) Average spin. (b) Variance of the spin components in the plane orthogonal to the mean spin.

2.2.3 More general non symmetric case

Now we consider a more general initial state (2.20), that is the eigenstate of the spin operator $S_{\vartheta,\varphi}$ with

$$S_{\vartheta,\varphi} = S_x \sin\vartheta\cos\varphi + S_y \sin\vartheta\sin\varphi + S_z\cos\vartheta, \tag{2.40}$$

where ϑ and φ are two polar angles giving the direction of the mean spin, and $\cos\vartheta = |C_a|^2 - |C_b|^2$, $\varphi = \arg(C_a^* C_b)$, as shown in Fig.2.4 (a). The Hamiltonian has the form of Eq.(2.23). The minimal variance of the spin $\Delta S^2_{\perp,\min}$ in the plane (x', y') orthogonal to the mean spin, represented in Fig.2.4 (b), is the same as Eq.(2.32) with $x \to z'$. Referring to Fig.2.4, the three spin components (S'_x, S'_y, S'_z) expressed in the original frame (S_x, S_y, S_z) can be written as

$$\begin{aligned} S'_x &= (\cos\vartheta\cos\varphi\cos\Theta - \sin\varphi\sin\Theta)\, S_x & (2.41)\\ &\quad +(\cos\vartheta\sin\varphi\cos\Theta + \cos\varphi\sin\Theta)\, S_y - \sin\vartheta\cos\Theta\, S_z \\ S'_y &= -(\cos\vartheta\cos\varphi\sin\Theta + \sin\varphi\cos\Theta)\, S_x & (2.42)\\ &\quad -(\cos\vartheta\sin\varphi\sin\Theta - \cos\varphi\cos\Theta)\, S_y + \sin\vartheta\sin\Theta\, S_z \\ S'_z &= \sin\vartheta\cos\varphi\, S_x + \sin\vartheta\sin\varphi\, S_y + \cos\vartheta\, S_z & (2.43) \end{aligned}$$

By changing the coordinates, in the original frame of reference the minimal variance can be written as

$$\begin{aligned} \Delta S^2_{\perp,\min} =& \frac{1}{2}(\cos^2\vartheta\cos^2\varphi + \sin^2\varphi)\Delta S_x^2 + \frac{1}{2}(\cos^2\vartheta\sin^2\varphi + \cos^2\varphi)\Delta S_y^2 \\ &+ \frac{1}{2}\sin^2\vartheta\Delta S_z^2 - \frac{1}{4}\sin^2\vartheta\sin 2\varphi\Delta_{xy} - \frac{1}{4}\sin 2\vartheta\cos\varphi\Delta_{zx} \\ &- \frac{1}{4}\sin 2\vartheta\sin\varphi\Delta_{yz} - \frac{1}{2}\sqrt{\tilde{A}^2 + \tilde{B}^2} \end{aligned} \tag{2.44}$$

where

$$\begin{aligned}\tilde{A} =& (\sin^2\varphi - \cos^2\vartheta\cos^2\varphi)\Delta S_x^2 + (\cos^2\varphi - \cos^2\vartheta\sin^2\varphi)\Delta S_y^2 \\ & -\sin^2\vartheta\Delta S_z^2 - \frac{1}{2}(1+\cos^2\vartheta)\sin 2\varphi\Delta_{xy} + \frac{1}{2}\sin 2\vartheta\cos\varphi\Delta_{zx} \\ & +\frac{1}{2}\sin 2\vartheta\sin\varphi\Delta_{yz}\,; \end{aligned} \quad (2.45)$$

$$\begin{aligned}\tilde{B} =& \cos\vartheta\sin 2\varphi(\Delta S_x^2 - \Delta S_y^2) - \cos\vartheta\cos 2\varphi\Delta_{xy} - \sin\vartheta\sin\varphi\Delta_{zx} \\ & +\sin\vartheta\cos\varphi\Delta_{yz}\,; \end{aligned} \quad (2.46)$$

and where we introduced the correlations

$$\Delta_{ij} = \langle S_i S_j + S_j S_i\rangle - 2\langle S_i\rangle\langle S_j\rangle, \quad i \neq j = x, y, z\,. \quad (2.47)$$

The expectation values related to the collective spin operators S_i defined in Eqs.(2.28)-(2.30) can be expressed by the quantum averages given by,

$$\langle b^\dagger a\rangle = C_b^* C_a\, e^{-2ivt} N \mathcal{J}_1^{N-1} \quad (2.48)$$

$$\langle b^\dagger b^\dagger b a\rangle = |C_b|^2 C_b^* C_a\, e^{-i(2v-\chi_d^{2\mathrm{m}})t} N(N-1)\mathcal{J}_1^{N-2} \quad (2.49)$$

$$\langle a^\dagger a^\dagger a b\rangle = |C_a|^2 C_a^* C_b\, e^{i(2v+\chi_d^{2\mathrm{m}})t} N(N-1)\mathcal{J}_{-1}^{N-2} \quad (2.50)$$

$$\langle b^\dagger b^\dagger a a\rangle = C_b^{*2} C_a^2\, e^{-4ivt} N(N-1)\mathcal{J}_2^{N-2} \quad (2.51)$$

where we introduced the function $\mathcal{J}_\beta$ with $\beta = -1, 1, 2$

$$\mathcal{J}_\beta = |C_a|^2 e^{-i\beta\chi_d^{2\mathrm{m}}t} + |C_b|^2 e^{i\beta\chi_d^{2\mathrm{m}}t} \quad (2.52)$$

and the drift velocity

$$v = \frac{1}{2\hbar}\left[(\mu_a - \mu_b) - \hbar\chi_d^{2\mathrm{m}}(\bar{N}_a - \bar{N}_b) + \hbar\chi_s^{2\mathrm{m}}(N - \bar{N})\right], \quad (2.53)$$

where N is the total initial number of atoms.

In the following chapters, where the particle losses and spatial dynamics are taken into account, we will always calculate the these quantum averages within the relevant model. The squeezing parameters ξ^2 then can be obtained with the definition (2.8) from these quantum averages (see appendix A).

Chapter 3

Effect of decoherence : particle losses

In the previous chapter, we have considered the spin squeezing created by the interactions between the cold atoms. For such a scheme, particle losses will be an unavoidable source of decoherence. In experiments of cold atoms, there are several kinds of losses: one-body losses caused by collision of condensed atoms with the hot background gas; two-body losses due to spin-dipole interactions or spin-exchange interactions; three-body losses caused by collisions followed by recombination of two atoms to form a molecule. Indeed, the last one is more intrinsic in the scheme considered here, since three-body losses come always with the coherent interactions, and reflect the fact that ultracold atoms are in a metastable gas phase.

In this chapter we study the effect of decoherence by using an analytical Monte-Carlo wave functions approach [61, 62, 63]. The principle goal is to answer the fundamental question: whether or not one could improve without limits the squeezing by increasing the number of particles in the system. We have seen from Eq.(2.37) that the best squeezing time tends to zero when the total number of atoms $N \to \infty$, which suggests that one would still have $\xi^2 \to 0$ in presence of decoherence. Indeed we will show that this is the case when only one-body losses are present, although ξ^2 tends to zero more slowly than $N^{-2/3}$ that is the result in the absence of losses. When two-body and three-body losses are considered in addition to one-body losses, the situation changes completely as now decoherence itself increase with N. The main results of this chapter are published in [35, 36].

3.1 Spin squeezing with particle losses

We still restrict to the two-mode model as discussed in the previous chapter. The Hamiltonian in the no-loss case

$$\mathcal{H}_0 = f_{\hat{N}} + \hbar v_{\hat{N}}(\hat{N}_a - \hat{N}_b) + \frac{\hbar\chi_d^{2\mathrm{m}}}{4}(\hat{N}_a - \hat{N}_b)^2 \tag{3.1}$$

is the same as Eq.(2.23). In presence of losses, the evolution is ruled by a master equation for the density operator ρ of the system. In the interaction picture with respect to $\mathcal{H}_0$, with one, two, and three-body losses, we have:

$$\begin{aligned}\frac{d\tilde{\rho}}{dt} =& \sum_{m=1}^{3}\sum_{\varepsilon=a,b}\gamma_\varepsilon^{(m)}\left[c_\varepsilon^m\,\tilde{\rho}\,c_\varepsilon^{\dagger m} - \frac{1}{2}\{c_\varepsilon^{\dagger m}c_\varepsilon^m,\tilde{\rho}\,\}\right] \\ &+ \gamma_{ab}\left[c_a c_b\,\tilde{\rho}\,c_a^\dagger c_b^\dagger - \frac{1}{2}\{c_a^\dagger c_b^\dagger c_a c_b,\tilde{\rho}\,\}\right],\end{aligned} \tag{3.2}$$

where $\tilde{\rho} = e^{i\mathcal{H}_0 t/\hbar}\,\rho\,e^{-i\mathcal{H}_0 t/\hbar}$, $c_a = e^{i\mathcal{H}_0 t/\hbar}\,a\,e^{-i\mathcal{H}_0 t/\hbar}$, and similarly for b. Note that now the annihilation operators c_ε depend on time. The constants $\gamma_\varepsilon^{(m)}$ and γ_{ab} are defined as

$$\gamma_\varepsilon^{(m)} = \frac{K_\varepsilon^{(m)}}{m}\int d^3r|\bar{\phi}_\varepsilon(\mathbf{r})|^{2m}, \tag{3.3}$$

$$\gamma_{ab} = K_{ab}\int d^3r|\bar{\phi}_a(\mathbf{r})|^2|\bar{\phi}_b(\mathbf{r})|^2. \tag{3.4}$$

$K_\varepsilon^{(m)}$ is the m-body rate constant ($m = 1,2,3$) and $\bar{\phi}_\varepsilon(\mathbf{r})$ ($\varepsilon = a,b$) is the condensate wave function for the ε component with $N_a = \bar{N}_a$ and $N_b = \bar{N}_b$ particles. The wave function $\bar{\phi}_\varepsilon(\mathbf{r})$ can be obtained from the stationary solution of Gross-Pitaevskii equation (2.18). K_{ab} is the rate constant for a two-body loss event in which two particles coming from different components are lost at once[1]. The number of condensate atoms N_ε accordingly decays as:

$$\begin{aligned}\dot{N}_\varepsilon(t) =& -\sum_{m=1}^{3}K_\varepsilon^{(m)}\int d^3r N_\varepsilon^m(t)|\bar{\phi}_\varepsilon(\mathbf{r},t)|^{2m} \\ &- K_{ab}\int d^3r N_a(t)N_b(t)|\bar{\phi}_a(\mathbf{r},t)|^2|\bar{\phi}_b(\mathbf{r},t)|^2.\end{aligned} \tag{3.5}$$

We study this problem by using the Monte-Carlo wave function approach [61, 62], in which the state of the system is described by a state vector, and

---

[1] Here the three-body losses in which three particles coming from different components are not taken into account

the irreversibility in the evolution is introduced by stochastic quantum jumps plus non unitary evolution applied to the state vector. When we average expectation values of an observable over a large number of realizations for the state vector evolution starting from the same initial state, we recover the quantum average that would result from solving the master equation (3.2). We define an effective Hamiltonian $\mathcal{H}_{\text{eff}}$ and the jump operators $J_\varepsilon^{(m)}(J_{ab}^{(2)})$

$$\mathcal{H}_{\text{eff}} = -\frac{i\hbar}{2}\sum_{m=1}^{3}\sum_{\varepsilon=a,b}\gamma_\varepsilon^{(m)} c_\varepsilon^{\dagger m} c_\varepsilon^{m} - \frac{i\hbar}{2}\gamma_{ab}\, c_a^\dagger c_b^\dagger c_a c_b\,; \tag{3.6}$$

$$J_\varepsilon^{(m)} = \sqrt{\gamma_\varepsilon^{(m)}}\, c_\varepsilon^{m}\,,\; J_{ab}^{(2)} = \sqrt{\gamma_{ab}}\, c_a c_b\,. \tag{3.7}$$

We assume that a small fraction of particles will be lost during the evolution so that we can consider $\chi_d^{2\text{m}}$, $\chi_s^{2\text{m}}$, $\gamma_\varepsilon^{(m)}$ and γ_{ab} as constant parameters of the model. The state evolution in a single quantum trajectory is a sequence of random quantum jumps at times t_j and non-unitary Hamiltonian evolutions of duration τ_j :

$$\begin{aligned} |\psi(t)\rangle =& e^{-i\mathcal{H}_{\text{eff}}(t-t_k)/\hbar} J_{\varepsilon_k}^{(m_k)}(t_k) e^{-i\mathcal{H}_{\text{eff}}\tau_k/\hbar} J_{\varepsilon_{k-1}}^{(m_{k-1})}(t_{k-1}) \\ & \ldots J_{\varepsilon_1}^{(m_1)}(t_1) e^{-i\mathcal{H}_{\text{eff}}\tau_1/\hbar}|\psi(0)\rangle\,, \end{aligned} \tag{3.8}$$

where now $\varepsilon_j = a, b$ or ab. As the Hamiltonian (3.1) is a function of $\hat{N}_a$ and $\hat{N}_b$, we can move all the annihilation operators a and b in the quantum jumps of Eq.(3.7) to the right hand side by using the commutation relations

$$a\, f(\hat{N}_a, \hat{N}_b) = f(\hat{N}_a + 1, \hat{N}_b)\, a\,, \quad b\, f(\hat{N}_a, \hat{N}_b) = f(\hat{N}_a, \hat{N}_b + 1)\, b\,. \tag{3.9}$$

Since for the phase state (2.20) one has

$$\exp\left[-\Delta(\hat{N}_a - \hat{N}_b)\right] |\varphi\rangle_N = |\varphi + 2\Delta\rangle_N\,, \tag{3.10}$$

$$a\,|\varphi\rangle_N = C_a\sqrt{N}|\varphi\rangle_{N-1}, \quad b\,|\varphi\rangle_N = C_b\sqrt{N}|\varphi\rangle_{N-1}, \tag{3.11}$$

application of a jump $J_{\varepsilon_j}^{(m_j)}(t_j)$ to the N-particle phase state at time t_j yields

$$J_{\varepsilon_j}^{(m_j)}(t_j)|\,\varphi\rangle_N \propto |\,\varphi + \Delta_j t_j\,\rangle_{N-m_j}\,, \tag{3.12}$$

$$\Delta_j = 2\chi_s^{2\text{m}}\delta_{\varepsilon_j, ab} + (\chi_s^{2\text{m}} + \chi_d^{2\text{m}}) m_j\, \delta_{\varepsilon_j, a} + (\chi_s^{2\text{m}} - \chi_d^{2\text{m}}) m_j\, \delta_{\varepsilon_j, b} \tag{3.13}$$

After a quantum jump, the phase state is changed into a new phase state, with m_j particle less and with the relative phase between the two modes showing a random shift $\Delta_j\, t_j$ with respect to the phase before the jump,

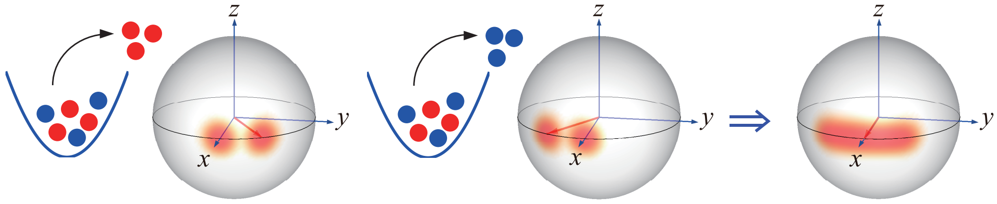

Figure 3.1: Illustration of the degradation of relative phase by a three-body loss event. Initially the mean spin is assumed to be aligned with axis-x. After a quantum jump, if three particles in state a (red) are lost, the relative phase will show a positive shift, while if three particles in state b (blue) are lost, the relative phase will show a negative shift. Averaging over all stochastic processes finally degrades the relative phase.

which reduces the squeezing. Note that in the symmetric case $\chi_s^{\rm 2m} = 0$, and no random phase shift occurs in the case of a jump of ab. Indeed we will find that at short times in the symmetric case, these kind of crossed ab losses are harmless to the squeezing.

Here we give an example of how random loss events degrade relative phase and squeezing. We consider the three-body losses for a symmetric case where $\bar{N}_a = \bar{N}_b$ and $a_{aa} = a_{bb}$. In this case, $\chi_s^{\rm 2m} = 0$. By using the commutation relations Eq.(3.9), the jump operator for each component can be written as

$$J_a(t_j) = \sqrt{\gamma_a^{(3)}}\, e^{-i3\chi_d^{\rm 2m} t_j\, S_z} a^3, \quad J_b(t_j) = \sqrt{\gamma_b^{(3)}}\, e^{i3\chi_d^{\rm 2m} t_j\, S_z} b^3 \tag{3.14}$$

Applying a quantum jump to the N-particle phase state results in

$$J_{\varepsilon_j}(t_j)|\varphi\rangle_N \propto |\varphi + 3\chi_d^{\rm 2m}(\delta_{\varepsilon_j,a} - \delta_{\varepsilon_j,b})t_j\rangle_{N-3}\,, \tag{3.15}$$

where $\varepsilon_j = a, b$, implying that, in each loss event, if three particles in state a are lost, the relative phase will show a positive shift, while if three particles in state b are lost, the relative phase will show a negative shift, as illustrated in Fig.3.1. After averaging over all stochastic processes, the relative phase is degraded, and the spin squeezing is reduced.

For the nonsymmetric case where $\chi_s^{\rm 2m} \neq 0$, there is another effect that degrades the spin squeezing. Namely the random loss event makes the direction of mean spin fluctuate for different trajectories. This is due to the fact that the second term in Eq.(3.1) which gives the mean spin precession around z also depends on the total number of atoms when the two components see different mean-field, as shown in Eq.(2.24). This results in some extra phase noise due to losses.

The expectation value of any observable $\hat{\mathcal{O}}$ is obtained by averaging over all possible stochastic realizations, that is all kinds, times and number of quantum jumps, each trajectory being weighted by its probability

$$\langle\hat{\mathcal{O}}\rangle = \sum_k \int_{0<t_1<t_2<\cdots t_k<t} dt_1 dt_2 \cdots dt_k \sum_{\{\varepsilon_j, m_j\}} \langle\psi(t)|\hat{\mathcal{O}}|\psi(t)\rangle \,. \tag{3.16}$$

Note that the single trajectory (3.8) is not normalized. The norm will provide its correct "weight" in the average.

3.1.1 Exact analytical solution for one-body losses

With one-body losses only, the problem is exactly solvable. This is because for one-body losses the effective Hamiltonian (3.6) is proportional to $\hat{N}_a$ and $\hat{N}_b$, so it does not affect the state. By using the property that

$$c_{\varepsilon_j}(t_j)\, \mathcal{H}_{\text{eff}}(\hat{N}_a, \hat{N}_b) = \mathcal{H}_{\text{eff}}(\hat{N}_a + \delta_{\varepsilon_j, a}, \hat{N}_b + \delta_{\varepsilon_j, b})\, c_{\varepsilon_j}(t_j) \,, \tag{3.17}$$

we can move all the jump operators in Eq.(3.8) to the right side close to the initial state $|\psi(0)\rangle$. The evolution of a single quantum trajectory with k quantum jumps results in

$$\begin{aligned} |\psi(t)\rangle = &\exp\left\{-\frac{1}{2}\sum_{j=1}^{k}\left(\gamma_a \hat{N}_a + \gamma_b \hat{N}_b\right) t\right\} \left[\frac{N!}{(N-k)!}\right]^{1/2} \\ &\cdot \alpha_k |\varphi + \beta_k\rangle_{N-k, C'_a, C'_b} \end{aligned} \tag{3.18}$$

where the mixing coefficients for the phase state are changed into $C'_a = e^{-\gamma_a t/2} C_a$ and $C'_b = e^{-\gamma_b t/2} C_b$ due to the losses, and

$$|\alpha_k|^2 = \prod_{j=1}^{k} \left[|C_a|^2 \gamma_a\, \delta_{\varepsilon_j, a} + |C_b|^2 \gamma_b\, \delta_{\varepsilon_j, b}\right] \,, \tag{3.19}$$

$$\beta_k = \sum_{j=1}^{k} t_j \left[(\chi_d^{2\text{m}} + \chi_s^{2\text{m}})\, \delta_{\varepsilon_j, a} - (\chi_d^{2\text{m}} - \chi_s^{2\text{m}})\, \delta_{\varepsilon_j, b}\right] . \tag{3.20}$$

Note that the phase of α_k in Eq.(3.18) will disappear when calculate the quantum average $\langle\psi(t)|\hat{\mathcal{O}}|\psi(t)\rangle$, such that the result only concerns $|\alpha_k|$. By using Eq.(3.16), the averages needed to calculate spin squeezing with one-body losses only are given as follows,

$$
\begin{aligned}
\langle a^\dagger a\rangle &= |C_a|^2 N\exp(-\gamma_a t) && (3.21)\\
\langle b^\dagger b\rangle &= |C_b|^2 N\exp(-\gamma_b t) && (3.22)\\
\langle a^\dagger a^\dagger a a\rangle &= |C_a|^4 N(N-1)\exp(-2\gamma_a t) && (3.23)\\
\langle b^\dagger b^\dagger b b\rangle &= |C_b|^4 N(N-1)\exp(-2\gamma_b t) && (3.24)\\
\langle b^\dagger a^\dagger a b\rangle &= |C_b|^2|C_a|^2 N(N-1)\exp[-(\gamma_a+\gamma_b)t] && (3.25)\\
\langle b^\dagger a\rangle &= C_b^* C_a\, e^{-2ivt} N\exp\left[-\frac{1}{2}(\gamma_a+\gamma_b)t\right] L_1^{N-1} && (3.26)\\
\langle b^\dagger b^\dagger b a\rangle &= |C_b|^2 C_b^* C_a\, e^{-i(2v-\chi_d^{\mathrm{2m}})t} N(N-1)\exp\left[-\frac{1}{2}(\gamma_a+3\gamma_b)t\right] L_1^{N-2} && (3.27)\\
\langle a^\dagger a^\dagger a b\rangle &= |C_a|^2 C_a^* C_b\, e^{i(2v+\chi_s^{\mathrm{2m}})t} N(N-1)\exp\left[-\frac{1}{2}(3\gamma_a+\gamma_b)t\right] L_{-1}^{N-2} && (3.28)\\
\langle b^\dagger b^\dagger a a\rangle &= C_b^{*2} C_a^2\, e^{-4ivt} N(N-1)\exp\left[-(\gamma_a+\gamma_b)t\right] L_2^{N-2} && (3.29)
\end{aligned}
$$

where we introduced the functions L_β with $\beta = -1, 1, 2$

$$
\begin{aligned}
L_\beta =& \frac{|C_a|^2}{\gamma_a + i\beta(\chi_d^{\mathrm{2m}}+\chi_s^{\mathrm{2m}})}\left[\gamma_a e^{i\beta\chi_s^{\mathrm{2m}}t} + i\beta(\chi_d^{\mathrm{2m}}+\chi_s^{\mathrm{2m}})e^{-(\gamma_a+i\beta\chi_d^{\mathrm{2m}})t}\right]\\
&+ \frac{|C_b|^2}{\gamma_b - i\beta(\chi_d^{\mathrm{2m}}-\chi_s^{\mathrm{2m}})}\left[\gamma_b e^{i\beta\chi_s^{\mathrm{2m}}t} - i\beta(\chi_d^{\mathrm{2m}}-\chi_s^{\mathrm{2m}})e^{-(\gamma_b-i\beta\chi_d^{\mathrm{2m}})t}\right]
\end{aligned}
\qquad (3.30)
$$

and the drift velocity is defined as in Eq.(2.53).

3.1.2 Two and three-body losses: approximated analytical solution

When two and three-body losses are taken into account, the evolution of the effective Hamiltonian will change the state in such a way that a phase state would not be a phase state anymore, and the analysis becomes more complicated. However analytical results can still be obtained by using a constant loss rate approximation [63]. If a small fraction of particles is lost during the evolution, the effective Hamiltonian (3.6) can be approximated as

$$
\mathcal{H}_{\mathrm{eff}} \simeq -\frac{i\hbar}{2}\sum_{m=1}^{3}\sum_{\varepsilon=a,\,b}\gamma_\varepsilon^{(m)}\bar{N}_\varepsilon^m - \frac{i\hbar}{2}\gamma_{ab}\bar{N}_a\bar{N}_b \equiv -\frac{i\hbar}{2}\lambda \qquad (3.31)
$$

This approximation implies that the loss rate through out the whole evolution is constant. Indeed with the approximation (3.31), the initial phase state remains a phase state. As a consequence, when a quantum jump occurs, only the relative phase and the total number of particle changes (see equation (3.12)). The evolution of a single quantum trajectory with k quantum jumps can then be written as

$$|\Psi(t)\rangle = e^{-\lambda t/2}\prod_{j=1}^{k} J_{\varepsilon_j}^{(m_j)}(t_j)|\Psi(0)\rangle = e^{-\lambda t/2}\alpha_k|\varphi+\beta_k\rangle_{N-N(k)} \tag{3.32}$$

where

$$\begin{aligned}|\alpha_k|^2 =& \prod_{j=1}^{k}\Big\{\sum_{m'=1}^{3}\sum_{\varepsilon'=a,\,b}\delta_{m_j,\,m'}\delta_{\varepsilon_j,\,\varepsilon'}\bar{N}^{m'}|C_{\varepsilon'}|^{2m'}\gamma_{\varepsilon'}^{(m')} \\ &+\bar{N}^2|C_a|^2|C_b|^2\gamma_{ab}\delta_{\varepsilon_j,\,ab}\Big\}\end{aligned} \tag{3.33}$$

$$\begin{aligned}\beta_k =& \sum_{j=1}^{k} t_j\Big\{2\chi_s^{2\mathrm{m}}\delta_{\varepsilon_j,\,ab}+\sum_{m'=1}^{3} m'\delta_{m_j,\,m'}\big[(\chi_d^{2\mathrm{m}}+\chi_s^{2\mathrm{m}})\delta_{\varepsilon_j,\,a} \\ &-(\chi_d^{2\mathrm{m}}-\chi_s^{2\mathrm{m}})\delta_{\varepsilon_j,\,b}\big]\Big\}\end{aligned} \tag{3.34}$$

$$N(k) = \sum_{j=1}^{k}\sum_{m'=1}^{3} m'\delta_{m_j,\,m'}(\delta_{\varepsilon_j,\,a}+\delta_{\varepsilon_j,\,b})+2\delta_{\varepsilon_j,\,ab}\,, \tag{3.35}$$

In the expression (3.33) of $|\alpha_k|^2$ we replace N with $\bar{N}$ consistently with the constant loss rate approximation. The averages needed to calculate the spin squeezing for one, two and three-body losses are:

$$\langle a^\dagger a\rangle = |C_a|^2 e^{-\lambda t}\left[N-(\partial_{\sigma_1}+\partial_{\sigma_2})\right]F_0(\sigma_1,\sigma_2) \tag{3.36}$$

$$\langle b^\dagger b\rangle = |C_b|^2 e^{-\lambda t}\left[N-(\partial_{\sigma_1}+\partial_{\sigma_2})\right]F_0(\sigma_1,\sigma_2) \tag{3.37}$$

$$\langle a^\dagger a^\dagger aa\rangle = |C_a|^4 e^{-\lambda t}\left[N-(\partial_{\sigma_1}+\partial_{\sigma_2})-1\right]\left[N-(\partial_{\sigma_1}+\partial_{\sigma_2})\right]F_0(\sigma_1,\sigma_2) \tag{3.38}$$

$$\langle b^\dagger b^\dagger bb\rangle = |C_b|^4 e^{-\lambda t}\left[N-(\partial_{\sigma_1}+\partial_{\sigma_2})-1\right]\left[N-(\partial_{\sigma_1}+\partial_{\sigma_2})\right]F_0(\sigma_1,\sigma_2) \tag{3.39}$$

$$\begin{aligned}\langle b^\dagger a^\dagger ab\rangle =& |C_b|^2|C_a|^2 e^{-\lambda t}\left[N-(\partial_{\sigma_1}+\partial_{\sigma_2})-1\right]\left[N-(\partial_{\sigma_1}+\partial_{\sigma_2})\right] \\ &\cdot F_0(\sigma_1,\sigma_2)\end{aligned} \tag{3.40}$$

$$\begin{aligned}\langle b^\dagger a\rangle =& C_b^* C_b e^{-(2iv+\lambda)t}\left(|C_a|^2 e^{-i\chi_d^{2\mathrm{m}}t}+|C_b|^2 e^{i\chi_d^{2\mathrm{m}}t}\right)^{N-1} \\ &\cdot\left[N-(\partial_{\sigma_1}+\partial_{\sigma_2})\right]F_1(\sigma_1,\sigma_2)\end{aligned} \tag{3.41}$$

$$\begin{aligned}\langle b^\dagger b^\dagger ba\rangle =& |C_b|^2 C_b^* C_a e^{-(2iv-i\chi_d^{2\mathrm{m}}+\lambda)t}\left(|C_a|^2 e^{-i\chi_d^{2\mathrm{m}}t}+|C_b|^2 e^{i\chi_d^{2\mathrm{m}}t}\right)^{N-2} \\ &\cdot\left[N-(\partial_{\sigma_1}+\partial_{\sigma_2})-1\right]\left[N-(\partial_{\sigma_1}+\partial_{\sigma_2})\right]F_1(\sigma_1,\sigma_2)\end{aligned} \tag{3.42}$$

$$
\begin{aligned}
\langle a^\dagger a^\dagger a b\rangle &= |C_a|^2 C_a^* C_b e^{(2iv+i\chi_d^{2\mathrm{m}}-\lambda)\,t}\left(|C_b|^2 e^{-i\chi_d^{2\mathrm{m}}t}+|C_a|^2 e^{i\chi_d^{2\mathrm{m}}t}\right)^{N-2} \\
&\quad\cdot\left[N-(\partial_{\sigma_1}+\partial_{\sigma_2})-1\right]\left[N-(\partial_{\sigma_1}+\partial_{\sigma_2})\right]F_{-1}(\sigma_1,\sigma_2) \quad (3.43)\\
\langle b^\dagger b^\dagger a a\rangle &= C_b^{*2} C_a^2 e^{-(4iv+\lambda)t}\left(|C_a|^2 e^{-2i\chi_d^{2\mathrm{m}}t}+|C_b|^2 e^{2i\chi_d^{2\mathrm{m}}t}\right)^{N-2} \\
&\quad\cdot\left[N-(\partial_{\sigma_1}+\partial_{\sigma_2})-1\right]\left[N-(\partial_{\sigma_1}+\partial_{\sigma_2})\right]F_{2}(\sigma_1,\sigma_2) \quad (3.44)
\end{aligned}
$$

where we introduced the functions $F_\beta(\sigma_1,\sigma_2)$

$$
\begin{aligned}
F_\beta(\sigma_1,\sigma_2) = \exp\Bigg\{ &\sum_{m=1}^{3} \frac{e^{m\sigma_1}\gamma_a^{(m)}\left[1-e^{-im\beta(\chi_d^{2\mathrm{m}}+\chi_s^{2\mathrm{m}})t}\right]}{im\beta(\chi_d^{2\mathrm{m}}+\chi_s^{2\mathrm{m}})\mathcal{Q}_\beta^m} \\
&+\frac{e^{m\sigma_2}\gamma_b^{(m)}\left[e^{im\beta(\chi_d^{2\mathrm{m}}-\chi_s^{2\mathrm{m}})t}-1\right]}{im\beta(\chi_d^{2\mathrm{m}}-\chi_s^{2\mathrm{m}})\mathcal{Q}_\beta^m}+\frac{e^{\sigma_1+\sigma_2}\gamma_{ab}\left[1-e^{-i2\beta\chi_s^{2\mathrm{m}}t}\right]}{i2\beta\chi_s^{2\mathrm{m}}\mathcal{Q}_\beta^2}\Bigg\}
\end{aligned} \quad (3.45)
$$

with $\beta=-1,0,1,2$, and

$$
\mathcal{Q}_\beta = |C_a|^2\exp\left[-i\beta(\chi_d^{2\mathrm{m}}+\chi_s^{2\mathrm{m}})t\right]+|C_b|^2\exp\left[i\beta(\chi_d^{2\mathrm{m}}-\chi_s^{2\mathrm{m}})t\right], \quad (3.46)
$$

and all the expressions should be evaluated in $\sigma_1=\ln\bar{N}_a$, $\sigma_2=\ln\bar{N}_b$. The expression of v is given in (2.53).

We check the validity of the constant loss rate approximation by numerical simulation. In Fig.3.2 (a) we show the squeezing parameter as a function of time for 1000 ^{87}Rb atoms evenly split $|C_a|^2=|C_b|^2=1/2$. The atoms in states a and b are trapped in harmonic potentials whose minima are $0.44\,\mu$m apart corresponding to an experimentally relevant situation (see chapter 6). The rate constants for the losses are different for two components. We compare the analytical solution in the constant loss rate approximation with an exact Monte-Carlo simulation. The comparison shows that our constant rate approximation is very accurate when a small fraction of particles is lost at the time at which the best squeezing is achieved. In Fig.3.2 (b) we show the corresponding total number of particles and $\langle S_z\rangle$ as a function of time. According to the figures one can see that the constant loss rate approximation neglects two effects: (i) the decrease of the loss rate in time as less and less particles are in the system, as shown in Fig.3.2 (b) (top) where N_{total} calculated from the constant rate approximation decreases faster than the one obtained from simulation; (ii) the change of the ratio $\langle\hat{N}_a\rangle/\langle\hat{N}_b\rangle$ due to the asymmetric loss rate between the two components, as shown in Fig.3.2 (b) (bottom): $\langle S_z\rangle$ in our analytical model remains constant while in the simulation it increases with time.

In Fig.3.3 we compare two cases with large asymmetric two-body losses. In (a) we consider initially $\langle N_a\rangle=\langle N_b\rangle$, which is the most favorable condition for squeezing [66]. Due to the asymmetric losses, the population ratio

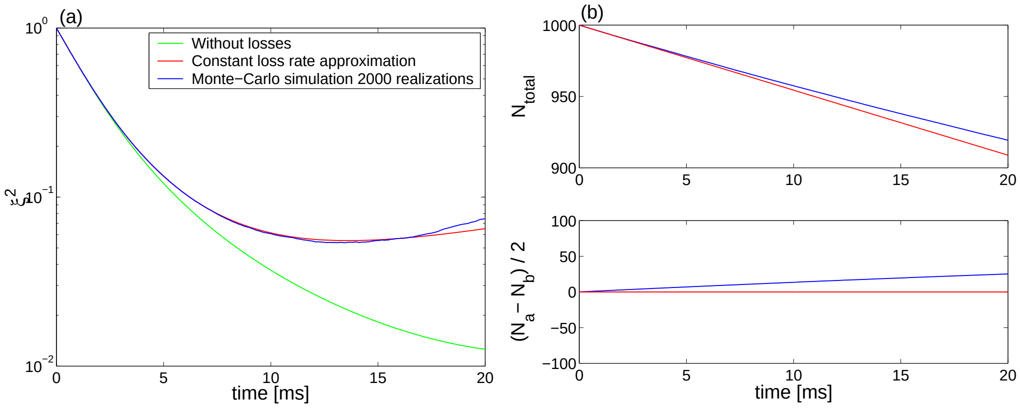

Figure 3.2: (a) Spin squeezing with one, two and three-body losses. Green solid line: squeezing parameter in the no-loss case. Red solid line: analytical solution with the constant loss rate approximation. Blue solid line: Monte-Carlo simulation with 2000 realizations. (b) Corresponding total number of particles and $\langle S_z \rangle$ as a function of time. Parameters correspond to ^{87}Rb atoms in the states $|F = 1, m_F = -1\rangle$ and $|F = 2, m_F = 1\rangle$: initial number of atoms $N = 1000$ with $\bar{N}_a = \bar{N}_b = 500$; trap frequencies $\omega_\perp = 2\pi \times 515\,\mathrm{Hz}$, $\omega_x = 2\pi \times 115\,\mathrm{Hz}$, the minimum of the two traps for a and b are separated by $0.44\,\mu\mathrm{m}$; m=87 a.m.u., $a_{aa} = 100.44\,r_B$, $a_{bb} = 95.47\,r_B$, $a_{ab} = 98.09\,r_B$, r_B is the Bohr radius. The rate constants for the losses are: $K_a^{(1)} = K_b^{(1)} = 1.0\,\mathrm{s}^{-1}$, $K_b^{(2)} = 119 \times 10^{-21}\,\mathrm{m}^3\mathrm{s}^{-1}$ [64], $K_{ab} = 78 \times 10^{-21}\,\mathrm{m}^3\mathrm{s}^{-1}$ [64], $K_a^{(3)} = 6 \times 10^{-42}\,\mathrm{m}^6\mathrm{s}^{-1}$ [65]. Using the stationary solution (2.18), these physical parameters result in $\chi_d^{2\mathrm{m}} = 0.51\,\mathrm{s}^{-1}$, $\chi_s^{2\mathrm{m}} = 0.05\,\mathrm{s}^{-1}$, $v = 51.34\,\mathrm{s}^{-1}$, $\gamma_a^{(1)} = \gamma_b^{(1)} = 0.2\,\mathrm{s}^{-1}$, $\gamma_a^{(2)} = 0$, $\gamma_b^{(2)} = 5.8 \times 10^{-3}\,\mathrm{s}^{-1}$, $\gamma_{ab}^{(2)} = 2.9 \times 10^{-3}\,\mathrm{s}^{-1}$, $\gamma_a^{(3)} = 2.55 \times 10^{-8}\,\mathrm{s}^{-1}$, $\gamma_b^{(3)} = 0$, which are directly used in two-mode model.

between the two spin components changes. The squeezing reduces as the mean spin leaves the equator and approaches the poles. However, in the constant loss rate approximation it remains constant, and consequently a better spin squeezing shall be predicted than reality. On the other hand, the fact that more particles are lost in the constant loss rate approximation makes the effect of losses on squeezing overestimated. These two effects partially compensate in the even splitting case, and we get a good agreement between the approximate solution and the exact one. In the case of (b) instead, we consider $\langle N_a \rangle \neq \langle N_b \rangle$. We initially put more particles in the high loss rate component b. Then the two effects described above add up instead of compensating each other in the constant loss rate approximation, giving a degradation of squeezing with respect to reality. Such splitting configuration, so-called breathe-together configuration will be discussed in detail in chapter 4. Note however that even for such large and highly non-symmetric losses,

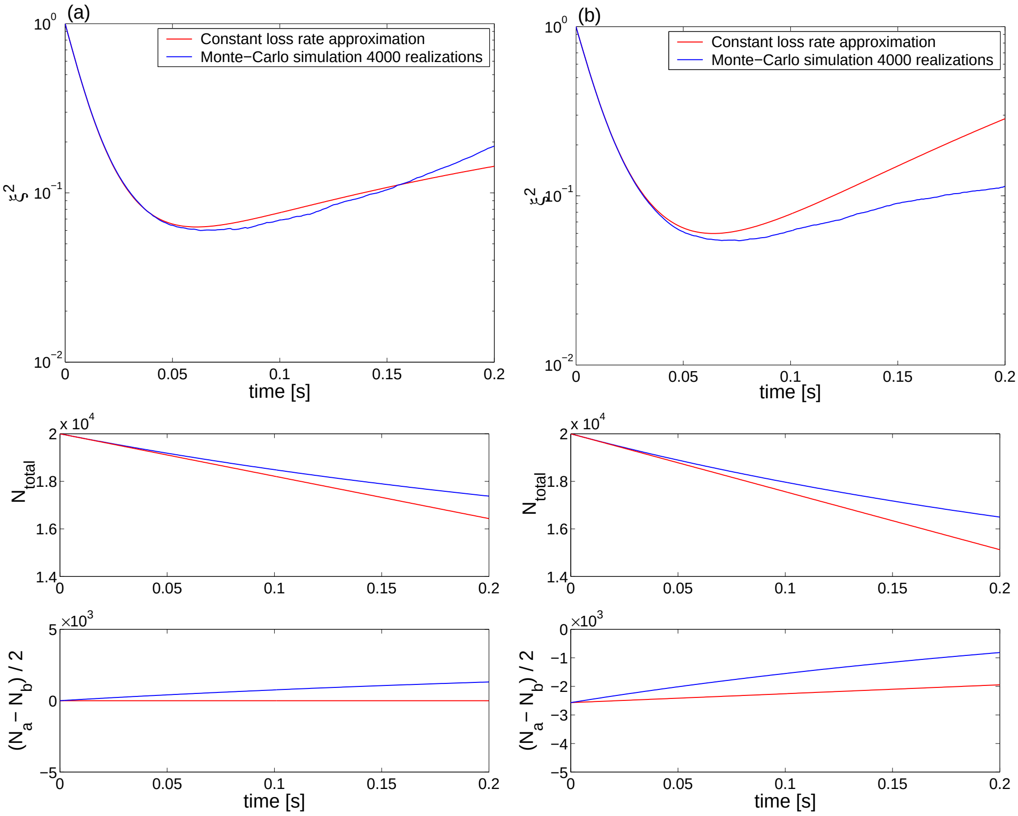

Figure 3.3: (Top) Spin squeezing with two-body losses in a bimodal condensate as a function of time. Red solid line: analytical solution with constant loss rate approximation. Blue solid line: Monte-Carlo simulation with 4000 realizations. (Bottom) Corresponding total number of particles and $\langle S_z \rangle$ as a function of time. (a) Symmetrically split condensates with $\bar{N}_a = \bar{N}_b = 10^4$. Parameters: $\chi_d^{2\mathrm{m}} = 5.38 \times 10^{-3}\,\mathrm{s}^{-1}$, $\chi_s^{2\mathrm{m}} = 5.42 \times 10^{-4}\,\mathrm{s}^{-1}$, $v = 13.88\,\mathrm{s}^{-1}$, $\gamma_a^{(2)} = 0$, $\gamma_b^{(2)} = 8.92 \times 10^{-5}\,\mathrm{s}^{-1}$. (b) Breathe-together configuration with $\bar{N}_a = 7432$ and $\bar{N}_b = 12568$. Parameters: $\chi_d^{2\mathrm{m}} = 5.39 \times 10^{-3}\,\mathrm{s}^{-1}$, $\chi_s^{2\mathrm{m}} = 1.39 \times 10^{-3}\,\mathrm{s}^{-1}$, $v = 13.85\,\mathrm{s}^{-1}$, $\gamma_a^{(2)} = 0$, $\gamma_b^{(2)} = 7.71 \times 10^{-5}\,\mathrm{s}^{-1}$, calculated from the stationary solution of Gross-Pitaevskii equation (2.18) with the trap frequency is $\omega = 2\pi \times 42.6\,\mathrm{Hz}$, m=87 a.m.u., and the scattering length $a_{aa} = 100.44\,r_B$, $a_{bb} = 95.47\,r_B$, $a_{ab} = 88.28\,r_B$, r_B is the Bohr radius. The rate constants for two-body losses are: $K_a^{(2)} = 0$, $K_b^{(2)} = 119 \times 10^{-21}\,\mathrm{m}^3\mathrm{s}^{-1}$.

the constant loss rate approximation proves to be rather accurate up to the best squeezing time.

3.2 Optimization of spin squeezing in the symmetric case

In this section, we explore the analytical solutions obtained in the constant loss rate approximation. We will concentrate on the symmetric condensates case. We assume that the two components have the same average number of atoms, scattering length, and loss rates. In this case we can carry out analytically the optimization of squeezing in presence of losses.

In the symmetric case and constant loss rate approximation it turns out that $\Delta S_z^2 = \langle \hat{N} \rangle /4$. This allows to express ξ^2 in a simple way,

$$\xi^2 = \frac{\langle a^\dagger a \rangle}{\langle b^\dagger a \rangle^2} \left(\langle a^\dagger a \rangle + \tilde{A} - \sqrt{\tilde{A}^2 + \tilde{B}^2} \right) , \tag{3.47}$$

with

$$\tilde{A} = \frac{1}{2} \operatorname{Re} \left(\langle b^\dagger a^\dagger a b - b^\dagger b^\dagger a a \rangle \right) \tag{3.48}$$

$$\tilde{B} = 2 \operatorname{Im} \left(\langle b^\dagger b^\dagger b a \rangle \right) . \tag{3.49}$$

An analytical expression for spin squeezing can be calculated from (3.36)-(3.44) with $\bar{N}_a = \bar{N}_b$, $\chi_s^{2\mathrm{m}} = 0$, $\gamma_a^{(m)} = \gamma_b^{(m)} = \gamma^{(m)}$. We shall use them to find simple results for the best squeezing and the best squeezing time in the large N limit. Let us define the rates related to the fraction of lost particles,

$$\Gamma^{(m)} = \left(\frac{N}{2} \right)^{m-1} m \gamma^{(m)} ; \qquad \Gamma_{ab} = \frac{N}{2} \gamma_{ab} . \tag{3.50}$$

The quantity $\Gamma^{(m)} t$ gives the fraction of lost particles due to m-body losses. In the absence of losses, the best squeezing and the best squeezing time in units of $1/\chi_d^{2\mathrm{m}}$ scale as $N^{-2/3}$. We then set $N = \epsilon^{-3}$ and rescale the time as $\chi_d^{2\mathrm{m}} t = \tau \epsilon^2$. We expand (3.47) for $\epsilon \ll 1$ up to order 2 included, keeping $\Gamma^{(m)} / \chi_d^{2\mathrm{m}}$ constant, we obtain:

$$\xi^2(t) = \frac{1}{N^2 (\chi_d^{2\mathrm{m}} t)^2} + \frac{1}{6} N^2 (\chi_d^{2\mathrm{m}} t)^4 + \frac{1}{3} \Gamma_{\mathrm{sq}} t, \tag{3.51}$$

where

$$\Gamma_{\mathrm{sq}} = \sum_m \Gamma_{\mathrm{sq}}^{(m)} \text{ and } \Gamma_{\mathrm{sq}}^{(m)} = m \Gamma^{(m)} . \tag{3.52}$$

The key point is that in this expansion, for large N and short times, the crossed losses ab do not contribute. Introducing the squeezing $\xi_0^2(t)$ in the no-loss case Eq.(2.35), we obtain:

$$\xi^2(t) = \xi_0^2(t)\left[1 + \frac{1}{3}\frac{\Gamma_{\rm sq} t}{\xi_0^2(t)}\right] . \tag{3.53}$$

The result (3.53) very simply accesses the impact of losses on spin squeezing. First it shows that losses cannot be neglected as soon as the lost fraction of particles is of the order of ξ_0^2. The more squeezed the state is, the more sensitive to the losses. Second, it shows that in the limit $N \to \infty$ and $\xi_0^2(t_{\rm best}) \to 0$, the squeezing in presence of losses is of the order of the lost fraction of particles at the best time: $\xi^2(t_{\rm best}) \sim \Gamma_{\rm sq} t_{\rm best}/3$. This also sets the limits of validity of our constant loss rate approximation. For our approximation to be valid, the lost fraction of particle, hence squeezing parameter at the best squeezing time, should be small.

Minimizing $\xi^2(t)$ in Eq.(3.51) with respect to t, one finds the best squeezing time and the corresponding squeezing

$$t_{\rm best} = \left[\frac{f(C)}{2}\right]^{1/3} \frac{N^{-2/3}}{\chi_d^{\rm 2m}} , \tag{3.54}$$

$$\xi^2(t_{\rm best}) = \left[\frac{1}{f(C)^{2/3}} + \frac{f(C)^{4/3}}{24} + \frac{C f(C)^{1/3}}{3}\right]\left(\frac{2}{N}\right)^{2/3} , \tag{3.55}$$

where $f(C) = \sqrt{C^2+12} - C$, $C = \Gamma_{\rm sq}/2\chi_d^{\rm 2m}$. In order to find optimal conditions to produce spin squeezing in presence of losses and set the ultimate limits of this technique, from now on, we assume that the number of particles is large enough for the condensate to be in the Thomas-Fermi regime with the scattering lengths

$$a_{ab} < a_{aa} = a_{bb} . \tag{3.56}$$

In this case, the two components of the condensate do not demix as the cross interaction energy is smaller than the self interaction energy components. We introduce the *sum* and *difference* of the intra and inter-species s-wave scattering lengths:

$$a_s = a_{aa} + a_{ab} \tag{3.57}$$

$$a_d = a_{aa} - a_{ab} . \tag{3.58}$$

In the symmetric case considered, the two components of the condensate

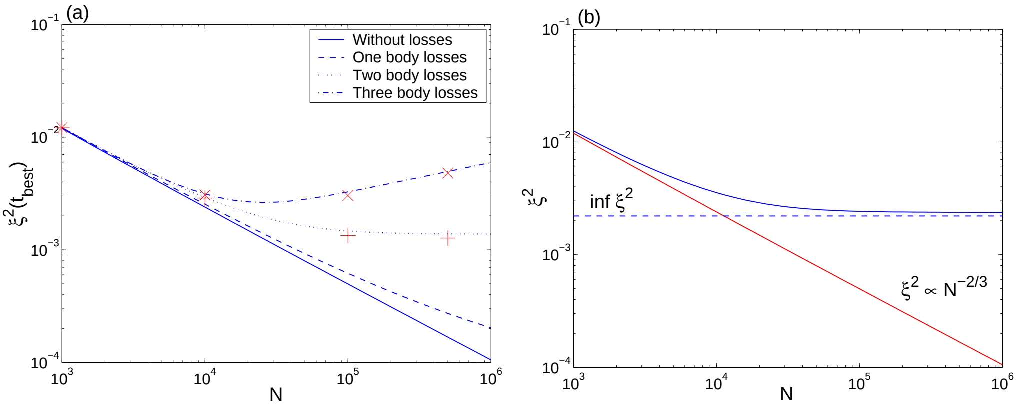

Figure 3.4: (a) Spin squeezing obtained by a minimization of ξ^2 over time in a fixed trap, as a function of the initial number of particles, calculated from Thomas-Fermi approximation (3.59)-(3.63), without loss of particles (solid line), with one-body losses (dashed line), with two-body losses (dotted line), with three-body losses (dash-dotted line), respectively. Parameters: $a_s = a_d = 5.32\,\mathrm{nm}$, $\bar{\omega} = 2\pi \times 200\,\mathrm{Hz}$, $K^{(1)} = 0.1\,\mathrm{s}^{-1}$, $K^{(2)} = 2 \times 10^{-21}\,\mathrm{m}^3/\mathrm{s}$, $K^{(3)} = 18 \times 10^{-42}\,\mathrm{m}^6/\mathrm{s}$. The symbols plus (crosses) are results of a numerical simulation with 400 Monte-Carlo realizations for two-body (three-body) losses. (b) Spin squeezing obtained at t_{best} as a function of the initial number of particles, without losses (red solid line), with one, two, and three-body losses (blue solid line), when the trap frequency is optimized for each number of particles using (3.64). The dashed line is the lower bound of spin squeezing when $N \to \infty$. The rate constants are the same as (a).

have the same profiles. Under the Thomas-Fermi approximation, we have

$$\mu_a = \mu_b = \frac{1}{2}\hbar\bar{\omega}\left[\frac{15}{2}\frac{Na_s}{a_{ho}}\right]^{2/5}, \tag{3.59}$$

$$\chi = \frac{2^{3/5}3^{2/5}}{5^{3/5}}\left(\frac{\hbar}{M}\right)^{-1/5}\bar{\omega}^{6/5}N^{-3/5}\frac{a_d}{a_s^{3/5}}, \tag{3.60}$$

$$\Gamma^{(1)} = K^{(1)}, \tag{3.61}$$

$$\Gamma^{(2)} = \frac{15^{2/5}}{2^{7/5}7\pi}\left(\frac{\hbar}{M}\right)^{-6/5}\bar{\omega}^{6/5}N^{2/5}a_s^{-3/5}K^{(2)}, \tag{3.62}$$

$$\Gamma^{(3)} = \frac{5^{4/5}}{2^{19/5}3^{1/5}7\pi^2}\left(\frac{\hbar}{M}\right)^{-12/5}\bar{\omega}^{12/5}N^{4/5}a_s^{-6/5}K^{(3)}, \tag{3.63}$$

where $a_{ho} = \sqrt{\hbar/M\bar{\omega}}$ is the harmonic oscillator length, $\bar{\omega}$ is the geometric mean of the trap frequencies. Note that for two spatially separated condensates, $a_{ab} = 0$, and $a_s = a_d$.

We first analyze the dependence of the squeezing on the initial number of particles, including separately for clarity one, two, and three-body losses. Fig.3.4 (a) shows the best squeezing $\xi^2(t_{\rm best})$ as a function of the initial atom number N when only one kind of losses is present. The trap frequency is fixed. The curve without losses proportional to $N^{-2/3}$ is also shown for comparison. We choose the parameters for the ^{87}Rb atoms in the state $|F=1\rangle$. In this case, the scattering length $a = 5.32\,\text{nm}$. According to the figure, one-body losses do not change qualitatively the picture without losses and we have $\xi^2(t_{\rm best}) \propto N^{-4/15}$ for $N \to \infty$. In the same limit, with two-body losses, $\xi^2(t_{\rm best})$ is independent of N. With three-body losses, $\xi^2(t_{\rm best}) \propto N^{4/15}$ for $N \to \infty$, implying that, for a fixed $\bar{\omega}$, there is a finite number of particles that optimizes squeezing.

In a fixed trap, when one tries to improve the squeezing by increasing the number of atoms, the density of the condensate will also increase. Therefore the three-body losses become more and more important in this case. To overcome this problem, one could, in the meantime, try to lower the density by opening the trap for example. Reducing the density decreases the fraction of lost particles due to two and three-body losses. However, the interaction parameter χ responsible for the squeezing is also reduced in this way and the squeezing time gets longer thus increasing the importance of one-body losses that are independent of the density.

The tradeoff between these two effects defines the optimum trap frequency. Note that the square brackets in Eq.(3.55) is an increasing function of C, we can then optimize $\xi^2(t_{\rm best})$ by minimizing C with respect to $\bar{\omega}$. Under the conditions $K^{(1)} \neq 0$ and $K^{(3)} \neq 0$, the minimum of C, $C_{\rm min}$ is obtained for $\Gamma^{(1)} = 3\Gamma^{(3)}$, yielding

$$\bar{\omega}^{\rm opt} = \frac{2^{19/12}7^{5/12}\pi^{5/6}}{15^{1/3}} \frac{\hbar}{M} \frac{a_s^{1/2}}{N^{1/3}} \left(\frac{K^{(1)}}{K^{(3)}}\right)^{5/12} . \tag{3.64}$$

$\bar{\omega}^{\rm opt}$ is the optimized trap frequency. Note that this optimization concerns one and three-body losses only. The effect of decoherence due to two-body losses quantified by the ratio $\Gamma^{(2)}/\chi$ is independent of the trap frequency. The best squeezing under the Thomas-Fermi approximation occurs when there is a balance between one-body and three-body losses.

Once the trap frequency is optimized, $\xi^2(t_{\rm best}, \bar{\omega}^{\rm opt})$ is a decreasing function of N, as shown in Fig.3.4 (b). The lower bound for ξ^2, reached for $N \to \infty$ is then

$$\inf_{t,\bar{\omega},N} \xi^2 = \left[\frac{5\sqrt{3}M}{28\pi\hbar}\right]^{2/3} \left[\sqrt{\frac{7}{2}\frac{K^{(1)}K^{(3)}}{a_d^2}} + \frac{K^{(2)}}{a_d}\right]^{2/3} . \tag{3.65}$$

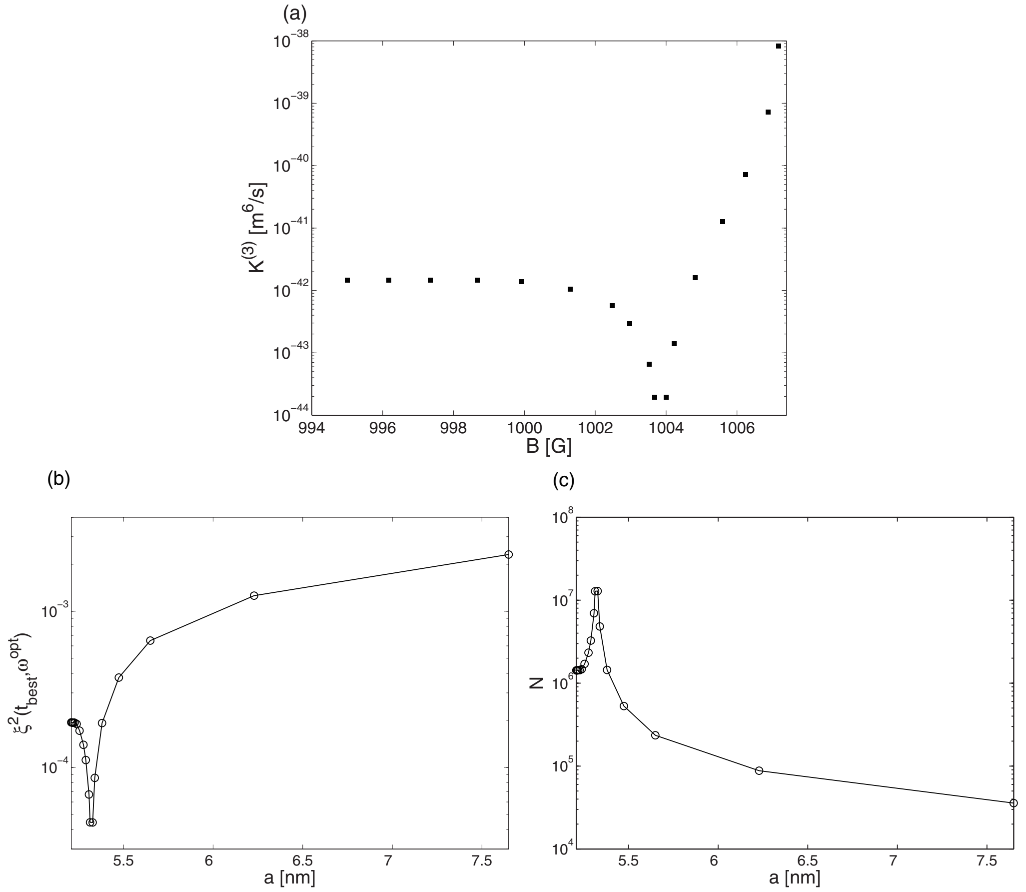

Figure 3.5: (a) Three-body recombination loss rate constant $K^{(3)}$ versus B taken from [69]. (b) Spin squeezing $\xi^2(t_{\text{best}})$ optimized with respect to $\bar{\omega}$ as a function of the scattering length a, when the magnetic field is varied on the left side of the $B_0 = 1007.4\,\text{G}$ Feshbach resonance of ^{87}Rb. (c) The number of particles for each point in (b), calculated for $\eta = 10\,\%$. $K^{(1)} = 0.01\,\text{s}^{-1}$ and $K^{(2)} = 0$.

The fact that ξ^2 is a decreasing function of N is important for broad interest applications such as spectroscopy where, apart from the gain coming from spin squeezing, one always gains in increasing N, as shown in Eq.(2.13). Another simple outcome of this analytic study is that, for positive scattering lengths a_{aa}, a_{ab}, the maximum squeezing is obtained when $a_{ab} = 0$ that is for example for spatially separated condensates. Another possibility is to use a Fechbach resonance to decrease the inter-species scattering length a_{ab} [67, 68], knowing that the crossed $a - b$ losses do not harm the squeezing at short times.

In practice, in order to approach this lower bound, one can choose $N = N_\eta$ such that $\xi^2 = (1 + \eta) \inf \xi^2$ (e.g. $\eta = 10\,\%$), then calculate the optimized trap frequency (3.64) with N_η. For a suitable choice of the internal state, in an optical trap, the two-body losses can be neglected $K^{(2)} = 0$. One can get in this case very simple formulas for the optimized parameters and squeezing. For $\eta = 10\,\%$,

$$N_\eta \simeq \frac{17.833}{[K^{(1)}K^{(3)}]^{1/2}} \frac{\hbar\, a_d}{M}\,, \tag{3.66}$$

$$t_{\text{best}} \simeq 0.277 \left[\frac{M}{\hbar K^{(1)}}\right]^{2/3} \left[\frac{K^{(3)}}{a_d^2}\right]^{1/3}\,, \tag{3.67}$$

$$\xi^2 \simeq 0.356 \left[\frac{MK^{(1)}}{\hbar}\right]^{1/3} \left[\frac{MK^{(3)}}{\hbar\, a_d^2}\right]^{1/3}\,. \tag{3.68}$$

Note that in (3.68) the scattering length appears at the denominator. We then ask ourselves whether we can use a Feshbach resonance to increase the intra-species scattering length $a = a_{aa} = a_{bb}$ (but also $K^{(3)}$) to improve the squeezing. In Fig.3.5 (b) we plot the squeezing parameter versus a assuming $a_{ab} = 0$ and $K^{(1)} = 0.01\,\text{s}^{-1}$. Predicted values of $K^{(3)}$, as a function of the magnetic field strength B, are shown in Fig.3.5 (a), which is taken from [69] for ^{87}Rb in the state $|F = 1, m_F = 1\rangle$ (theoretical work). Close to the resonance, the scattering length a as a function of B is approximately given by

$$a(B) = a_{bg}[1 - \Delta B/(B - B_0)] \tag{3.69}$$

where $B_0 = 1007.4\,\text{G}$, $\Delta B = 0.21\,\text{G}$ and $a_{bg} = 5.32\,\text{nm}$. From Eq.(3.69) plus Fig.3.5 (a), we obtain the rate constant $K^{(3)}$ as a function of a. We calculate $\bar{\omega}^{\text{opt}}$ and the number of particles needed for $\eta = 10\,\%$ for each point in the curve, see Fig.3.5 (c). Close to Feshbach resonance, the squeezing gets worse as $K^{(3)}$ increases (even if the figure we do not enter the regime $K^{(3)} \sim \hbar\, a^4/M$). The dip giving large squeezing corresponds to a strong decrease in $K^{(3)}$ around 1003.5 G ($K^{(3)} \simeq 3 \times 10^{-45}\text{m}^6/\text{s}$). In the theoretical article [69], the authors explain that it is due to an atom-dimer zero-energy resonance at this magnetic field strength. If the dip were confirmed by the experiments, it would allow a squeezing parameter $\xi^2 = 4.4 \times 10^{-5}$ to be reached.

3.3 The survival time of squeezing

As we show in chapter 2, spin squeezed states are useful resources that would allow a precision gain over the standard quantum limit in interferometric measurements. However, in order to use it, for example in atomic clocks, the squeezed state should survive during the interrogation time. In this section, we consider the problem of the survival time of a spin squeezed state in presence of losses.

We imagine that the system evolves in two periods: for $0 < t < T_1$, the system is squeezed in a tight trap with the nonlinear parameter $\chi_{d1}^{2\mathrm{m}}$, in presence of all kinds of losses; and for $T_1 < t < T_1 + T_2$, we move to a shallow trap to lower the density, consequently the nonlinear parameter is decreased $\chi_{d2}^{2\mathrm{m}} \simeq 0$. The Hamiltonian for the two periods is

$$\mathcal{H}_{0j} = f_{\hat{N}}^{(j)} + \hbar\, v_{\hat{N}}^{(j)} (\hat{N}_a - \hat{N}_b) + \frac{\hbar \chi_{dj}^{2\mathrm{m}}}{4} (\hat{N}_a - \hat{N}_b)^2 \,, \tag{3.70}$$

with $j = 1, 2$ indicating the first and second period, and

$$\begin{aligned} v_{\hat{N}}^{(j)} &= \frac{1}{2\hbar} \Big[(\mu_{aj} - \mu_{bj}) - \hbar \chi_{dj}^{2\mathrm{m}} (\bar{N}_a - \bar{N}_b) + \hbar \chi_{sj}^{2\mathrm{m}} (\hat{N} - \bar{N}) \Big] && (3.71) \\ \chi_{dj}^{2\mathrm{m}} &= \frac{1}{2\hbar} \left(\partial_{N_a} \mu_{aj} + \partial_{N_b} \mu_{bj} - \partial_{N_b} \mu_{aj} - \partial_{N_a} \mu_{bj} \right)_{\bar{N}_a, \bar{N}_b} && (3.72) \\ \chi_{sj}^{2\mathrm{m}} &= \frac{1}{2\hbar} (\partial_{N_a} \mu_{aj} - \partial_{N_b} \mu_{bj})_{\bar{N}_a, \bar{N}_b} \,. && (3.73) \end{aligned}$$

For $\chi_{d2}^{2\mathrm{m}} \simeq 0$, the effect of losses in the the second period can be briefly summarized as follows: (i) similar as the first period, each loss event in the second period will also cause a random phase shift of the state, e.g. see Eqs.(3.77) and (3.81), which degrades the relative phase between the two modes, consequently degrades the spin squeezing; (ii) in case $\chi_{s2}^{2\mathrm{m}} \neq 0$, there is extra effect: in each single trajectory, the mean spin rotates around the axis-z with the velocity depending on the remaining number of particles, therefore during the interrogation time, the loss events induce fluctuations in the direction of mean spin, which results in more phase noise.

Note that in a real Ramsey sequence using spin squeezed state, before the interrogation period starts, one has to rotate the state such that the squeezed axis is aligned along the equatorial plane of the Bloch sphere (phase squeezed state), which makes it more sensitive to phase noise. The lifetime for spin squeezed state in a real Ramsey sequence will be discussed in chapter 6.

3.3.1 Simple case with one-body losses only

In this subsection, we consider a simple symmetric case with one-body losses only in the second period. For the first period, starting with the phase state (2.20), the system evolves according to the Hamiltonian $\mathcal{H}_{01}$ described in

Eq.(3.70) with $\chi_{s1}^{2\mathrm{m}} = v_{\hat{N}1} = 0$. We again use the constant rate approximation. The effective Hamiltonian then can be approximated as in Eq.(3.31)

$$\mathcal{H}_{\mathrm{eff1}} \simeq -\frac{i\hbar}{2}\sum_{m=1}^{3}\sum_{\varepsilon=a,b}\gamma_{\varepsilon 1}^{(m)}\bar{N}_{\varepsilon}^{m} - \frac{i\hbar}{2}\gamma_{ab1}\bar{N}_a\bar{N}_b \equiv -\frac{i\hbar}{2}\lambda_1 \tag{3.74}$$

with $\gamma_{a1}^{(m)} = \gamma_{b1}^{(m)} = \gamma_1^{(m)}$ and $\bar{N}_a = \bar{N}_b = N/2$. In the second period, we assume that we change to a very shallow trap such that the interaction between the atoms is stopped, the nonlinear parameter $\chi_{d2}^{2\mathrm{m}} = 0$. The system evolves under the influence of one-body losses only. The effective Hamiltonian can be written as

$$\mathcal{H}_{\mathrm{eff2}} = -\frac{i\hbar}{2}\gamma_2^{(1)}\left(\hat{N}_a + \hat{N}_b\right) \tag{3.75}$$

The rate constants $K^{(m)}$ and K_{ab} are the same in the two periods. However, the real loss rates $\gamma_{\varepsilon j}^{(m)}$ and γ_{abj} as defined in Eq.(3.3) and (3.4) are different since the wave functions are different due to the trap configurations.

The evolution of a single quantum trajectory with k jumps at times t_j in the first period and m jumps at times t_l in the second one reads

$$\begin{aligned}|\Psi(T_1,T_2)\rangle =& e^{-\lambda_1 T_1/2}\left\{\frac{[N-N(k)]!}{[N-N(k)-m]!}\right\}^{1/2}\exp\left[-\frac{1}{2}\sum_{l=1}^{m}\gamma_2^{(1)}(t_l - T_1)\right] \\ & \cdot\,\alpha_k\tilde{\alpha}_m\hat{\mathcal{P}}_m|\varphi+\beta_k\rangle_{N-N(k)-m,\,C_a',\,C_b'}\end{aligned} \tag{3.76}$$

where α_k, β_k and $N(k)$ are defined as in Eq.(3.33)-(3.35), $\tilde{\alpha}_m$ is the same as in Eq.(3.19), $C_a' = e^{-\gamma_2^{(m)}T_2/2}C_a$, $C_b' = e^{-\gamma_2^{(m)}T_2/2}C_b$ and

$$\begin{aligned}\hat{\mathcal{P}}_m = \prod_{l=1}^{m}\Big\{&\delta_{\varepsilon_l,a}e^{-iT_1\left[v_{\hat{N}+1}^{(1)}\left(\hat{N}_a-\hat{N}_b+1\right)+\chi_{d1}^{2\mathrm{m}}\left(\hat{N}_a-\hat{N}_b+1\right)^2/4\right]} \\ &+\delta_{\varepsilon_l,b}e^{-iT_1\left[v_{\hat{N}+1}^{(1)}\left(\hat{N}_a-\hat{N}_b-1\right)+\chi_{d1}^{2\mathrm{m}}\left(\hat{N}_a-\hat{N}_b-1\right)^2/4\right]}\Big\}\,.\end{aligned} \tag{3.77}$$

After average over all possible stochastic realizations, one finds that the squeezing parameter can be written as follows,

$$\begin{aligned}\xi^2(T_1,T_2) &= \frac{1}{4}\frac{\langle\hat{N}(T_1)\rangle^2}{\langle S_x(T_1)\rangle^2} - \left[\frac{1}{4}\frac{\langle\hat{N}(T_1)\rangle^2}{\langle S_x(T_1)\rangle^2} - \xi^2(T_1)\right]e^{-\gamma_2^{(1)}T_2} \\ &\simeq 1 - \left[1-\xi^2(T_1)\right]e^{-\gamma_2^{(1)}T_2}\,.\end{aligned} \tag{3.78}$$

where in the second line we have used the fact that for $T_1 \ll 1$ one has $\langle S_x(T_1)\,\rangle \simeq N/4$. Eq.(3.78) indicates the life time of squeezing. The quantity

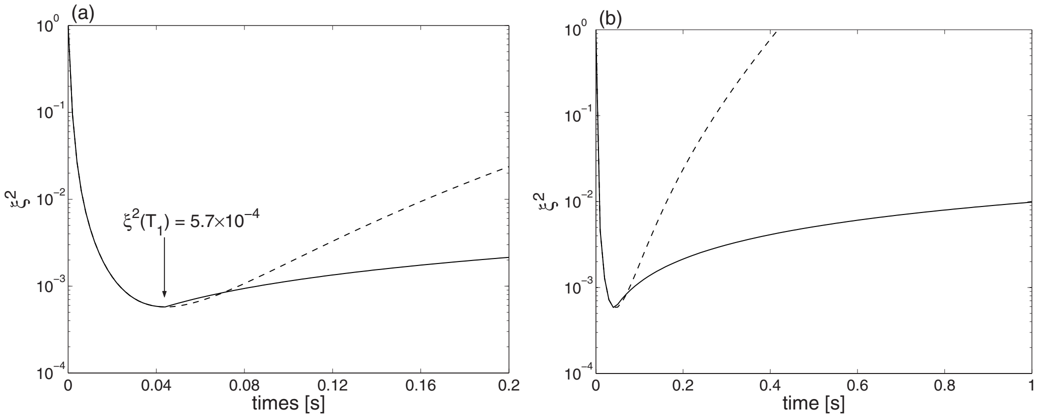

Figure 3.6: Spin squeezing ξ^2 as a function of time. The scattering length is chosen for ^{87}Rb atoms in the state $|F = 1, m_F = 1\rangle$, $a = 5.32\,\mathrm{nm}$, and the corresponding rate constants are: $K^{(1)} = 0.01\,\mathrm{s}^{-1}$, $K^{(2)} = 0$, $K^{(3)} = 6 \times 10^{-42}\,\mathrm{m}^6/\mathrm{s}$ [69]. The solid line represents the evolution consisting of two periods. In the first period, which is optimized with (3.66)-(3.68), the trap frequency is $\bar{\omega}^{\mathrm{opt}} = 2\pi \times 20.06\,\mathrm{Hz}$ and initial number of particles $N = 2.8 \times 10^5$, the best squeezing, reached at $T_1 = t_{\mathrm{best}} = 4.4 \times 10^{-2}\,\mathrm{s}$, is $\xi^2 = 5.7 \times 10^{-4}$. In the second period, we assume that the system evolves under the influence of one-body losses. The rate constants in the two periods are the same. The other parameters are calculated with Thomas-Fermi approximation (3.59)-(3.63). The dashed line represents the evolution consisting only one periods. The parameters are the same as the first period plotted with the solid line. (a) Short time behavior with $T_1 + T_2 = 0.2\,\mathrm{s}$. (b) Long time behavior with $T_1 + T_2 = 1\,\mathrm{s}$.

$1 - \xi^2$ simply decays exponentially, with the decay rate $\gamma_2^{(1)}$. This result shows that the spin squeezing can be kept some time after the interactions have been stopped. It also shows that the more squeezed the state is, the harder to keep.

To give an example, in Fig.3.6 we show a plot for ^{87}Rb atoms. We choose the scattering length of the state $|F = 1, m_F = 1\rangle$, i.e. $a = 5.32\,\mathrm{nm}$. The rate constant $K^{(1)} = 0.01\,\mathrm{s}^{-1}$, $K^{(2)} = 0$, $K^{(3)} = 6 \times 10^{-42}\,\mathrm{m}^6/\mathrm{s}$ [65]. In the optimized conditions (3.66)-(3.68) the initial number of atoms is $N = 2.8 \times 10^5$ and $\bar{\omega}^{\mathrm{opt}} = 2\pi \times 20.06\,\mathrm{Hz}$. $\xi^2 = 5.7 \times 10^{-4}$ is reached at $T_1 = t_{\mathrm{best}} = 4.4 \times 10^{-2}\,\mathrm{s}$. If we stopped the interaction at that time, as shown in the figure (solid line), a large amount of squeezing $\xi^2 \simeq 0.01$ will be still available after 1 s. On the contrary, if we continue to squeeze with $\chi_{d2}^{2\mathrm{m}} \neq 0$, as plotted in the figure (dashed line), there will be no spin squeezing after 0.4 s.

3.3.2 In presence of one, two, and three-body losses

In this subsection we give the analytical solution in presence of all kinds of losses in both periods within the constant rate approximation. The effective Hamiltonian

$$\mathcal{H}_{\mathrm{eff}j} \simeq -\frac{i\hbar}{2}\sum_{m=1}^{3}\sum_{\varepsilon=a,\,b}\gamma_{\varepsilon j}^{(m)}\bar{N}_{\varepsilon}^{m} - \frac{i\hbar}{2}\gamma_{abj}\bar{N}_a\bar{N}_b \equiv -\frac{i\hbar}{2}\lambda_j \tag{3.79}$$

The evolution of a single quantum trajectory with k jumps at times t_j in the first period and m jumps at times t_l in the second one reads

$$|\Psi(T_1,T_2)\rangle = e^{-\lambda_1 T_1/2-\lambda_2 T_2/2}\alpha_k\tilde{\alpha}_m\hat{\mathcal{O}}_m|\varphi+\beta_k+\tilde{\beta}_m\rangle_{N-N(k)-N(m)} \tag{3.80}$$

where α_k, β_k, $N(k)$ and $\tilde{\alpha}_m$, $\tilde{\beta}_k$, $N(m)$ are defined as in Eq.(3.33)-(3.35), and

$$\begin{aligned}\hat{\mathcal{O}}_m = \prod_{l=1}^{m}\Bigg\{\sum_{m'=1}^{3}\Bigg[&\delta_{\varepsilon_l,\,a}e^{-iT_1\,v^{(1)}_{(\hat{N}+m')}(\hat{N}_a-\hat{N}_b+m')-iT_1\chi_{d1}^{2\mathrm{m}}(\hat{N}_a-\hat{N}_b+m')^2/4} \\ &+\delta_{\varepsilon_l,\,b}e^{-iT_1\,v^{(1)}_{(\hat{N}+m')}(\hat{N}_a-\hat{N}_b-m')-iT_1\chi_{d1}^{2\mathrm{m}}(\hat{N}_a-\hat{N}_b-m')^2/4}\Bigg] \\ &+\delta_{\varepsilon_l,\,ab}e^{-iT_1\,v^{(1)}_{(\hat{N}+m')}(\hat{N}_a-\hat{N}_b)-iT_1\chi_{d1}^{2\mathrm{m}}(\hat{N}_a-\hat{N}_b)^2/4}\Bigg\}\,.\end{aligned} \tag{3.81}$$

The averages needed to calculate spin squeezing are

$$\begin{aligned}\langle a^\dagger a\rangle &= |C_a|^2 e^{-\lambda_1 T_1-\lambda_2 T_2}\left[N-(\partial_{\sigma_1}+\partial_{\sigma_2})-(\partial_{\tilde{\sigma}_1}+\partial_{\tilde{\sigma}_2})\right] \\ &\quad G_0(\sigma_1,\sigma_2,\tilde{\sigma}_1,\tilde{\sigma}_2) && (3.82) \\ \langle b^\dagger b\rangle &= |C_b|^2 e^{-\lambda_1 T_1-\lambda_2 T_2}\left[N-(\partial_{\sigma_1}+\partial_{\sigma_2})-(\partial_{\tilde{\sigma}_1}+\partial_{\tilde{\sigma}_2})\right] \\ &\quad G_0(\sigma_1,\sigma_2,\tilde{\sigma}_1,\tilde{\sigma}_2) && (3.83) \\ \langle a^\dagger a^\dagger aa\rangle &= |C_a|^4 e^{-\lambda_1 T_1-\lambda_2 T_2}\left[N-(\partial_{\sigma_1}+\partial_{\sigma_2})-(\partial_{\tilde{\sigma}_1}+\partial_{\tilde{\sigma}_2})-1\right] \\ &\quad \left[N-(\partial_{\sigma_1}+\partial_{\sigma_2})-(\partial_{\tilde{\sigma}_1}+\partial_{\tilde{\sigma}_2})\right]G_0(\sigma_1,\sigma_2,\tilde{\sigma}_1,\tilde{\sigma}_2) && (3.84) \\ \langle b^\dagger b^\dagger bb\rangle &= |C_b|^4 e^{-\lambda_1 T_1-\lambda_2 T_2}\left[N-(\partial_{\sigma_1}+\partial_{\sigma_2})-(\partial_{\tilde{\sigma}_1}+\partial_{\tilde{\sigma}_2})-1\right] \\ &\quad \left[N-(\partial_{\sigma_1}+\partial_{\sigma_2})-(\partial_{\tilde{\sigma}_1}+\partial_{\tilde{\sigma}_2})\right]G_0(\sigma_1,\sigma_2,\tilde{\sigma}_1,\tilde{\sigma}_2) && (3.85) \\ \langle b^\dagger a^\dagger ab\rangle &= |C_b|^2|C_a|^2 e^{-\lambda_1 T_1-\lambda_2 T_2}\left[N-(\partial_{\sigma_1}+\partial_{\sigma_2})-(\partial_{\tilde{\sigma}_1}+\partial_{\tilde{\sigma}_2})-1\right] \\ &\quad \left[N-(\partial_{\sigma_1}+\partial_{\sigma_2})-(\partial_{\tilde{\sigma}_1}+\partial_{\tilde{\sigma}_2})\right]G_0(\sigma_1,\sigma_2,\tilde{\sigma}_1,\tilde{\sigma}_2) && (3.86)\end{aligned}$$

$$\begin{aligned}
\langle b^\dagger a\rangle &= C_b^* C_b e^{-(2iv_1+\lambda_1)T_1-(2iv_2+\lambda_2)T_2}\Big[|C_a|^2 e^{-i\chi_{d1}^{\rm 2m}T_1-i\chi_{d2}^{\rm 2m}T_2} \\
&\quad + |C_b|^2 e^{i\chi_{d1}^{\rm 2m}T_1+i\chi_{d2}^{\rm 2m}T_2}\Big]^{N-1}\left[N-(\partial_{\sigma_1}+\partial_{\sigma_2})-(\partial_{\tilde\sigma_1}+\partial_{\tilde\sigma_2})\right] \\
&\quad G_1(\sigma_1,\sigma_2,\tilde\sigma_1,\tilde\sigma_2) \qquad (3.87)\\
\langle b^\dagger b^\dagger b a\rangle &= |C_b|^2 C_b^* C_a e^{-(2iv_1-i\chi_{d1}^{\rm 2m}+\lambda_1)T_1-(2iv_2-i\chi_{d2}^{\rm 2m}+\lambda_2)T_2}\Big[|C_a|^2 e^{-i\chi_{d1}^{\rm 2m}T_1-i\chi_{d2}^{\rm 2m}T_2} \\
&\quad + |C_b|^2 e^{i\chi_{d1}^{\rm 2m}T_1+i\chi_{d2}^{\rm 2m}T_2}\Big]^{N-2}\left[N-(\partial_{\sigma_1}+\partial_{\sigma_2})-(\partial_{\tilde\sigma_1}+\partial_{\tilde\sigma_2})\right] \\
&\quad \left[N-(\partial_{\sigma_1}+\partial_{\sigma_2})-(\partial_{\tilde\sigma_1}+\partial_{\tilde\sigma_2})-1\right] G_1(\sigma_1,\sigma_2,\tilde\sigma_1,\tilde\sigma_2) \qquad (3.88)\\
\langle a^\dagger a^\dagger a b\rangle &= |C_a|^2 C_a^* C_b e^{(2iv_1+i\chi_{d1}^{\rm 2m}-\lambda_1)T_1+i(2iv_2+i\chi_{d2}^{\rm 2m}-\lambda_2)T_2}\Big[|C_b|^2 e^{-i\chi_{d1}^{\rm 2m}T_1-i\chi_{d2}^{\rm 2m}T_2} \\
&\quad + |C_a|^2 e^{i\chi_{d1}^{\rm 2m}T_1+i\chi_{d2}^{\rm 2m}T_2}\Big]^{N-2}\left[N-(\partial_{\sigma_1}+\partial_{\sigma_2})-(\partial_{\tilde\sigma_1}+\partial_{\tilde\sigma_2})\right] \\
&\quad \left[N-(\partial_{\sigma_1}+\partial_{\sigma_2})-(\partial_{\tilde\sigma_1}+\partial_{\tilde\sigma_2})-1\right] G_{-1}(\sigma_1,\sigma_2,\tilde\sigma_1,\tilde\sigma_2) \qquad (3.89)\\
\langle b^\dagger b^\dagger a a\rangle &= C_b^{*2} C_a^2 e^{-(4iv_1+\lambda_1)T_1-(4iv_2+\lambda_2)T_2}\Big[|C_a|^2 e^{-2i\chi_{d1}^{\rm 2m}T_1-2i\chi_{d2}^{\rm 2m}T_2} \\
&\quad + |C_b|^2 e^{2i\chi_{d1}^{\rm 2m}T_1+2i\chi_{d2}^{\rm 2m}T_2}\Big]^{N-2}\left[N-(\partial_{\sigma_1}+\partial_{\sigma_2})-(\partial_{\tilde\sigma_1}+\partial_{\tilde\sigma_2})\right] \\
&\quad \left[N-(\partial_{\sigma_1}+\partial_{\sigma_2})-(\partial_{\tilde\sigma_1}+\partial_{\tilde\sigma_2})-1\right] G_2(\sigma_1,\sigma_2,\tilde\sigma_1,\tilde\sigma_2) \qquad (3.90)
\end{aligned}$$

where the drift velocity is

$$v_j = \frac{1}{2\hbar}\left[(\mu_a^{(j)}-\mu_b^{(j)}) - \hbar\chi_{dj}^{\rm 2m}(\bar N_a-\bar N_b) + \hbar\chi_{sj}^{\rm 2m}(N-\bar N)\right], \qquad (3.91)$$

and $\mu_a^{(j)}$, $\mu_b^{(j)}$ are the chemical potentials for component a and b in the j-th period. We introduced the function $G_\beta(\sigma_1,\sigma_2,\tilde\sigma_1,\tilde\sigma_2)$

$$\begin{aligned}
G_\beta(\sigma_1,\sigma_2,\tilde\sigma_1,\tilde\sigma_2) &= \exp\Bigg\{\sum_{m=1}^{3}\Big[\mathcal{A}_{m1}\,e^{m\sigma_1} + \mathcal{A}_{m2}\,e^{m\tilde\sigma_1-im\beta(\chi_{d1}^{\rm 2m}+\chi_{s1}^{\rm 2m})T_1} \\
&\quad + \mathcal{B}_{m1}\,e^{m\sigma_2} + \mathcal{B}_{m2}\,e^{m\tilde\sigma_2+im\beta(\chi_{d1}^{\rm 2m}-\chi_{s1}^{\rm 2m})T_1}\Big] + \frac{e^{\sigma_1+\sigma_2}\gamma_{ab1}[1-e^{-i2\beta\chi_{s1}^{\rm 2m}T_1}]}{i2\beta\chi_{s1}^{\rm 2m}\mathcal{D}_\beta^2} \\
&\quad + \frac{e^{\tilde\sigma_1+\tilde\sigma_2}\gamma_{ab2}\,e^{-i2\beta\chi_{s1}^{\rm 2m}T_1}[1-e^{-i2\beta\chi_{s2}^{\rm 2m}T_2}]}{i2\beta\chi_{s2}^{\rm 2m}\mathcal{D}_\beta^2}\Bigg\} \qquad (3.92)
\end{aligned}$$

with $\beta = -1, 0, 1, 2$,

$$\mathcal{A}_{mj} = \frac{\gamma_{aj}^{(m)} \left\{1 - \exp\left[-im\beta(\chi_{dj}^{\mathrm{2m}} + \chi_{sj}^{\mathrm{2m}})T_j\right]\right\}}{im\beta(\chi_{dj}^{\mathrm{2m}} + \chi_{sj}^{\mathrm{2m}})\mathcal{D}_\beta^m}, \tag{3.93}$$

$$\mathcal{B}_{mj} = \frac{\gamma_{bj}^{(m)} \left\{\exp\left[im\beta(\chi_{dj}^{\mathrm{2m}} - \chi_{sj}^{\mathrm{2m}})T_j\right] - 1\right\}}{im\beta(\chi_{dj}^{\mathrm{2m}} - \chi_{sj}^{\mathrm{2m}})\mathcal{D}_\beta^m}. \tag{3.94}$$

The denominator $\mathcal{D}_\beta$ is defined as

$$\begin{aligned}\mathcal{D}_\beta =& |C_a|^2 \exp\left[-i\beta(\chi_{d1}^{\mathrm{2m}} + \chi_{s1}^{\mathrm{2m}})T_1 - i\beta(\chi_{d2}^{\mathrm{2m}} + \chi_{s2}^{\mathrm{2m}})T_2\right] \\ &+ |C_b|^2 \exp\left[i\beta(\chi_{d1}^{\mathrm{2m}} - \chi_{s1}^{\mathrm{2m}})T_1 + i\beta(\chi_{d2}^{\mathrm{2m}} - \chi_{s2}^{\mathrm{2m}})T_2\right].\end{aligned} \tag{3.95}$$

All the expressions should be evaluated in $\sigma_1 = \tilde{\sigma}_1 = \ln \bar{N}_a$, $\sigma_2 = \tilde{\sigma}_2 = \ln \bar{N}_b$.

In Fig.3.7 we give an example for ^{87}Rb atoms. The parameters correspond to the states $|F = 1, m_F = -1\rangle$ and $|F = 2, m_F = 1\rangle$. We show the squeezing parameter as a function of time for the initial number of atoms $N = 1250$, evenly split. The trap frequencies in the first period are $\omega_\perp = 2\pi \times 500\,\mathrm{Hz}$, $\omega_x = 2\pi \times 109\,\mathrm{Hz}$, and in the second period $\omega_\perp = 2\pi \times 50\,\mathrm{Hz}$, $\omega_x = 2\pi \times 10\,\mathrm{Hz}$. The minima of the trap for components a and b are separated by $0.52\,\mu\mathrm{m}$ in the first period, while in the second period the two components see the same trap. The rate constants are the same throughout the whole evolution. The parameters χ, γ can be deduced from the stationary solution of Gross-Pitaevskii equation (2.18). In Fig.3.7 bottom we show the fraction of the number of particles remaining in the trap. One finds that even in such shallow trap in the second period, the fraction of lost particle due to two-body losses is still comparable with one-body losses. This is caused by the high loss rate in $F = 2$ state. The squeezing parameter $\xi^2 = 3.8 \times 10^{-2}$ is reached at $T_1 = 13.0\,\mathrm{ms}$. After transfer to the second shallow trap, the state remains squeezed until 1.0 s. Compared to the Monte-Carlo simulations, we find very good agreement with our analytical result (3.82)-(3.90).

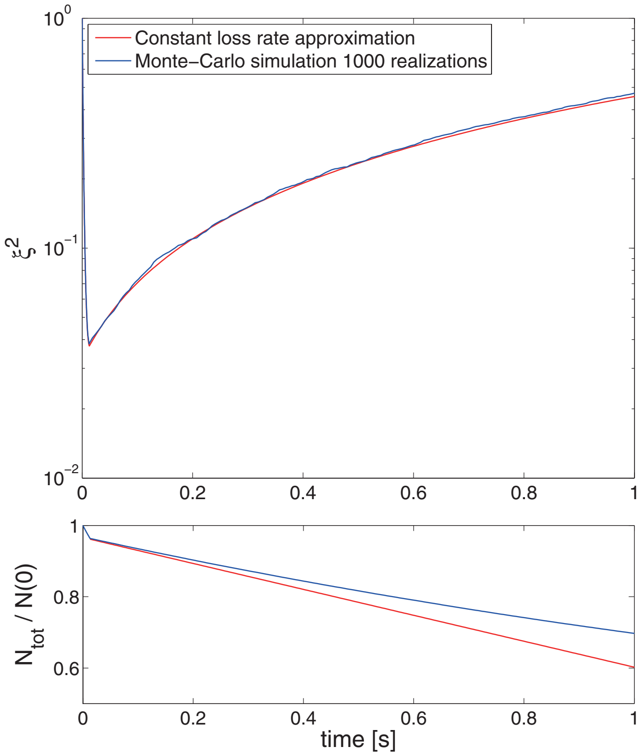

Figure 3.7: (Top) Spin squeezing ξ^2 as a function of time with one, two and three-body losses. (Bottom) Fraction of the particles remaining in the system during the evolution. Red solid line: analytical solution with constant loss rate approximation. Blue solid line: Monte-Carlo simulation with 1000 realizations. Parameters: initial number of atoms $N = 1250$ with $\bar{N}_a = \bar{N}_b = 625$; trap frequencies for the first period $\omega_\perp = 2\pi \times 500\,\mathrm{Hz}$, $\omega_x = 2\pi \times 109\,\mathrm{Hz}$, the minimum of the two traps for a and b are separated by $0.52\,\mu\mathrm{m}$; for the second period $\omega_\perp = 2\pi \times 50\,\mathrm{Hz}$, $\omega_x = 2\pi \times 10\,\mathrm{Hz}$. $m = 87\,\mathrm{a.m.u.}$. The scattering length is chosen for ^{87}Rb atoms in the state $|F = 1, m_F = -1\rangle$ and $|F = 2, m_F = 1\rangle$: $a_{aa} = 100.44\,r_B$, $a_{bb} = 95.47\,r_B$, $a_{ab} = 98.09\,r_B$, r_B is the Bohr radius. The rate constants for the losses: $K_a^{(1)} = K_b^{(1)} = 0.2\,\mathrm{s}^{-1}$, $K_b^{(2)} = 70 \times 10^{-21}\,\mathrm{m}^3\mathrm{s}^{-1}$, $K_{ab} = 50 \times 10^{-21}\,\mathrm{m}^3\mathrm{s}^{-1}$, $K_a^{(3)} = 6 \times 10^{-42}\,\mathrm{m}^6\mathrm{s}^{-1}$, which are the same for both two periods. These parameters, from the stationary solution (2.18), result in $\chi_{d1}^{2\mathrm{m}} = 0.49\,\mathrm{s}^{-1}$, $\chi_{s1}^{2\mathrm{m}} = 0.04\,\mathrm{s}^{-1}$, $\upsilon_1 = 55.03\,\mathrm{s}^{-1}$; $\chi_{d2}^{2\mathrm{m}} = 5.2 \times 10^{-5}\,\mathrm{s}^{-1}$, $\chi_{s2}^{2\mathrm{m}} = 2.0 \times 10^{-3}\,\mathrm{s}^{-1}$, $\upsilon_2 = 2.49\,\mathrm{s}^{-1}$; $\gamma_{a1}^{(1)} = \gamma_{b1}^{(1)} = \gamma_{a2}^{(1)} = \gamma_{b2}^{(1)} = 0.2\,\mathrm{s}^{-1}$, $\gamma_{b1}^{(2)} = 6.1 \times 10^{-3}\,\mathrm{s}^{-1}$, $\gamma_{b2}^{(2)} = 2.2 \times 10^{-4}\,\mathrm{s}^{-1}$, $\gamma_{ab1} = 1.4 \times 10^{-3}\,\mathrm{s}^{-1}$, $\gamma_{ab2} = 1.5 \times 10^{-4}\,\mathrm{s}^{-1}$, $\gamma_{a1}^{(3)} = 6.05 \times 10^{-8}\,\mathrm{s}^{-1}$, $\gamma_{a2}^{(3)} = 7.40 \times 10^{-11}\,\mathrm{s}^{-1}$, which are directly used in two-mode model. The time of evolution for the first period $T_1 = 13.0\,\mathrm{ms}$, and for the second period $T_2 = 1.0\,\mathrm{s}$.

Chapter 4

Spin squeezing and spatial dynamics

In the previous two chapters, we studied spin squeezing in the framework of a two-mode model, where we assume that the condensate wave functions are always in the stationary ground state. In the real experiment, a straightforward way to produce the initial phase state in a bimodal condensate is to start with one atomic condensate in a given internal state a and perform a $\pi/2$-pulse coupling coherently the internal state a to a second internal state b. However, as the strength of the interaction between two atoms $a-a$, $b-b$ and $a-b$ are in general different, the change in the mean-field energy excites the spatial dynamics of the condensate wave functions. In the evolution subsequent to the pulse, the spin dynamics creating squeezing and the spatial dynamics are entangled [23, 70, 71, 66] and occur on the same time scale set by an effective interaction parameter χ. This makes it *a priori* more difficult to obtain simple analytical results.

In this chapter we develop a simple formalism which allows us to calculate analytically or semi-analytically the effect of the spatial dynamics on spin squeezing. It neglects initial thermal excitations and reduces to the simple two-mode model described in the previous chapters for the case of stationary condensates. Using our treatment we show that at particular times in the evolution the spatial dynamics and the spin dynamics disentangle and the dynamical model gives the same result as a simple two-mode model. The main results of this chapter are published in [36].

4.1 State evolution

Our starting point is again the second quantized Hamiltonian for the two-component Bose-Einstein condensate (2.14),

$$\begin{aligned}\mathcal{H} = \sum_{\varepsilon=a,\,b} \int d^3r\, \hat{\Psi}^\dagger_\varepsilon(\mathbf{r}) h_\varepsilon \hat{\Psi}_\varepsilon(\mathbf{r}) + \sum_{\varepsilon=a,\,b} \frac{g_{\varepsilon\varepsilon}}{2} \int d^3r\, \hat{\Psi}^\dagger_\varepsilon(\mathbf{r}) \hat{\Psi}^\dagger_\varepsilon(\mathbf{r}) \hat{\Psi}_\varepsilon(\mathbf{r}) \hat{\Psi}_\varepsilon(\mathbf{r}) \\ + g_{ab} \int d^3r\, \hat{\Psi}^\dagger_a(\mathbf{r}) \hat{\Psi}^\dagger_b(\mathbf{r}) \hat{\Psi}_b(\mathbf{r}) \hat{\Psi}_a(\mathbf{r}), \qquad (4.1)\end{aligned}$$

where

$$h_\varepsilon = -\hbar^2 \nabla^2/(2M) + U^{(\varepsilon)}_{\text{ext}}(\mathbf{r}) \qquad (4.2)$$

is the one-particle Hamiltonian for atoms in state ε including the kinetic energy and external trapping potential. The field operators can be written as

$$\hat{\Psi}_a(\mathbf{r}) = a_{\langle\mathbf{r}|}, \quad \hat{\Psi}_b(\mathbf{r}) = b_{\langle\mathbf{r}|} \qquad (4.3)$$

where $a_{\langle\mathbf{r}|}$ annihilates a particle in component a at the position $\mathbf{r}$.

We assume that we start from a condensate with N atoms in the state a; the stationary wave function of the condensate is $\phi_0(\mathbf{r})$. After a $\pi/2$-pulse, the system is prepared in a phase state, where the external wave function is $\phi_0(\mathbf{r})$,

$$|\psi(0)\rangle = \frac{1}{\sqrt{N!}} \left[C_a\, a^\dagger_{|\phi_0\rangle} + C_b\, b^\dagger_{|\phi_0\rangle} \right]^N |\text{vac}\rangle \qquad (4.4)$$

The operator $a^\dagger_{|\phi_0\rangle}$ creates a particle in state a with wave function ϕ_0. Since the inter-species scattering length a_{ab} and the intra-species scattering length a_{bb} are different from a_{aa}, the sudden change in the mean-field after the pulse will excite the spatial dynamics [72]. Due again to interactions, the evolution of the spin dynamics and the spatial dynamics will be entangled. To study this problem, it is convenient to use the Fock states with a well defined number of particles in $|a\rangle$ and $|b\rangle$, these numbers being preserved during time evolution subsequent to the mixing pulse. Expanded over the Fock states, the initial state (4.4) reads:

$$|\psi(0)\rangle = \sum_{N_a=0}^{N} \left(\frac{N!}{N_a! N_b!} \right)^{1/2} C_a^{N_a} C_b^{N_b} |N_a : \phi_0, N_b : \phi_0\rangle, \qquad (4.5)$$

where $N_b = N - N_a$, and

$$|N_a : \phi_a, N_b : \phi_b\rangle = \frac{\left[a^\dagger_{|\phi_a(N_a,N_b)\rangle} \right]^{N_a}}{\sqrt{N_a!}} \frac{\left[b^\dagger_{|\phi_b(N_a,N_b)\rangle} \right]^{N_b}}{\sqrt{N_b!}} |\text{vac}\rangle\,. \qquad (4.6)$$

The commutation relations between the field operators and the creation operators $\hat{a}^{\dagger}_{|\phi_a(N_a,N_b)\rangle}$ ($\hat{b}^{\dagger}_{|\phi_b(N_a,N_b)\rangle}$) are

$$\left[\hat{a}_{\langle\mathbf{r}|}, \hat{a}^{\dagger}_{|\phi_a(N_a,N_b)\rangle}\right] = \langle\mathbf{r}|\phi_a(N_a,N_b)\rangle = \phi_a(N_a,N_b,\mathbf{r}) \tag{4.7}$$

$$\left[\hat{b}_{\langle\mathbf{r}|}, \hat{b}^{\dagger}_{|\phi_b(N_a,N_b)\rangle}\right] = \langle\mathbf{r}|\phi_b(N_a,N_b)\rangle = \phi_b(N_a,N_b,\mathbf{r}) \tag{4.8}$$

Within an Hartee-Fock type ansatz for the N-body state vector, we calculate the evolution of each Fock state in (4.5), and we get [70]:

$$\begin{aligned}&|N_a:\phi_0,\, N_b:\phi_0\rangle \rightarrow \\ &\qquad e^{-iA(N_a,N_b;t)/\hbar}|N_a:\phi_a(N_a,N_b;t),\, N_b:\phi_b(N_a,N_b;t)\rangle\,,\end{aligned} \tag{4.9}$$

where $\phi_a(N_a,N_b;t)$ and $\phi_b(N_a,N_b;t)$ are solutions of the coupled Gross-Pitaevskii equations:

$$i\hbar\frac{\partial\phi_\varepsilon}{\partial t} = \left[h_\varepsilon + (N_\varepsilon-1)g_{\varepsilon\varepsilon}|\phi_\varepsilon|^2 + N_{\varepsilon'}g_{\varepsilon\varepsilon'}|\phi_{\varepsilon'}|^2\right]\phi_\varepsilon \tag{4.10}$$

with the initial conditions

$$\phi_a(0) = \phi_b(0) = \phi_0 \tag{4.11}$$

and the time dependent phase factor A solves (see appendix C):

$$\begin{aligned}\frac{d}{dt}A(N_a,N_b;t) = &-\sum_{\varepsilon=a,b} N_\varepsilon(N_\varepsilon-1)\frac{g_{\varepsilon\varepsilon}}{2}\int d^3r|\phi_\varepsilon|^4 \\ &- N_aN_bg_{ab}\int d^3r|\phi_a|^2|\phi_b|^2\,.\end{aligned} \tag{4.12}$$

To calculate the expectation value of operators, one then has to solve (4.10) for all values of N_ε, and put back the expression (4.9) in (4.5).

With this treatment we fully include the quantum dynamics of the two condensate modes a and b, as one does for the simple two modes model, but also including the spatial dynamics of the two modes and their dependence on the number of particles. The approximation we make is to neglect all the other modes orthogonal to the condensates which would be populated thermally. An alternative method is to use a number conserving Bogoliubov theory that explicitly includes the operators of the condensates as in [71]. In that case all the modes are present but the modes orthogonal to the condensates are treated in a linearized way. In [71] the author compares this number conserving Bogoliubov approach to our approach, which is also used in [23], and he finds very similar result for the spin squeezing. He also finds that within his treatment the thermally excited modes strictly do not affect the squeezing in the scheme we consider here. If the perturbative method has the advantage of being systematic, our approach, supplemented with a further approximation (the modulus-phase approximation introduced in section 4.2) allows us to get some insight and obtain simple analytical results.

Similarly as in Eq.(2.28)-(2.30), we introduce three spin operators expressed in terms of field operators [23]

$$S_x = \frac{1}{2}\int d^3r[\hat{\Psi}_b^\dagger(\mathbf{r})\hat{\Psi}_a(\mathbf{r}) + \hat{\Psi}_a^\dagger(\mathbf{r})\hat{\Psi}_b(\mathbf{r})], \tag{4.13}$$

$$S_y = \frac{i}{2}\int d^3r[\hat{\Psi}_b^\dagger(\mathbf{r})\hat{\Psi}_a(\mathbf{r}) - \hat{\Psi}_a^\dagger(\mathbf{r})\hat{\Psi}_b(\mathbf{r})], \tag{4.14}$$

$$S_z = \frac{1}{2}\int d^3r[\hat{\Psi}_a^\dagger(\mathbf{r})\hat{\Psi}_a(\mathbf{r}) - \hat{\Psi}_b^\dagger(\mathbf{r})\hat{\Psi}_b(\mathbf{r})]. \tag{4.15}$$

Definitions (4.13)-(4.15) explicitly take into account the spatial wave functions of the condensate and depend in particular on the overlap between the two modes. By using Eqs.(2.44)-(2.47), the spin squeezing then can be calculated in terms of averages of field operators products (see appendix A). The state of the system at time t is obtained by evolving Eq.(4.4) with Eq.(4.9). To calculate the averages on needs to compute the action of the field operators $\hat{\Psi}_a$ and $\hat{\Psi}_b$ on the Fock state (4.6). By using the commutators (4.7) and (4.8), one has

$$\begin{aligned}&\hat{\Psi}_a(\mathbf{r})|N_a:\phi_a(N_a,N_b),N_b:\phi_b(N_a,N_b)\rangle\\ &\qquad=\phi_a(N_a,N_b,\mathbf{r})\sqrt{N_a}|N_a-1:\phi_a(N_a,N_b),N_b:\phi_b(N_a,N_b)\rangle,\end{aligned} \tag{4.16}$$

$$\begin{aligned}&\hat{\Psi}_b(\mathbf{r})|N_a:\phi_a(N_a,N_b),N_b:\phi_b(N_a,N_b)\rangle\\ &\qquad=\phi_b(N_a,N_b,\mathbf{r})\sqrt{N_b}|N_a:\phi_a(N_a,N_b),N_b-1:\phi_b(N_a,N_b)\rangle.\end{aligned} \tag{4.17}$$

The explicit expression of the averages that are needed to calculate the spin squeezing parameter are given as follows,

$$\begin{aligned}&\langle\hat{\Psi}_b^\dagger(\mathbf{r})\hat{\Psi}_a(\mathbf{r})\rangle\\ &=\sum_{N_a=1}^{N}\frac{N!}{(N_a-1)!N_b!}|C_a|^{2(N_a-1)}|C_b|^{2N_b}C_b^*C_a\,\phi_b^*(N_a-1,N_b+1,\mathbf{r})\phi_a(N_a,N_b,\mathbf{r})\\ &\quad e^{i[A(N_a-1,N_b+1)-A(N_a,N_b)]/\hbar}[\langle\phi_a(N_a-1,N_b+1)|\phi_a(N_a,N_b)\rangle]^{N_a-1}\\ &\quad[\langle\phi_b(N_a-1,N_b+1)|\phi_b(N_a,N_b)\rangle]^{N_b-1},\end{aligned} \tag{4.18}$$

$$\begin{aligned}
&\langle\hat{\Psi}_b^\dagger(\mathbf{r})\hat{\Psi}_a^\dagger(\mathbf{r}')\hat{\Psi}_a(\mathbf{r})\hat{\Psi}_b(\mathbf{r}')\rangle\\
=&\sum_{N_a=1}^{N}\frac{N!}{(N_a-1)!(N_b-1)!}|C_a|^{2N_a}|C_b|^{2N_b}\,\phi_b^*(N_a,N_b,\mathbf{r})\phi_a^*(N_a,N_b,\mathbf{r}')\\
&\phi_a(N_a,N_b,\mathbf{r})\phi_b(N_a,N_b,\mathbf{r}')[\langle\phi_a(N_a-2,N_b+2)|\phi_a(N_a,N_b)\rangle]^{N_a-1}\\
&[\langle\phi_b(N_a-2,N_b+2)|\phi_b(N_a,N_b)\rangle]^{N_b-1}\,,
\end{aligned}\tag{4.19}$$

$$\begin{aligned}
&\langle\hat{\Psi}_b^\dagger(\mathbf{r})\hat{\Psi}_b^\dagger(\mathbf{r}')\hat{\Psi}_a(\mathbf{r})\hat{\Psi}_a(\mathbf{r}')\rangle\\
=&\sum_{N_a=1}^{N}\frac{N!}{(N_a-2)!N_b!}|C_a|^{2(N_a-2)}|C_b|^{2N_b}C_b^{*2}C_a^2\,\phi_b^*(N_a-2,N_b+2,\mathbf{r})\\
&\phi_b^*(N_a-2,N_b+2,\mathbf{r}')\phi_a(N_a,N_b,\mathbf{r})\phi_a(N_a,N_b,\mathbf{r}')e^{i[A(N_a-2,N_b+2)-A(N_a,N_b)]/\hbar}\\
&[\langle\phi_a(N_a-2,N_b+2)|\phi_a(N_a,N_b)\rangle]^{N_a-2}[\langle\phi_b(N_a-2,N_b+2)|\phi_b(N_a,N_b)\rangle]^{N_b}\,,
\end{aligned}\tag{4.20}$$

$$\begin{aligned}
&\langle\hat{\Psi}_b^\dagger(\mathbf{r})\hat{\Psi}_b^\dagger(\mathbf{r}')\hat{\Psi}_b(\mathbf{r})\hat{\Psi}_a(\mathbf{r}')\rangle\\
=&\sum_{N_a=1}^{N}\frac{N!}{(N_a-1)!(N_b-1)!}|C_a|^{2(N_a-1)}|C_b|^{2N_b}C_b^*C_a\,\phi_b^*(N_a-1,N_b+1,\mathbf{r})\\
&\phi_b^*(N_a-1,N_b+1,\mathbf{r}')\phi_b(N_a,N_b,\mathbf{r})\phi_a(N_a,N_b,\mathbf{r}')e^{i[A(N_a-1,N_b+1)-A(N_a,N_b)]/\hbar}\\
&[\langle\phi_a(N_a-1,N_b+1)|\phi_a(N_a,N_b)\rangle]^{N_a-1}[\langle\phi_b(N_a-1,N_b+1)|\phi_b(N_a,N_b)\rangle]^{N_b-1}\,,
\end{aligned}\tag{4.21}$$

$$\begin{aligned}
&\langle\hat{\Psi}_a^\dagger(\mathbf{r})\hat{\Psi}_a^\dagger(\mathbf{r}')\hat{\Psi}_a(\mathbf{r})\hat{\Psi}_b(\mathbf{r}')\rangle\\
=&\sum_{N_a=1}^{N}\frac{N!}{(N_a-1)!(N_b-1)!}|C_a|^{2N_a}|C_b|^{2(N_b-1)}C_a^*C_b\,\phi_a^*(N_a+1,N_b-1,\mathbf{r})\\
&\phi_a^*(N_a+1,N_b-1,\mathbf{r}')\phi_a(N_a,N_b,\mathbf{r})\phi_b(N_a,N_b,\mathbf{r}')e^{i[A(N_a+1,N_b-1)-A(N_a,N_b)]/\hbar}\\
&[\langle\phi_a(N_a+1,N_b-1)|\phi_a(N_a,N_b)\rangle]^{N_a-1}[\langle\phi_b(N_a+1,N_b-1)|\phi_b(N_a,N_b)\rangle]^{N_b-1}\,.
\end{aligned}\tag{4.22}$$

These quantum averages correspond to an initial state with a well-defined total number of particles N. In case of fluctuations in the total number of particles, where the density matrix of the system is a statistical mixture of states with a different number of particles, a further averaging of N over a probability distribution $P(N)$ is needed.

To calculate above quantum averages, I have written a collection of simulation routines in Fortran including (i) the solution of the stationary of Gross-Pitaevskii equations for the initial wave function ϕ_0, and (ii) dynamical evolutions described by Eq.(4.10). The wave functions ϕ_a and ϕ_b will be used to calculate the quantum averages (4.18)-(4.22), from which the squeezing parameter can be deduced. These simulations will be used to compare with our semi-analytical approach in the following sections. To find the initial wave function, we use the conjugate gradient method to find the ground state of GP (see appendix D). Such method is also used in the simulations in a double well potential to look for the first excitation state of GP (see chapter 7). For the dynamical evolution, our simulations are based on spectral methods. In three dimensions and in the absence of particular symmetries (e.g. spherical symmetry), they can only be carried out on a cluster machine (see chapter 6) due to the fact that there are many GP for different N_ε to evolve. The calculations can be greatly simplified by using our semi-analytical approach as shown in the next section.

4.2 Dynamical modulus-phase approach

4.2.1 General model

For a large number of atoms and especially in three dimensions, the procedure described in the previous section relying on the solution of (4.10) and (4.12) for a large number of Fock states can be a very heavy numerical task. To overcome this difficulty, in order to develop an analytical approach, we can exploit the fact that for large N in the initial state (4.5) the distributions of the number of atoms N_a and N_b are very peaked around their average values with a typical width of order $\sqrt{N}$. Moreover, assuming that possible fluctuations in the total number of particles are described by a distribution $P(N)$ having a width much smaller than the average of the total number of particles $\bar{N}$, we can limit to N_a and N_b close to $\bar{N}_a = |C_a|^2\bar{N}$ and $\bar{N}_b = |C_b|^2\bar{N}$. We then split the condensate wave function into modulus and phase,

$$\phi_\varepsilon = |\phi_\varepsilon| \exp(i\theta_\varepsilon) \qquad \varepsilon = a, b\,, \tag{4.23}$$

and we assume that the variation of the modulus over the distribution of N_ε can be neglected while we approximate the variation of the phase by a linear expansion around $\bar{N}_\varepsilon$ [70]. The approximate condensate wave functions read

$$\phi_\varepsilon(N_a, N_b) \simeq \bar{\phi}_\varepsilon \exp\left[i \sum_{\varepsilon'=a,b} (N_{\varepsilon'} - \bar{N}_{\varepsilon'})(\partial_{N_{\varepsilon'}}\theta_\varepsilon)_{\bar{N}_a,\bar{N}_b} \right] \tag{4.24}$$

where $\bar{\phi}_\varepsilon \equiv \phi_\varepsilon(N_a = \bar{N}_a, N_b = \bar{N}_b)$. Note that the wave functions as well as their phases discussed in this chapter depend on time and space. For simplicity, in the following, we omit the label t for all expressions, and the label t and $\mathbf{r}$ for ϕ_ε and θ_ε.

The modulus phase approximation takes into account, in an approximate way, the dependence of the condensate wave function on the number of particles. It is precisely this effect that is responsible of entanglement between spatial dynamics and spin dynamics. Introducing time and position dependent quantities,

$$\chi_d(\mathbf{r}) = \frac{1}{2}\left[(\partial_{N_a} - \partial_{N_b})(\theta_a - \theta_b)\right]_{\bar{N}_a,\bar{N}_b} , \tag{4.25}$$

$$\chi_s(\mathbf{r}) = \frac{1}{2}\left[(\partial_{N_a} + \partial_{N_b})(\theta_a - \theta_b)\right]_{\bar{N}_a,\bar{N}_b} , \tag{4.26}$$

$$\chi_0(\mathbf{r}) = \frac{1}{2}\left[(\partial_{N_a} - \partial_{N_b})(\theta_a + \theta_b)\right]_{\bar{N}_a,\bar{N}_b} , \tag{4.27}$$

the scalar product of the wave vectors can then be written as

$$\begin{aligned}&\langle\phi_a(N_a-\beta, N_b+\beta)|\phi_a(N_a,N_b)\rangle\\ &\quad= \int d^3r|\bar{\phi}_a(\mathbf{r})|^2 \exp\{i\beta[\chi_0(\mathbf{r}) + \chi_d(\mathbf{r})]\} ,\end{aligned} \tag{4.28}$$

$$\begin{aligned}&\langle\phi_b(N_a-\beta, N_b+\beta)|\phi_b(N_a,N_b)\rangle\\ &\quad= \int d^3r|\bar{\phi}_b(\mathbf{r})|^2 \exp\{i\beta[\chi_0(\mathbf{r}) - \chi_d(\mathbf{r})]\} ,\end{aligned} \tag{4.29}$$

$$\begin{aligned}&\langle\phi_b(N_a-\beta, N_b+\beta)|\phi_a(N_a,N_b)\rangle\\ &\quad= \int d^3r\bar{\phi}_b^*(\mathbf{r})\bar{\phi}_a(\mathbf{r}) \exp[i(N_a-\beta)\chi_d(\mathbf{r}) - iN_b\chi_d(\mathbf{r})]\exp[i\beta\chi_0(\mathbf{r})]\\ &\qquad \exp[i(N-\bar{N})\chi_s(\mathbf{r}) - iN(|C_a|^2 - |C_b|^2)\chi_d(\mathbf{r})]\end{aligned} \tag{4.30}$$

$$\begin{aligned}&\langle\phi_a(N_a+\beta, N_b-\beta)|\phi_b(N_a,N_b)\rangle\\ &\quad= \int d^3r\bar{\phi}_a^*(\mathbf{r})\bar{\phi}_b(\mathbf{r}) \exp[-iN_a\chi_d(\mathbf{r}) + i(N_b-\beta)\chi_d(\mathbf{r})]\exp[-i\beta\chi_0(\mathbf{r})]\\ &\qquad \exp[-i(N-\bar{N})\chi_s(\mathbf{r}) - iN(|C_a|^2 - |C_b|^2)\chi_d(\mathbf{r})]\end{aligned} \tag{4.31}$$

where $\beta = -1, 1, 2$. By using the Gross-Pitaevskii equations (4.10) for $\phi_\varepsilon(N_a, N_b)$ and for $\phi_\varepsilon(\bar{N}_a, \bar{N}_b)$, one obtains

$$\begin{aligned}&i\hbar\frac{\partial}{\partial t}\left[(N_a - \bar{N}_a)\frac{\partial\theta_\varepsilon}{\partial N_a}|_{\bar{N}_a,\bar{N}_b} + (N_b - \bar{N}_b)\frac{\partial\theta_\varepsilon}{\partial N_b}|_{\bar{N}_a,\bar{N}_b}\right]\\ =&(N_\varepsilon - \bar{N}_\varepsilon)g_{\varepsilon\varepsilon}|\phi_\varepsilon|^4 + (N_{\varepsilon'} - \bar{N}_{\varepsilon'})g_{\varepsilon\varepsilon'}|\phi_\varepsilon|^2|\phi_{\varepsilon'}|^2\end{aligned} \tag{4.32}$$

where $\varepsilon \neq \varepsilon' = a, b$. Using (4.32) together with the initial condition (4.11), we obtain the terms concerned the phase factor A in Eq.(4.12)

$$\begin{aligned} &[A(N_a-1, N_b+1) - A(N_a, N_b)]/\hbar \\ =& -(N_a-1)\int d^3r|\bar{\phi}_a|^2[\chi_0(\mathbf{r})+\chi_d(\mathbf{r})] - N_b\int d^3r|\bar{\phi}_b|^2[\chi_0(\mathbf{r})-\chi_d(\mathbf{r})]\,, \end{aligned} \tag{4.33}$$

and

$$\begin{aligned} &[A(N_a-2, N_b+2) - A(N_a, N_b)]/\hbar \\ =& -2(N_a-2)\int d^3r|\bar{\phi}_a|^2[\chi_0(\mathbf{r})+\chi_d(\mathbf{r})] - 2N_b\int d^3r|\bar{\phi}_b|^2[\chi_0(\mathbf{r})-\chi_d(\mathbf{r})] \\ &-\int d^3r\{|\bar{\phi}_a|^2[\chi_0(\mathbf{r})+\chi_d(\mathbf{r})] + |\bar{\phi}_b|^2[\chi_0(\mathbf{r})-\chi_d(\mathbf{r})]\}\,. \end{aligned} \tag{4.34}$$

The averages and variances of the spin operators (4.13)-(4.15) are obtained by using (4.18)-(4.22) after spatial integration,

$$\begin{aligned} &\int d^3r\langle\hat{\psi}_b^\dagger(\mathbf{r})\hat{\psi}_a(\mathbf{r})\rangle \\ =&NC_b^*C_a\int d^3r\bar{\phi}_b^*(\mathbf{r})\bar{\phi}_a(\mathbf{r})\left[|C_a|^2e^{i\chi_d(\mathbf{r})} + |C_b|^2e^{-i\chi_d(\mathbf{r})}\right]^{N-1} \\ &\cdot\exp\left[-i\bar{N}\left(|C_a|^2-|C_b|^2\right)\chi_d(\mathbf{r}) + i(N-\bar{N})\chi_s(\mathbf{r}) + i\chi_0(\mathbf{r})\right]\mathcal{F}_1\,, \end{aligned} \tag{4.35}$$

$$\begin{aligned} &\int d^3rd^3r'\langle\hat{\psi}_b^\dagger(\mathbf{r})\hat{\psi}_a^\dagger(\mathbf{r}')\hat{\psi}_a(\mathbf{r})\hat{\psi}_b(\mathbf{r}')\rangle \\ =&N(N-1)|C_a|^2|C_b|^2\int d^3rd^3r'\bar{\phi}_b^*(\mathbf{r})\bar{\phi}_a(\mathbf{r})\bar{\phi}_a^*(\mathbf{r}')\bar{\phi}_b(\mathbf{r}')\,, \end{aligned} \tag{4.36}$$

$$\begin{aligned} &\int d^3rd^3r'\langle\hat{\psi}_b^\dagger(\mathbf{r})\hat{\psi}_b^\dagger(\mathbf{r}')\hat{\psi}_a(\mathbf{r})\hat{\psi}_a(\mathbf{r}')\rangle \\ =&N(N-1)C_b^{*2}C_a^2\int d^3rd^3r'\bar{\phi}_b^*(\mathbf{r})\bar{\phi}_a(\mathbf{r})\bar{\phi}_b^*(\mathbf{r}')\bar{\phi}_a(\mathbf{r}')\left[|C_a|^2e^{i\chi_d(\mathbf{r})+i\chi_d(\mathbf{r}')}\right. \\ &\left.+|C_b|^2e^{-i\chi_d(\mathbf{r})-i\chi_d(\mathbf{r}')}\right]^{N-2}\exp\left\{-i\bar{N}(|C_a|^2-|C_b|^2)\left[\chi_d(\mathbf{r})+\chi_d(\mathbf{r}')\right]\right\} \\ &\cdot\exp\left\{2i\left[\chi_0(\mathbf{r})+\chi_0(\mathbf{r}')\right] + i(N-\bar{N})\left[\chi_s(\mathbf{r})+\chi_s(\mathbf{r}')\right]\right\}\mathcal{F}_2\,. \end{aligned} \tag{4.37}$$

$$\begin{aligned} &\int d^3rd^3r'\langle\hat{\psi}_b^\dagger(\mathbf{r})\hat{\psi}_b^\dagger(\mathbf{r}')\hat{\psi}_b(\mathbf{r})\hat{\psi}_a(\mathbf{r}')\rangle \\ =&N(N-1)C_b^*C_a|C_b|^2\int d^3r\bar{\phi}_b^*(\mathbf{r})\bar{\phi}_a(\mathbf{r})\left[|C_a|^2e^{i\chi_d(\mathbf{r})} + |C_b|^2e^{-i\chi_d(\mathbf{r})}\right]^{N-2} \\ &\cdot\exp\left\{-i\left[\bar{N}(|C_a|^2-|C_b|^2)+1\right]\chi_d(\mathbf{r}) + i\chi_0(\mathbf{r}) + i(N-\bar{N})\chi_s(\mathbf{r})\right\}\mathcal{F}_1 \end{aligned} \tag{4.38}$$

$$
\begin{aligned}
&\int d^3r d^3r' \langle \hat{\psi}_a^\dagger(\mathbf{r}) \hat{\psi}_a^\dagger(\mathbf{r}') \hat{\psi}_a(\mathbf{r}) \hat{\psi}_b(\mathbf{r}') \rangle \\
=&N(N-1) C_a^* C_b |C_a|^2 \int d^3r \bar{\phi}_a^*(\mathbf{r}) \bar{\phi}_b(\mathbf{r}) \left[|C_a|^2 e^{-i\chi_d(\mathbf{r})} + |C_b|^2 e^{i\chi_d(\mathbf{r})} \right]^{N-2} \\
&\cdot \exp\left\{ i \left[\bar{N}(|C_a|^2 - |C_b|^2) - 1 \right] \chi_d(\mathbf{r}) - i\chi_0(\mathbf{r}) - i(N-\bar{N})\chi_s(\mathbf{r}) \right\} \mathcal{F}_{-1} \,.
\end{aligned}
\tag{4.39}
$$

where we have defined

$$
\begin{aligned}
\mathcal{F}_\beta = &\exp\left\{ i \left[A(N_a - \beta, N_b + \beta) - A(N_a, N_b) \right] / \hbar \right\} \\
&\cdot \left[\langle \phi_a(N_a - \beta, N_b + \beta) | \phi_a(N_a, N_b) \rangle \right]^{N_a - \beta - \delta_{\beta,-1}} \\
&\cdot \left[\langle \phi_b(N_a - \beta, N_b + \beta) | \phi_b(N_a, N_b) \rangle \right]^{N_b - \delta_{\beta,-1}} \,.
\end{aligned}
\tag{4.40}
$$

For the calculations we have used Eqs.(4.28)-(4.31) and (4.33)-(4.34). All quantities can be written in terms of the wave functions $\phi_\varepsilon(\bar{N}_a, \bar{N}_b)$, and the quantities χ_d, χ_s, χ_0 defined (4.25)-(4.27). In some cases (see subsection 4.2.2) these quantities can be explicitly calculated analytically. In the general case, it is sufficient to evolve five coupled Gross-Pitaevskii equations (4.10) to get the wave functions $\phi_a(\mathbf{r}, t)$, $\phi_b(\mathbf{r}, t)$ for $(\bar{N}_a, \bar{N}_b \pm \delta N_b)$ and $(\bar{N}_a \pm \delta N_a, \bar{N}_b)$ with $\delta N_{a,b} \neq 0$ (to calculate numerically χ_d, χ_s, χ_0), and with $\delta N_{a,b} = 0$ (to calculate the central wave functions $\bar{\phi}_{a,b}$). Although we do not expect a perfect quantitative agreement with the full numerical model for all values of parameters (see Fig.4.1 and Fig.4.3), we will see that the analytical model catches the main features and allows us to interpret simply the results.

In the particular case of stationary wave functions of the condensates, the phase of the condensate simply depends on the chemical potential. The parameters χ_d, χ_s and χ_0 become space-independent:

$$
\chi_d^{\mathrm{st}} = -\frac{t}{2\hbar} \left[(\partial_{N_a} - \partial_{N_b})(\mu_a - \mu_b) \right]_{\bar{N}_a, \bar{N}_b} \tag{4.41}
$$

$$
\chi_s^{\mathrm{st}} = -\frac{t}{2\hbar} \left[(\partial_{N_a} + \partial_{N_b})(\mu_a - \mu_b) \right]_{\bar{N}_a, \bar{N}_b} \tag{4.42}
$$

$$
\chi_0^{\mathrm{st}} = \chi_s^{\mathrm{st}} \,. \tag{4.43}
$$

In this case we recover the two-mode model explored in chapter 2 and chapter 3. The nonlinear parameter χ_d^{2m}, χ_s^{2m}, and χ_0^{2m} introduced in chapter 2 can be written in terms of Eqs.(4.41)-(4.43), $\chi_d^{\mathrm{2m}} = -\chi_d^{\mathrm{st}}/t$ and $\chi_s^{\mathrm{2m}} = -\chi_s^{\mathrm{st}}/t$.

To test our modulus-phase dynamical model, in Fig.4.1, we consider a situation in which the external dynamics is significantly excited after the $\pi/2$-pulse which populates the state b. Parameters correspond to a bimodal Rb condensate in $|F=1, m_F=1\rangle$ and $|F=2, m_F=-1\rangle$ with $\bar{N}_a = \bar{N}_b = 5 \times 10^4$ and where a Feshbach resonance is used to reduce a_{ab} by about 10% with respect to its bare value [67, 68]. The considered harmonic

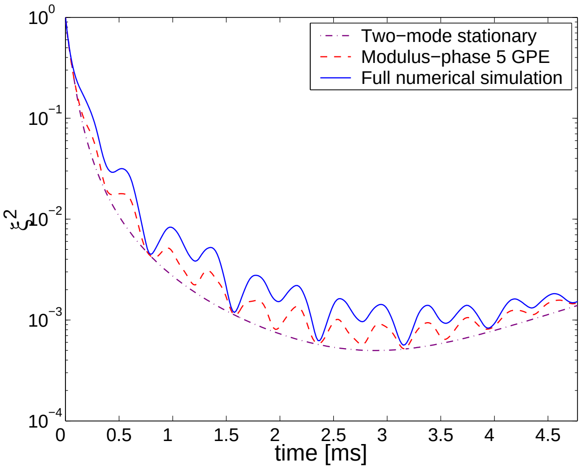

Figure 4.1: Spin squeezing as a function of time in the cases in which the spatial dynamics is strongly excited after the $\pi/2$-pulse populating a second internal state. Blue solid line: full numerical calculation with 3000 Fock states. Red dashed line: modulus-phase model. Violet dash-dotted line: stationary two-mode model using (4.41)-(4.43). Parameters: $\omega = 2\pi \times 2\,\text{kHz}$, m=87 a.m.u., $a_{aa} = 100.44\,r_B$, $a_{bb} = 95.47\,r_B$, $a_{ab} = 88.28\,r_B$. No particle losses. r_B is the Bohr radius.

trap is very steep $\omega = 2\pi \times 2$ kHz. In the figure we compare our modulus-phase approach (dashed line) with the full numerical solution (solid line) and with a stationary calculation using (4.41)-(4.42) (dash-dotted line) which is equivalent to the two-mode model. The oscillation of the squeezing parameter in the two dynamical calculations (dashed line and solid line) are due to the fact that the sudden change in the mean-field causes oscillations in the wave functions whose amplitude and the frequency are different for each Fock state. From the figure, we find that our modulus-phase approach obtained by integrating 5 Gross-Pitaevskii equations (dashed line) reproduces the main characteristics of the full numerical simulation using 3000 Fock states (solid line). The stationary two mode model on the other hand is not a very good approximation in this case. Only for some particular times the three curves almost touch. At these times the wave functions of all the Fock states almost overlap and, as we will show in our analytical treatment, spatial dynamics and spin dynamics disentangle.

In Fig.4.2 (a) we move to a shallow trap and less atoms. We note that in this case both the modulus-phase curve and the numerical simulation are very close to the stationary two-mode model which is then a good approximation at all times.

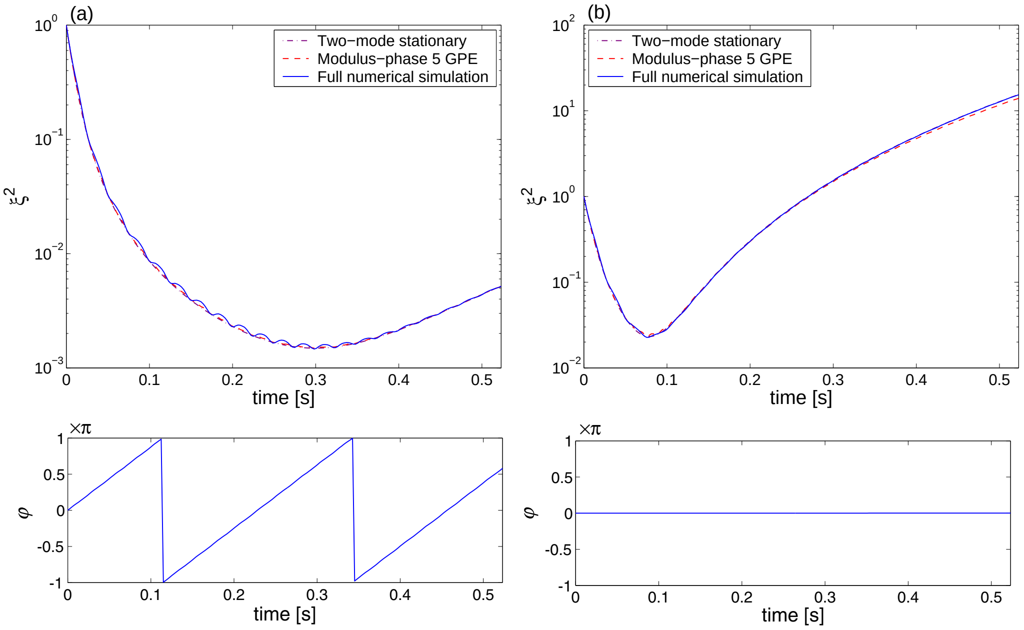

Figure 4.2: (Top) Spin squeezing as a function of time in the cases in which the spatial dynamics is weakly excited after the $\pi/2$-pulse populating a second internal state. Blue solid line: full numerical calculation with 1000 Fock states. Red dashed line: modulus-phase model. Violet dash-dotted line: stationary two-mode model using (4.41)-(4.43). (Bottom) Angle giving the direction of the mean spin projection in the equatorial plane of the Bloch sphere. Parameters: $\omega = 2\pi\times 42.6\,\text{Hz}$, (a) $\bar{N}_a = \bar{N}_b = 1\times 10^4$, (b) $\bar{N}_a = 7432$, $\bar{N}_b = 12568$. Other parameters: m=87 a.m.u., $a_{aa} = 100.44\,r_B$, $a_{bb} = 95.47\,r_B$, $a_{ab} = 88.28\,r_B$. No particle losses. r_B is the Bohr radius.

4.2.2 Breathe-together configuration

In this section we restrict to a spherically symmetric harmonic potential $U_\varepsilon = M\omega^2 r^2/2$ identical for the two internal states. For values of the inter-species scattering length such that

$$a_{ab} < a_{aa}, a_{bb} \tag{4.44}$$

and for a particular choice of the mixing angle such that the mean-field seen by the two condensates with $\bar{N}_a$ and $\bar{N}_b$ particles is the same:

$$\bar{N}_a g_{aa} + \bar{N}_b g_{ab} = \bar{N}_b g_{bb} + \bar{N}_a g_{ab} \equiv \bar{N} g\,, \tag{4.45}$$

the wave functions $\bar{\phi}_a$ and $\bar{\phi}_b$ solve the same Gross-Pitaevskii equation. In the Thomas-Fermi limit, the wave functions $\bar{\phi}_a$ and $\bar{\phi}_b$ share the same scaling solution $\bar{\phi}$ [73, 74] and “breathe-together” [70],

$$\bar{\phi}_a = \bar{\phi}_b = \bar{\phi}(\mathbf{r},t) \equiv \frac{e^{-i\eta(t)}}{\mathcal{L}^{3/2}(t)} e^{iMr^2\dot{\mathcal{L}}(t)/2\hbar\mathcal{L}(t)} \bar{\phi}_0 \left[\frac{\mathbf{r}}{\mathcal{L}(t)}\right] \tag{4.46}$$

with

$$\dot{\eta} = \frac{g}{g_{aa}} \frac{\bar{\mu}}{\mathcal{L}^3\hbar} \tag{4.47}$$

$$\frac{d^2\mathcal{L}}{dt^2} = \frac{g}{g_{aa}} \frac{\omega^2}{\mathcal{L}^4} - \omega^2\mathcal{L}\,; \tag{4.48}$$

$$\bar{\phi}_0(\mathbf{r}) = \left(\frac{15}{8\pi R_0^3}\right)^{1/2} \left[1 - \frac{r^2}{R_0^2}\right]^{1/2} \tag{4.49}$$

$\bar{\mu}$ is the chemical potential of the stationary condensate *before* the $\pi/2$-pulse, when all the N atoms are in state a, and $R_0 = \sqrt{2\bar{\mu}/m\omega^2}$ is the corresponding Thomas-Fermi radius, $\mathcal{L}(t)$ is the scaling parameter. The initial conditions for (4.48) are $\mathcal{L}(0) = 1$ and $\dot{\mathcal{L}}(0) = 0$.

Note that the scaling solution identical for the two modes a and b is valid only for $N_a = \bar{N}_a$, $N_b = \bar{N}_b$ and does not apply to all the wave functions $\phi_a(N_a, N_b)$ and $\phi_b(N_a, N_b)$ appearing in the expansion equation (4.5). Nevertheless, an advantage of choosing the mixing angle in order to satisfy the breathe-together condition (4.45), is that the mean spin has no drift velocity. In Fig.4.2 we calculate the spin squeezing (Top) and the angle φ giving the direction of the mean spin projection on the equatorial plane of the Bloch sphere (Bottom). Parameters are the same in Fig.4.2 (a) and (b) except for the mixing angle: in (a) we have $\bar{N}_a = \bar{N}_b$ while in (b) the mixing angle is chosen to satisfy (4.45). Note that φ in the latter case practically does not evolve. The maximum squeezing is worse in the breathe-together configuration than in the even-mixing case [66]. However, this conclusion does not hold when particle losses are taken into account. One of such example will be given in chapter 5.

By linearization of $\phi_a(N_a, N_b)$ and $\phi_b(N_a, N_b)$ around the breathe-together solution $\bar{\phi}_\varepsilon$ and using classical hydrodynamics, it is even possible to calculate *analytically* the parameters χ_d and χ_s relevant for the squeezing dynamics [70]. One obtains:

$$\begin{aligned}\chi_d(\mathbf{r},t) = &- \frac{1}{2\hbar}\left(\frac{2}{5}\frac{\bar{\mu}}{N}\right)\frac{g_{aa}+g_{bb}-2g_{ab}}{g_{aa}} \\ &\cdot \left\{\int_0^t \left[\frac{dt'}{\mathcal{L}^3(t')}\right] + \frac{5}{2}\frac{\mathrm{Im}\mathcal{B}(t)}{\Omega_5}\left[\left(\frac{r}{\mathcal{L}(t)R_0}\right)^2 - \frac{3}{5}\right]\right\}\end{aligned} \tag{4.50}$$

$$\chi_s(\mathbf{r},t) = \left(|C_b|^2 - |C_a|^2\right)\chi_d(\mathbf{r},t) = \chi_0(\mathbf{r},t)\,. \tag{4.51}$$

with χ_d, χ_s, and χ_0 defined in (4.25)-(4.27), and

$$\Omega_5 = \left(\frac{\bar{N}_a \bar{N}_b}{N^2} \frac{g_{aa} + g_{bb} - 2g_{ab}}{g_{aa}} \right)^{1/2} 5^{1/2}\omega \tag{4.52}$$

where $\mathcal{B}(t)$ is solution of the differential equations

$$i\dot{\mathcal{A}} = \frac{\Omega_5}{\mathcal{L}^2(t)}\mathcal{B} \tag{4.53}$$

$$i\dot{\mathcal{B}} = \frac{\Omega_5}{\mathcal{L}^3(t)}\mathcal{A} \tag{4.54}$$

to be solved together with equation (4.48), with initial conditions $\mathcal{A}(0) = \mathcal{B}(0) = 1$. In practice, when we expand the condensate wave functions around the breathe-together solution equation (4.46) as in [70], we encounter the hydrodynamics operator S [75]

$$S[\alpha] \equiv -\frac{N g_{aa}}{M} \mathrm{div}[\bar{\phi}_0^2 \,\mathbf{grad}\, \alpha]\,. \tag{4.55}$$

The deviation of the relative phase and the relative density from the breathe-together solution expand over two eigenmodes of S: A zero-energy mode which grows linearly in time and gives the dominant features of phase dynamics and squeezing (integral term in the curly brackets in Eq.(4.50)), and a breathing mode of frequency Ω_5 which is responsible for the oscillations of the squeezing parameter.

The fact that in breathe-together conditions and within the modulus-phase approximation $\chi_s = \chi_0$ is shown as follows. Evaluating (4.32) for $\varepsilon = a$, $N_a = \bar{N}_a$; $\varepsilon = b$, $N_b = \bar{N}_b$ and subtracting the two relations, one obtains

$$\frac{\partial}{\partial t} \left(\frac{\partial \bar{\theta}_a}{\partial N_b} - \frac{\partial \bar{\theta}_b}{\partial N_a} \right) = 0 \tag{4.56}$$

where we used the fact that in breathe-together conditions $|\bar{\phi}_a| = |\bar{\phi}_b|$. Equation (4.56) implies that the time derivative of $\chi_s - \chi_0$ is zero. As for $t = 0$ $\chi_s = \chi_0 = 0$, we conclude that $\chi_s = \chi_0$ at all times.

We give an example corresponding to strongly oscillating wave functions in Fig.4.3 where we compare the spin squeezing obtained from the analytical theory with a numerical simulation. In the analytical formula, the entanglement between spatial degrees of freedom and spin dynamics is apparent as χ_d in Eq. (4.50) is position dependent. The points in which the dynamical curve (dotted line) touches the stationary two mode curve (dash-dotted line) correspond to Im$\mathcal{B} = 0$ (see the bottom curve) where space and spin dynamics disentangle. We note however that the validity conditions of classical

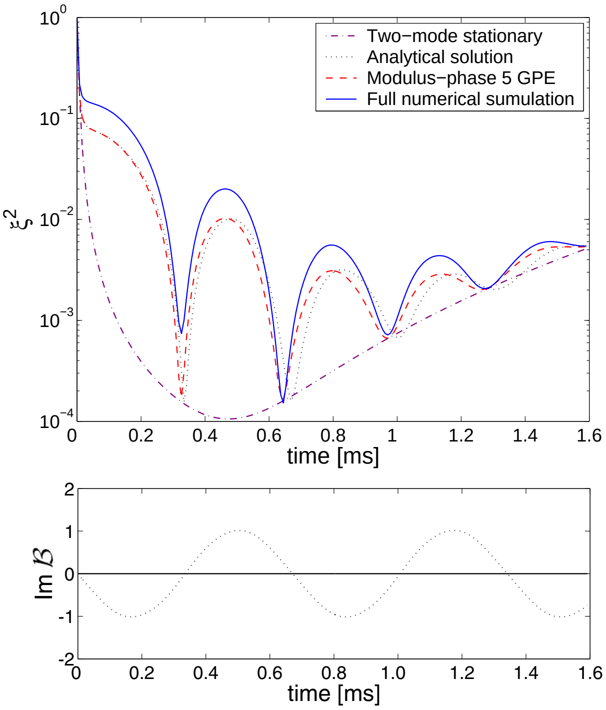

Figure 4.3: (Top) Test of the analytical formula Eq.(4.50) in the deep Thomas-Fermi regime. Spin squeezing as a function of time. Blue solid line: full numerical calculation. Red dashed line: modulus-phase approach. Black dotted line: analytical curve using equation (4.50). Violet dash-dotted line: stationary two-mode model using (4.41)-(4.43). (Bottom) Function Im$\mathcal{B}$. Spatial and spin dynamics disentangle when Im$\mathcal{B}(t) = 0$. Parameters: $\bar{N}_a = \bar{N}_b = 5 \times 10^5$, $\omega = 2\pi \times 2\,\text{kHz}$, m=87 a.m.u., $a_{aa} = a_{bb} = 0.3\,a_{ho}$,$a_{ab} = 0.24\,a_{ho}$. a_{ho} is the harmonic oscillator length: $a_{ho} = \sqrt{\hbar/M\omega}$. No particle losses.

hydrodynamics are more stringent for a mixture of condensates with rather close scattering lengths than for a single condensate [70]. We checked numerically that in order for equation (4.50) to correctly predict the frequency of the oscillations in the squeezing parameter, we have to enter deeply in the Thomas-Fermi regime.

4.3 Extracted spin squeezing

As we pointed out, the definitions Eq.(4.13)-(4.15) explicitly include the spatial overlap between the two modes. Here we give an alternative definition that can be used always, whether or not the modes overlap. To this aim, we introduce the time-dependent operators

$$\tilde{a} = \int d^3r\, \bar{\phi}_a^*(\mathbf{r},t)\hat{\psi}_a(\mathbf{r}), \tag{4.57}$$

$$\tilde{b} = \int d^3r\, \bar{\phi}_b^*(\mathbf{r},t)\hat{\psi}_b(\mathbf{r}), \tag{4.58}$$

where $\bar{\phi}_\varepsilon(\mathbf{r},t)$ is the solution of Gross-Pitaevskii Eq. (4.10) for mode ε with $\bar{N}_a$, $\bar{N}_b$ particles. We then introduce the spin operators:

$$\tilde{S}_x = \frac{1}{2}(\tilde{b}^\dagger\tilde{a} + \tilde{a}^\dagger\tilde{b}), \tag{4.59}$$

$$\tilde{S}_y = \frac{i}{2}(\tilde{b}^\dagger\tilde{a} - \tilde{a}^\dagger\tilde{b}), \tag{4.60}$$

$$\tilde{S}_z = \frac{1}{2}(\tilde{a}^\dagger\tilde{a} - \tilde{b}^\dagger\tilde{b}). \tag{4.61}$$

We call "extracted" spin squeezing the squeezing obtained from the spin operators defined in Eq.(4.59)-(4.61). Within this definition, we still take into account entanglement between external motion and spin dynamics, but we give up the information about the overlap between the two modes. By using the instantaneous modes (4.57)-(4.58) and within the modulus-phase approach (4.24), the quantum averages useful to calculate spin squeezing are expressed in terms of the functions:

$$\chi_d^{\mathrm{ex}}(\mathbf{r},\mathbf{r}') = \frac{1}{2}(\partial_{N_a} - \partial_{N_b})[\theta_a(\mathbf{r}) - \theta_b(\mathbf{r}')](\bar{N}_a,\bar{N}_b) \tag{4.62}$$

$$\chi_s^{\mathrm{ex}}(\mathbf{r},\mathbf{r}') = \frac{1}{2}(\partial_{N_a} + \partial_{N_b})[\theta_a(\mathbf{r}) - \theta_b(\mathbf{r}')](\bar{N}_a,\bar{N}_b) \tag{4.63}$$

$$\chi_0^{\mathrm{ex}}(\mathbf{r},\mathbf{r}') = \frac{1}{2}(\partial_{N_a} - \partial_{N_b})[\theta_a(\mathbf{r}) + \theta_b(\mathbf{r}')](\bar{N}_a,\bar{N}_b)\,. \tag{4.64}$$

By using the relation

$$\begin{aligned}\int d^3r|\bar{\phi}_\varepsilon|^2 \exp\left[i(\partial_{N_a} - \partial_{N_b})\theta_\varepsilon(\bar{N}_a,\bar{N}_b)\right] \\ \simeq \exp\left[i\int d^3r|\bar{\phi}_\varepsilon|^2(\partial_{N_a} - \partial_{N_b})\theta_\varepsilon(\bar{N}_a,\bar{N}_b)\right]\,.\end{aligned} \tag{4.65}$$

we obtain:

$$\begin{aligned}\langle\tilde{b}^\dagger\tilde{a}\rangle = NC_b^*C_a \int d^3r_1d^3r_2|\bar{\phi}_b(\mathbf{r}_1)|^2|\bar{\phi}_a(\mathbf{r}_2)|^2 \left[|C_a|^2e^{i\chi_d^{\mathrm{ex}}(\mathbf{r}_2,\mathbf{r}_1)}\right. \\ \left. + |C_b|^2e^{-i\chi_d^{\mathrm{ex}}(\mathbf{r}_2,\mathbf{r}_1)}\right]^{N-1} \exp\left[-i\bar{N}(|C_a|^2 - |C_b|^2)\chi_d^{\mathrm{ex}}(\mathbf{r}_2,\mathbf{r}_1)\right. \\ \left. +i(N-\bar{N})\chi_s^{\mathrm{ex}}(\mathbf{r}_2,\mathbf{r}_1) + i\chi_0^{\mathrm{ex}}(\mathbf{r}_2,\mathbf{r}_1)\right]\,,\end{aligned} \tag{4.66}$$

$$\langle \tilde{b}^\dagger \tilde{a}^\dagger \tilde{a} \tilde{b} \rangle = N(N-1)|C_a|^2 |C_b|^2 \,, \tag{4.67}$$

$$\begin{aligned}
\langle \tilde{b}^\dagger \tilde{b}^\dagger \tilde{a} \tilde{a} \rangle &= N(N-1) C_b^{*2} C_a^2 \int d^3r_1 d^3r_2 d^3r_3 d^3r_4 |\bar{\phi}_b(\mathbf{r}_1)|^2 |\bar{\phi}_b(\mathbf{r}_2)|^2 |\bar{\phi}_a(\mathbf{r}_3)|^2 | \\
&\cdot \bar{\phi}_a(\mathbf{r}_4)|^2 \left\{ |C_a|^2 e^{i[\chi_d^{\text{ex}}(\mathbf{r}_4,\mathbf{r}_2)+\chi_d^{\text{ex}}(\mathbf{r}_3,\mathbf{r}_1)]} + |C_b|^2 e^{-i[\chi_d^{\text{ex}}(\mathbf{r}_4,\mathbf{r}_2)+\chi_d^{\text{ex}}(\mathbf{r}_3,\mathbf{r}_1)]} \right\}^{N-2} \\
&\cdot \exp\left\{ -i\bar{N}(|C_a|^2 - |C_b|^2) \left[\chi_d^{\text{ex}}(\mathbf{r}_4,\mathbf{r}_2) + \chi_d^{\text{ex}}(\mathbf{r}_3,\mathbf{r}_1) \right] \right. \\
&\left. + i(N-\bar{N}) \left[\chi_s^{\text{ex}}(\mathbf{r}_4,\mathbf{r}_2) + \chi_s^{\text{ex}}(\mathbf{r}_3,\mathbf{r}_1) \right] + 2i \left[\chi_0^{\text{ex}}(\mathbf{r}_4,\mathbf{r}_2) + \chi_0^{\text{ex}}(\mathbf{r}_3,\mathbf{r}_1) \right] \right\} \\
&\cdot \exp\left\{ -i \int d^3r_5 \left(|\bar{\phi}_a(\mathbf{r}_5)|^2 \left[\chi_0^{\text{ex}}(\mathbf{r}_5,\mathbf{r}_5) + \chi_d^{\text{ex}}(\mathbf{r}_5,\mathbf{r}_5) \right] \right. \right. \\
&\left. \left. + |\bar{\phi}_b(\mathbf{r}_5)|^2 \left[\chi_0^{\text{ex}}(\mathbf{r}_5,\mathbf{r}_5) - \chi_d^{\text{ex}}(\mathbf{r}_5,\mathbf{r}_5) \right] \right) \right\} \,,
\end{aligned} \tag{4.68}$$

$$\begin{aligned}
\langle \tilde{b}^\dagger \tilde{b}^\dagger \tilde{b} \tilde{a} \rangle &= N(N-1) C_b^* C_a |C_b|^2 \int d^3r_1 d^3r_2 |\bar{\phi}_b(\mathbf{r}_1)|^2 |\bar{\phi}_a(\mathbf{r}_2)|^2 \\
&\cdot \left[|C_a|^2 e^{i\chi_d^{\text{ex}}(\mathbf{r}_2,\mathbf{r}_1)} + |C_b|^2 e^{-i\chi_d^{\text{ex}}(\mathbf{r}_2,\mathbf{r}_1)} \right]^{N-2} \exp\left\{ -i \left[\bar{N}(|C_a|^2 - |C_b|^2) \right. \right. \\
&\left. \left. + 1 \right] \chi_d^{\text{ex}}(\mathbf{r}_2,\mathbf{r}_1) + i(N-\bar{N}) \chi_s^{\text{ex}}(\mathbf{r}_2,\mathbf{r}_1) + i\chi_0^{\text{ex}}(\mathbf{r}_2,\mathbf{r}_1) \right\} \,,
\end{aligned} \tag{4.69}$$

$$\begin{aligned}
\langle \tilde{a}^\dagger \tilde{a}^\dagger \tilde{a} \tilde{b} \rangle &= N(N-1) C_a^* C_b |C_a|^2 \int d^3r_1 d^3r_2 |\bar{\phi}_a(\mathbf{r}_1)|^2 |\bar{\phi}_b(\mathbf{r}_2)|^2 \\
&\cdot \left[|C_b|^2 e^{i\chi_d^{\text{ex}}(\mathbf{r}_1,\mathbf{r}_2)} + |C_a|^2 e^{-i\chi_d^{\text{ex}}(\mathbf{r}_1,\mathbf{r}_2)} \right]^{N-2} \exp\left\{ i \left[\bar{N}(|C_a|^2 - |C_b|^2) \right. \right. \\
&\left. \left. - 1 \right] \chi_d^{\text{ex}}(\mathbf{r}_1,\mathbf{r}_2) - i(N-\bar{N}) \chi_s^{\text{ex}}(\mathbf{r}_1,\mathbf{r}_2) - i\chi_0^{\text{ex}}(\mathbf{r}_1,\mathbf{r}_2) \right\} \,.
\end{aligned} \tag{4.70}$$

Comparing the above expressions with Eq.(2.48)-(2.51), one realizes that in the stationary case, where χ_d, χ_s and χ_0 are space independent, the extracted spin squeezing dynamical model reduces again to a two-mode model that we study in detail in the chapter 3. We will use this extracted spin squeezing in the following chapters.

Chapter 5

Experiment proposals for spin squeezing

In this chapter, we apply our treatment to cases of practical interest. In section 5.1, we first consider a bimodal ^{87}Rb condensate. Rb is one of the most common atoms in BEC experiments and it is a good candidate for atomic clocks using trapped atoms on a chip [38]. Restricting to states which are equally affected by a magnetic field to first order, the most common choices are $|F = 1, m_F = -1\rangle$ and $|F = 2, m_F = 1\rangle$ which can be magnetically trapped, or $|F = 1, m_F = 1\rangle$ and $|F = 2, m_F = -1\rangle$ that must be trapped optically but for which there exists a low-field Feshbach resonance which can be used to reduce the inter species scattering length [67, 68]. Indeed a particular feature of these Rb states is that the three s-wave scattering lengths characterizing interactions between $a-a$, $b-b$ and $a-b$ atoms are very close to each other. A consequence is that the squeezing dynamics is very slow when the two condensates overlap. The inter-species Feshbach resonance [67] can be used to overcome this problem and speed up the dynamics [68, 41].

In schemes involving the $|F = 2, m_F = \pm 1\rangle$ of Rb, the main limit to the maximum squeezing achievable is set by the large two-body losses rate in these states. As a second case of experimental interest we then consider Na atoms in the $|F = 1, m_F = \pm 1\rangle$ states [23]. Although theses states have opposite shifts in a magnetic field, they present the advantage of negligible two-body losses. Using our analytical optimization procedure, we calculate the maximum squeezing achievable in these systems including the effect of spatial dynamics and particle losses.

In section 5.2, we examine a different scenario for Rb condensates in which, instead of changing the scattering length, one would spatially separate the two condensates after the mixing $\pi/2$-pulse and hold them separately during a well chosen squeezing time, so that the squeezing dynamics acts

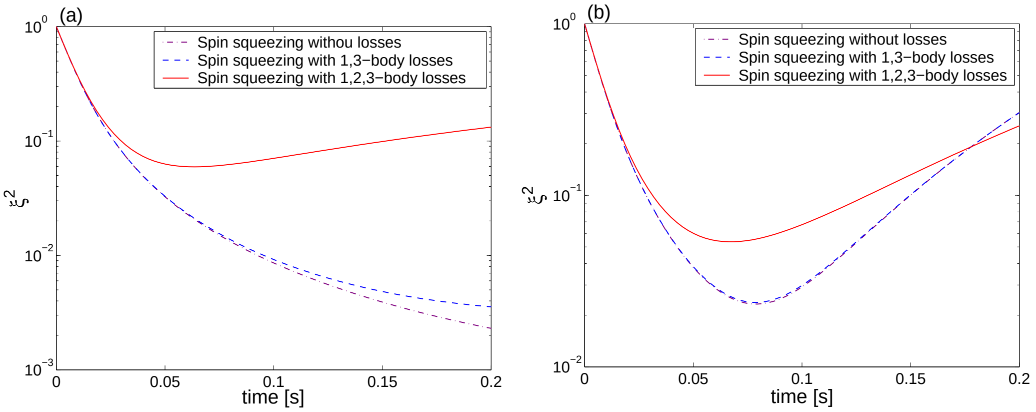

Figure 5.1: Spin squeezing with and without losses in a bimodal Rb condensate from the stationary two-mode model. A Feshbach resonance is used to reduce the inter-species scattering length by 10 %. Violet dash-dotted line: without losses. Blue dashed line: with one and three-body losses. Red solid line: with one, two and three-body losses. (a) For a $50-50$ mixing of the two states: $\bar{N}_a = \bar{N}_b = 10^4$, $\chi_d^{\rm 2m} = 5.367\times10^{-3}{\rm s}^{-1}$, $\chi_s^{\rm 2m} = 5.412\times10^{-4}\,{\rm s}^{-1}$. (b) In breathe-together conditions: $\bar{N}_a = 7432$, $\bar{N}_b = 12568$, $\chi_d^{\rm 2m} = 5.392\times10^{-3}\,{\rm s}^{-1}$, $\chi_s^{\rm 2m} = 1.386\times10^{-3}\,{\rm s}^{-1}$. Other parameters: $\omega = 2\pi\times 42.6\,{\rm Hz}$, m=87 a.m.u., $a_{aa} = 100.44\,r_B$, $a_{bb} = 95.47\,r_B$, $a_{ab} = 88.28\,r_B$, r_B is the Bohr radius. Particle losses: $K_1^{(a)} = K_1^{(b)} = 0.01\,{\rm s}^{-1}$, $K_2^{(a)} = 0$, $K_2^{(b)} = 119\times10^{-21}\,{\rm m}^3{\rm s}^{-1}$ [64], $K_2^{(ab)} = 78\times10^{-21}\,{\rm m}^3{\rm s}^{-1}$ [76], $K_3^{(a)} = 6\times10^{-42}\,{\rm m}^6{\rm s}^{-1}$ [65].

only when the clouds are spatially separated and it freezes out when the two clouds are put back together. The control of the atomic nonlinearity is an important feature of the schemes using Rb that we will consider in the next chapter. Very recently, both schemes we have studied for Rb atoms were implemented in experiment, using Feschbach resonance in [41] and using state-dependent potentials on an atom chip in [40]. The main results of this chapter are published in [36].

5.1 Overlapping condensates Rb or Na

We first consider a bimodal ^{87}Rb condensate in $|F=1, m_F=1\rangle$ and $|F=2, m_F=-1\rangle$ states where the scattering length a_{ab} is lowered by about 10% with respect to its bare value using a Feshbach resonance [67, 68].

In Fig.5.1 (a) and (b) we compare a situation in which the initial condensate is split evenly in the a and b components to a situation in which the mixing is chosen in order to satisfy the “breathe-together” conditions (4.45).

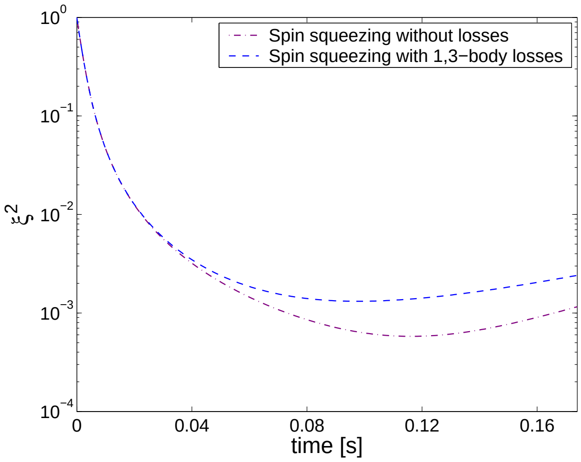

Figure 5.2: Spin squeezing with and without losses in a bimodal Na condensate from the stationary two-mode model. Violet dash-dotted line: without losses. Blue dashed line: with one and three-body losses. Optimized parameters: $\bar{N}_a = \bar{N}_b = 4 \times 10^4$ $\omega = 2\pi \times 183\,\text{Hz}$, m=23 a.m.u., $a_{aa} = a_{bb} = 51.89\,r_B$, $a_{ab} = 48.25\,r_B$, r_B is the Bohr radius. $\chi_d^{2\text{m}} = 5.517 \times 10^{-3}\,\text{s}^{-1}$, $\chi_s^{2\text{m}} = 0$. Particle losses: $K_1^{(a)} = K_1^{(b)} = 0.01\,\text{s}^{-1}$, $K_2^{(a)} = K_2^{(b)} = 0$, $K_3^{(a)} = K_3^{(b)} = 2 \times 10^{-42}\,\text{m}^6\text{s}^{-1}$ [77].

For the considered parameters, which are the same as Fig.4.2 (a) and (b), the spatial dynamics is not important and the two-mode model is a good approximation at all times. The squeezing in presence of losses is calculated using our general results of chapter 3 for asymmetric condensates. Although without losses the even splitting is more favorable, with one, two, three-body losses, results for the best squeezing are comparable $\xi^2 \simeq 6 \times 10^{-2}$. In the same figure 5.1, we also show a curve obtained for one and three-body losses only (dashed-line). It is clear that for the considered Rb states the dominant contribution for decoherence comes from the two-body losses in the $F = 2$ state severely limiting the maximum amount of obtainable squeezing. We have checked that the crossed ab losses have limited contribution in this case, as expected.

By using two states in the lower hyperfine manifold, one can greatly reduce two-body losses. A possible example is of using Na atoms in the $|F = 1, m_F = \pm 1\rangle$ states [23]. In Fig.5.2 we calculate the best obtainable squeezing with these two states. Parameters are chosen according to our optimization procedure of section 3.2. A large amount of squeezing $\xi^2 = 1.9 \times 10^{-3}$ can be reached at the best squeezing time. However, here the inter-species scattering length a_{ab} is not changed. As a result, the nonlinearity introduced by interactions will not be stopped after the best squeezing time is reached.

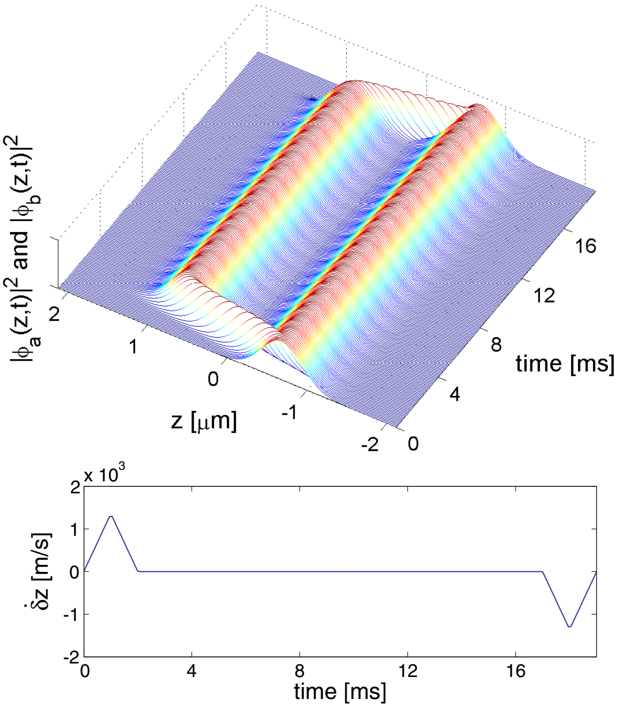

Figure 5.3: (Top) $|\phi_a(z,t)|^2$ and $|\phi_b(z,t)|^2$ in arbitrary units as the clouds are separated and put back together after an interaction time of about 15 ms. The harmonic potential for the a-component does not move, while that for the b-component is shifted vertically with a speed $\dot{\delta z}$. The distance between the two trap centers when they are separated is $\delta z = 4\sqrt{\hbar/M\omega_z}$. (Bottom) Variation in time of $\dot{\delta z}$. Parameters: $\bar{N}_a = \bar{N}_b = 5 \times 10^4$, $\omega_{x,y} = 2\pi \times 2.31\,\mathrm{Hz}$, $\omega_z = 2\pi \times 1\,\mathrm{kHz}$, m=87 a.m.u., $a_{aa} = 100.44\,r_B$, $a_{bb} = 95.47\,r_B$, $a_{ab} = 98.09\,r_B$, r_B is the Bohr radius. No particle losses.

Using our full numerical and our approximated dynamical approaches, (not shown in the figure) we checked that the two-mode model is an excellent approximation for these parameters.

5.2 Dynamically separated Rb BEC

In this subsection we consider a bimodal Rb condensate in $|F = 1, m_F = -1\rangle$ and $|F = 2, m_F = 1\rangle$ states. Rather than using a Feshbach resonance to change g_{ab}, we consider the possibility of suddenly separating the two clouds right after the mixing $\pi/2$-pulse using state-dependent potentials [78, 79], and recombining them after a well chosen interaction time. A related scheme

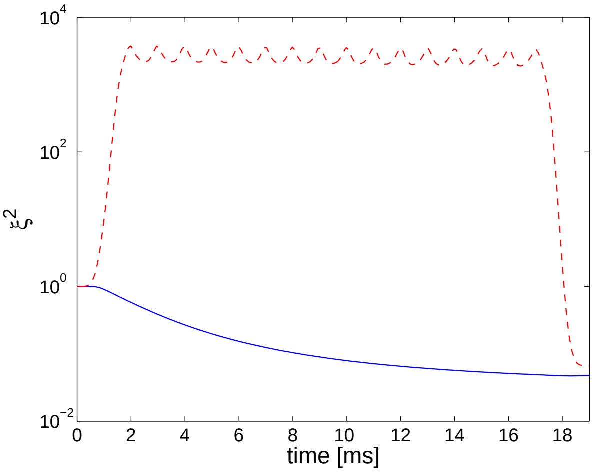

Figure 5.4: Spin squeezing as the two Rb condensates are separated and put back together after an interaction time of about 15 ms. Red dashed line: Spin squeezing obtained from the definitions (4.13)-(4.15) of the spin operators explicitly including the overlap between the clouds. Blue solid line: extracted spin squeezing based of the "instantaneous modes" (4.57)-(4.58). Parameters as in Fig.5.3.

using Bragg pulses in the frame of atom interferometry was proposed in [80]. We consider disc-shaped identical traps for the two states a and b with $\omega_z > \omega_{x,y} \equiv \omega_\perp$, that can be displaced independently along the z axes. In order to minimize center-of-mass excitation of the cloud, we use a triangular ramp for the displacement velocity, as shown in Fig.5.3 (Bottom), with total move-out time $2\tau = 4\pi/\omega_z$ [81]. In Fig.5.3 (Top) we show the z-dependence of densities of the clouds, integrated in the perpendicular xy plane, as the clouds are separated and put back together after a given interaction time.

We use our dynamical modulus-phase model in 3 dimensions to calculate the spin squeezing in this scheme. As the spatial overlap between the two clouds reduces a lot as they are separated, in Fig.5.4 we calculate both the spin squeezing obtained from the definitions (4.13)-(4.15) of spin operators (dashed line), and the "extracted spin squeezing" introduced in Section 4.3 based on the "instantaneous modes" (4.57)-(4.58) (solid line). The oscillations in the dashed line are due to tiny residual center of mass oscillations of the clouds that change periodically the small overlap between the two modes. They are absent in the extracted spin squeezing curve (solid line) as they do not affect the spin dynamics. When the clouds are put back together and the overlap between the modes is large again, the spin squeezing and the extracted spin squeezing curves give close results (not identical as the overlap of the two clouds is not precisely one).

In Fig.5.5 (a) we compare the extracted spin squeezing curve of Fig.5.4 (solid line) with a two-mode stationary calculation (dash-dotted line) assuming stationary condensates in separated wells. We notice that the squeezing progresses much more slowly in the dynamical case. Indeed when we separate the clouds, the mean-field changes suddenly for each component exciting a breathing mode whose amplitude and frequency is different for each of the Fock states involved. In the quasi 2D configuration considered here, the breathing of the wave functions is well described by a scaling solution in 2D for each condensate separately [73, 74] adapted to the case in which the trap frequency is not changed, but the mean-field is changed suddenly after separation of the two internal states:

$$\phi_\varepsilon(\mathbf{r}_\perp,t)=\frac{e^{-i\eta_\varepsilon(t)}}{\mathcal{L}_\varepsilon(t)}\exp\left[\frac{imr_\perp^2\dot{\mathcal{L}}_\varepsilon(t)}{2\hbar\,\mathcal{L}_\varepsilon(t)}\right]\phi_0\left(\frac{\mathbf{r}_\perp}{\mathcal{L}_\varepsilon(t)}\right) \tag{5.1}$$

with

$$\dot{\eta}_\varepsilon=\frac{\tilde{g}_{\varepsilon\varepsilon}}{\tilde{g}_{aa}}\frac{\bar{\mu}}{\mathcal{L}_\varepsilon^2\hbar} \tag{5.2}$$

$$\frac{d^2\mathcal{L}_\varepsilon}{dt^2}=\frac{N_\varepsilon}{N}\frac{\tilde{g}_{\varepsilon\varepsilon}}{\tilde{g}_{aa}}\frac{\omega_\perp^2}{\mathcal{L}_\varepsilon^3}-\omega_\perp^2\mathcal{L}_\varepsilon\ ; \tag{5.3}$$

$$\phi_0(\mathbf{r}_\perp)=\left(\frac{2}{\pi R_0^2}\right)^{1/2}\left[1-\frac{r_\perp^2}{R_0^2}\right]^{1/2}. \tag{5.4}$$

In Eqs(5.2)-(5.4), $\bar{\mu}$ is the chemical potential of the stationary condensate *before* the $\pi/2$ pulse, when all the N atoms are in state a, $R_0=\sqrt{2\bar{\mu}/m\omega_\perp^2}$ is the corresponding Thomas-Fermi radius, and $\tilde{g}_{\varepsilon\varepsilon}$ is a reduced coupling constant to describe the interaction between two atoms in the ε condensate in quasi 2D system,

$$\tilde{g}_{\varepsilon\varepsilon}=\frac{4\pi\hbar^2a_{\varepsilon\varepsilon}}{M}\sqrt{\frac{M\omega_z}{2\pi\hbar}} \tag{5.5}$$

where we assume that the condensate wave functions in the confined direction are Gaussian, and $a_{\varepsilon\varepsilon}$ is the 3D scattering length. The initial conditions for (5.3) are $\mathcal{L}_\varepsilon(0)=1$ and $\dot{\mathcal{L}}_\varepsilon(0)=0$.

We can use (5.1) to calculate the squeezing (dotted curve) and we note that it reproduces well the spin squeezing curve obtained integrating 5 Gross-Pitaevskii equations in 3D (full line). As we studied in detail in Section 4.2.2, oscillations of the wave functions cause oscillations of the squeezing parameter due to entanglement between spatial and spin dynamics. Indeed what we see in the extracted spin squeezing curve of Fig.5.5 (a) is the beginning of a slow oscillation for the squeezing parameter. In Fig.5.5 (b) we show the

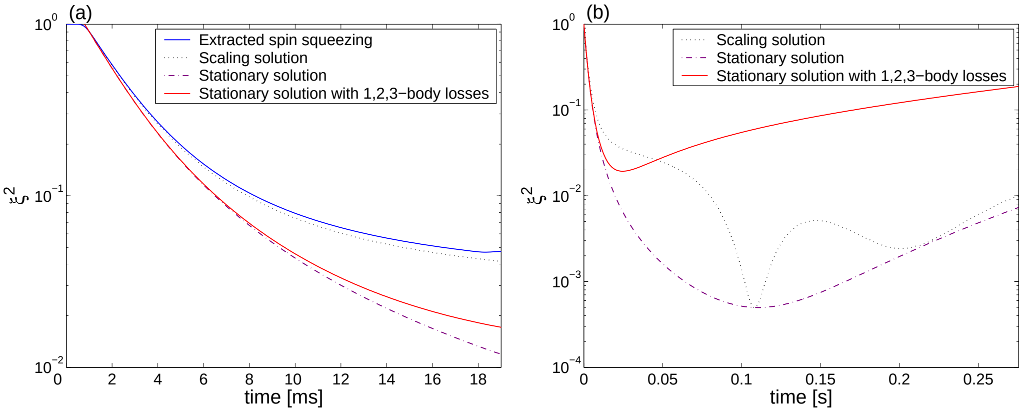

Figure 5.5: Spin squeezing as a function of time. (a) Comparison between a dynamical calculation and a stationary calculation. Blue solid line: extracted spin squeezing in 3D. Black doted line: 2D analytical scaling solution based on (5.3). Violet dash-dotted line: stationary calculation in 3D without losses. Red solid line: stationary calculation in 3D with losses. Spin squeezing progresses more slowly in the dynamical calculation than in the stationary calculation. (b) Long time behavior. Black doted line: scaling solution. Violet dash-dotted line: stationary calculation without losses. Red solid line: stationary calculation with losses. Parameters: $\chi_d^{2\text{m}} = 5.003 \times 10^{-3}\,\text{s}^{-1}$, $\chi_s^{2\text{m}} = 1.342 \times 10^{-4}\,\text{s}^{-1}$, $K_a^{(1)} = K_b^{(1)} = 0.01\,\text{s}^{-1}$, $K_a^{(2)} = 0$, $K_b^{(2)} = 119 \times 10^{-21}\,\text{m}^3\text{s}^{-1}$ [64], $K_a^{(3)} = 6 \times 10^{-42}\text{m}^6\,\text{s}^{-1}$ [65]. The other parameters are as in Fig.5.3.

long time behavior. There are indeed times at which the spatial and spin dynamics disentangle, and the dynamical curve and the steady state curve touch (see Sect. 4.2.2). Unfortunately these times are not accessible here in presence of losses (in particular the high two-body losses in the higher hyperfine state). Notice that in the first 15 ms of evolution considered in Fig.5.4 and Fig.5.5 (a) the effect of losses is small and the main limitation at short times is provided by the spatial dynamics. We checked that similar results can be obtained with a different geometry where we prepare the condensate in a cigar-shape trap and separate them along the longitudinal direction.

For a lower number of atoms, the sudden change in the mean-field and the consequent oscillations of the squeezing parameter are reduced. In Fig.5.6 we show the spin squeezing obtained by suddenly separating two BEC of Rb atoms in $|F = 1, m_F = -1\rangle$ and $|F = 2, m_F = 1\rangle$ states with 1000 atoms in each component. The dotted line is a dynamical calculation using the quasi 2D scaling solution (5.3) (and no losses), while the dash-dotted line and the solid line are stationary calculations without and with losses respectively. Note that around $t = 0.02$s, where the dynamical curve and the stationary

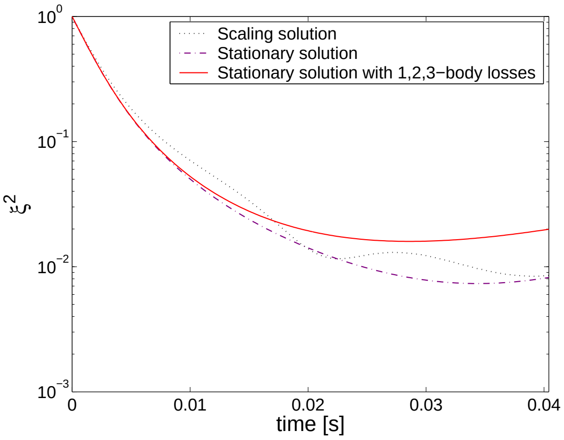

Figure 5.6: Spin squeezing as a function of time in two small Rb condensates. Black doted line: scaling solution based on (5.3). Violet dash-dotted line: stationary calculation without losses. Red solid line: stationary calculation with losses. Parameters: $K_a^{(1)} = K_b^{(1)} = 0.01\,\mathrm{s}^{-1}$, $K_a^{(2)} = 0$, $K_b^{(2)} = 119 \times 10^{-21}\,\mathrm{m}^3\mathrm{s}^{-1}$ [64], $K_a^{(3)} = 6 \times 10^{-42}\,\mathrm{m}^6\mathrm{s}^{-1}$ [65]. The other parameters: $\bar{N}_a = \bar{N}_b = 10^3$, $\omega_{x,y} = 2\pi \times 11.82\,\mathrm{Hz}$, $\omega_z = 2\pi \times 2\,\mathrm{kHz}$, m=87 a.m.u., $a_{aa} = 100.44\,r_B$, $a_{bb} = 95.47\,r_B$, $a_{ab} = 98.09\,r_B$, r_B is the Bohr radius. $\chi_d^{2\mathrm{m}} = 0.213\mathrm{s}^{-1}$, $\chi_s^{2\mathrm{m}} = 2.763 \times 10^{-3}\,\mathrm{s}^{-1}$.

curve touch, a squeezing of about $\xi^2 \sim 2 \times 10^{-2}$ could be reached despite the high losses in the $F = 2$ state.

Chapter 6

Spin squeezing on atom chip: Munich experiment

In chapter 5, we considered two schemes to realize spin squeezing in Bose-Einstein condensate with Rb atoms. Recently both schemes were successfully implemented in experiment, using a Feshbach resonance in an optical trap in [41] and using state-dependent potentials on an atom chip in [40]. We participated in the latter achievement realized in the group of P. Treutlein in Munich, giving the theoretical support.

In the experiment, the nonlinearity is adjusted by controlling the overlap between the condensates wave functions, as it is proposed in section 5.2. Initially, each atom is put in a superposition of two internal states $|a\rangle$ and $|b\rangle$. The nonlinearity furnished by interactions is "switched-on" after the state preparation, driving the factorized state to evolve into a spin squeezed state. Once the spin squeezed state is achieved, the nonlinearity can be "switched-off".

We expose here the theoretical part of the work, giving the physical explanation of the observed squeezing signals. This squeezing scheme could be applied in chip based atomic clocks experiments such as the one presently going on in Syrte in the observatoire de Paris. Other remarkable results in the field of spin squeezing on similar systems have been obtained, using a quantum coherent feedback mechanism in a cavity [54].

6.1 State preparation and coherent manipulation

The states used in the experiment are the ground state hyperfine levels $|a\rangle \equiv |F=1, m_F=-1\rangle$ and $|b\rangle \equiv |F=2, m_F=1\rangle$ of ^{87}Rb, as shown in Fig.6.1

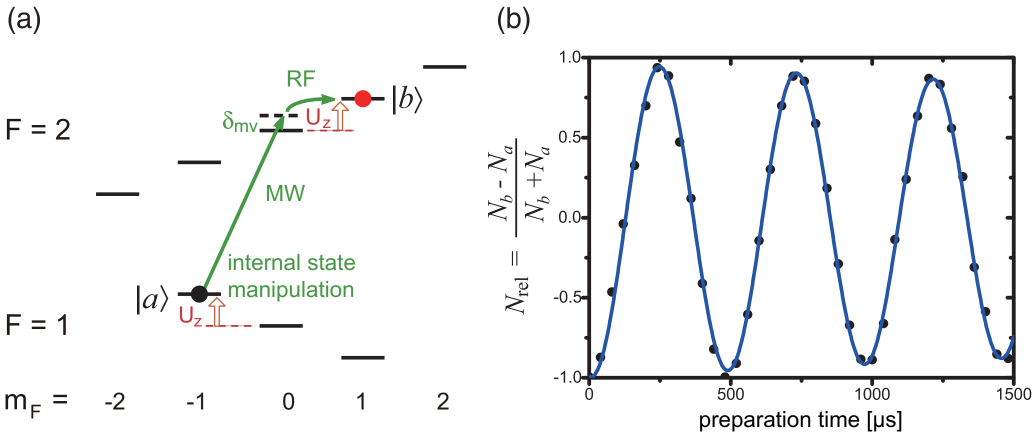

Figure 6.1: (a) Hyperfine structure of the ^{87}Rb ground state. The states $|a\rangle$ and $|b\rangle$ experience nearly identical Zeeman energy shifts U_z. For internal state manipulation of the atoms, the two-photon transition $|a\rangle \to |b\rangle$ is resonantly coupled, with detuning δ_{mw} from the intermediate state $|F = 2, m_F = 0\rangle$ (green lines). (b) Experiment: resonant Rabi oscillations of the relative atom number $N_{\mathrm{rel}} = (N_b - N_a)/(N_b + N_a)$ recorded by varying the duration of the state preparation pulse. The efficiency of a π-pulse is $(96 \pm 1)\,\%$. The decay with a time constant of 15 ms is due to gradients in Ω near the structured metallic chip surface which imposes boundary conditions on the electromagnetic field.

(a), which are also employed in chip-based atomic clocks with magnetically trapped atoms [38, 39]. Both states are magnetically trappable, have nearly identical magnetic moments which results in the same Zeeman energy shifts U_z (see Fig.6.1 (a)), and thus possess excellent coherence properties.

The initial phase state is created by applying a $\pi/2$-pulse to the single condensate prepared in state $|a\rangle$, as described in chapter 4. On the Bloch sphere it is equivalent to rotate the state from the poles to the equator around $-y$ axis, as shown in Fig.6.2. For a more general pulse of duration τ, the corresponding unitary transformation is

$$U = e^{i\Omega\tau S_y}, \tag{6.1}$$

where S_j $(j = x, y, z)$ are the spin operators defined in (2.28)-(2.30). After the unitary transformation, one has

$$\langle S_z(\tau)\rangle = \sin(\Omega\tau)\langle S_x(0)\rangle + \cos(\Omega\tau)\langle S_z(0)\rangle\,, \tag{6.2}$$

$$\langle S_x(\tau)\rangle = \cos(\Omega\tau)\langle S_x(0)\rangle - \sin(\Omega\tau)\langle S_z(0)\rangle\,. \tag{6.3}$$

When $\Omega\tau = \pi/2$ all the spins are aligned along axis-x.

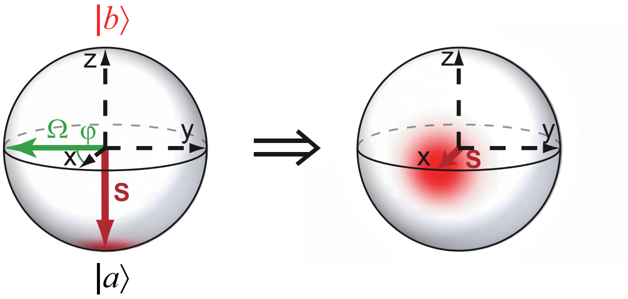

Figure 6.2: Evolution of the BEC internal state on the Bloch sphere. Starting with all atoms in $|a\rangle$, a $\pi/2$-pulse prepares a coherent spin state with mean spin $\langle \mathbf{S} \rangle$ along x and isotropic quantum noise in the yz-plane (fuzzy red circle).

In the experiment, this operation is applied by coherently driving the two-photon transition $|a\rangle \to |b\rangle$ with radio frequency and microwave radiation (green lines in Fig.6.1 (a)). This two-photon drive is turned on only for internal-state manipulation. The microwave is blue detuned with $\delta_{mw} = 2\pi \times 360\,\mathrm{kHz}$ to the $|F = 2, m_F = 0\rangle$ state, resulting in a two-photon Rabi frequency of $\Omega = 2\pi \times 2.1\,\mathrm{kHz}$. Fig.6.1 (b) shows the resulting Rabi oscillations for a detuning $\delta = 0$ from two-photon resonance. The efficiency of a π-pulse is $(96 \pm 1)\,\%$. The preparation time for the initial state $\tau = 120\,\mu\mathrm{s}$, is therefore much shorter than the spin dynamics and spatial dynamics timescales. So the external motion of the atoms does not change during the pulse. This justifies the initial state Eq.(4.4) at $t = 0$, where we assume that the two components have the same external wave functions.

6.2 Tunable nonlinearity

As described in previous sections, the three s-wave scattering lengths for the states $|a\rangle$ and $|b\rangle$ are very close, $a_{aa} : a_{ab} : a_{bb} = 100.4 : 97.7 : 95.0$ [64]. If the two components of the condensate overlap spatially, the nonlinear term characterizing the speed of squeezing χ_d is very small as an almost complete compensation occurs in Eq.(2.25) of the two-mode model,

$$\chi_d^{2\mathrm{m}} = \frac{1}{2\hbar} \left(\partial_{N_a}\mu_a + \partial_{N_b}\mu_b - \partial_{N_b}\mu_a - \partial_{N_a}\mu_b \right)_{\bar{N}_a, \bar{N}_b} \simeq 0 \tag{6.4}$$

the squeezing dynamics is very slow in this case. To overcome the problem, we can separate the two components spatially, making the crossed terms $\partial_{N_a}\mu_b$ and $\partial_{N_b}\mu_a$ zero and thus $\chi_d^{2\mathrm{m}} > 0$. The squeezing dynamics only takes place when the two components are separated. This is a new and versatile

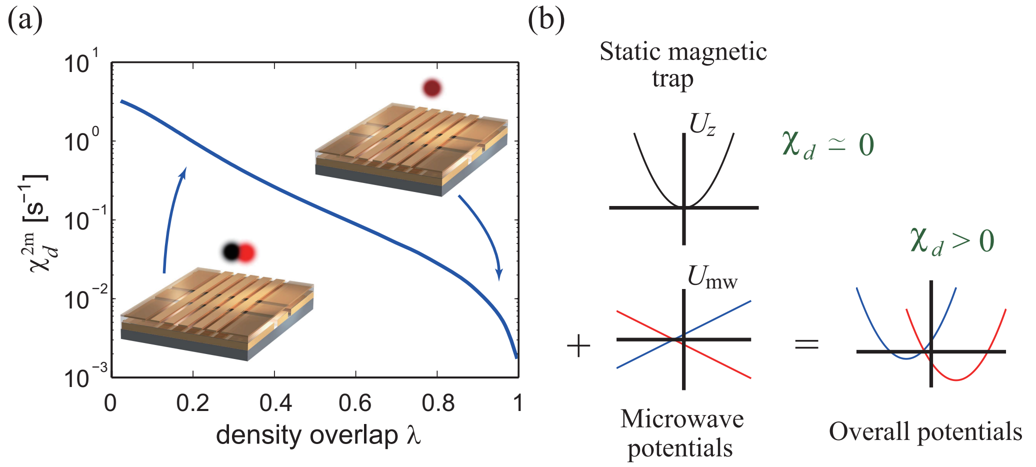

Figure 6.3: (a) Control of the nonlinearity χ_d on the atom chip. χ_d depends on the difference of intra- and inter-state atomic interactions. Its dependence on the normalized density overlap λ of the two BEC components is shown, calculated from stationary mode functions in potentials of increasing separation. The total number of atoms $N = 1250$. The trap frequencies: $\nu_x = 109\,\mathrm{Hz}$, $\nu_\perp = 500\,\mathrm{Hz}$. The trapping distance between the trap centers going from 0 to 4.0 μm. (b) Illustration of the state dependent potentials. Without microwave, the two components see the same static magnetic trap U_z, therefore χ_d is very small. The microwave induces an internal state dependent energy level shifts U_{mw} for the two states (blue and red correspondingly). Consequently the overall potentials seen by the two components are different, and χ_d is enlarged.

technique for tuning of interactions in a BEC that also works in magnetic traps and for atomic state pairs where no convenient Feshbach resonance exists. In Fig.6.3 (a) we show the parameter $\chi_d^{2\mathrm{m}}$ defined in (6.4) as a function of the normalized density overlap

$$\lambda = \frac{\int d^3r |\phi_a(\mathbf{r})|^2 |\phi_b(\mathbf{r})|^2}{\sqrt{\int d^3r |\phi_a(\mathbf{r})|^4 \int d^3r |\phi_b(\mathbf{r})|^4}} \tag{6.5}$$

calculated from the stationary mode functions (2.18) in traps of increasing separation from 0 to 4.0 μm. Note that $\chi_d^{2\mathrm{m}}$ can be tuned over three orders of magnitude.

In the experiment, the overlap of ϕ_a and ϕ_b is controlled with a state-dependent trapping potential. It consists of a static magnetic potential combined with a microwave near-field potential created with an on-chip waveguide. The microwave couples $|a\rangle$ and $|b\rangle$ to auxiliary states with a position-dependent Rabi frequency $\Omega_R(\mathbf{r})$. The coupling results in dressed states $|a\rangle$

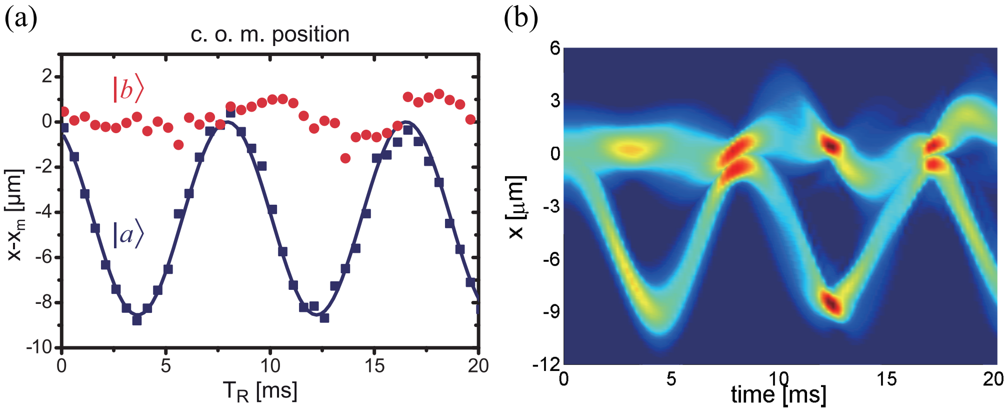

Figure 6.4: Oscillation of the atoms after the first $\pi/2$-pulse. In the scheme, the minimum of the trap for state $|a\rangle$ is displaced with $d_{\rm trap} = 4.3\,\mu$m by ramping up the power in the microwave near-field within $50\,\mu$s, while the minimum of the trap for state $|b\rangle$ remains unchanged. As a consequence the state $|a\rangle$ performs an oscillation with the amplitude $\simeq 2d_{\rm trap}$. The total number of atoms is $N = 400$. Trap frequencies: $\nu_x = 115\,$Hz, $\nu_\perp = 500\,$Hz. (a) Experiment: center of mass oscillation as a function of time [79]. The red circles (blue squares) corresponds to the state $|b\rangle$ ($|a\rangle$). T_R corresponds to the overall time the microwave was turned on. (b) Theory: longitudinal densities integrated along the tight confinement axes of the cylindrical traps obtained from dynamical simulation of the coupled Gross-Pitaevskii equations (4.10) with $\bar{N}_a = \bar{N}_b = 200$. Parameters are the same as in (a).

and $|b\rangle$ which are shifted in energy by the microwave potential $U^{(\varepsilon)}_{\rm mw}(\mathbf{r})$ with respect to the bare states. For different microwave frequency and polarization, the energy shifts for state $|a\rangle$ and $|b\rangle$ can be different or even opposing. The overall potentials seen by the dressed states are

$$U^{(\varepsilon)}_{\rm ext} = U_z + U^{(\varepsilon)}_{\rm mw}\,. \tag{6.6}$$

where U_z is the static magnetic trapping potential. In this way, the microwave near-field adds internal-state dependence to the potential in a controlled way. Combined with strong microwave power gradients, this leads to a state dependent potential as plotted in Fig.6.3 (b).

6.2.1 Large separation of the trapping potentials

In Fig.6.4 we show an experiment in which the condensates are state dependently split and recombined [79]. The total number of atoms $N = 400$. The frequency of the microwave field is chosen such that the detuning from the

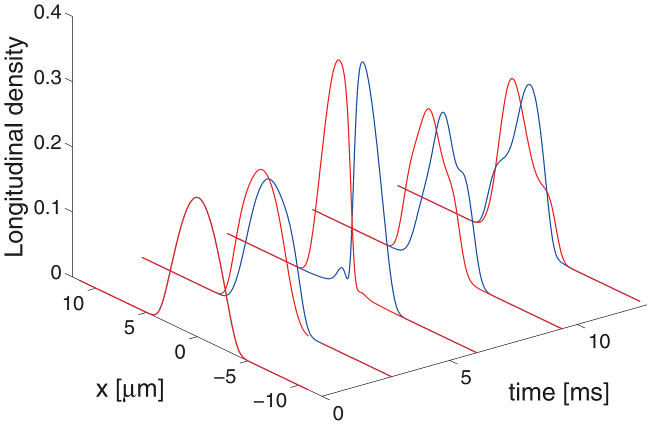

Figure 6.5: Longitudinal densities for the two states $|a\rangle$ (blue) and $|b\rangle$ (red) integrated along the tight confinement axes of the cylindrical traps calculated from dynamical simulation. The total number of atoms $N = 1250$. The trap frequencies $\nu_x = 109\,\text{Hz}$, $\nu_\perp = 500\,\text{Hz}$. After the first $\pi/2$-pulse, the minimum of the trap for both states are displaced with $d^{(a)}_{\text{trap}} = -0.126\,\mu\text{m}$, $d^{(b)}_{\text{trap}} = 0.394\,\mu\text{m}$ within $50\,\mu\text{s}$.

transition $|F = 1, m_F = -1\rangle \leftrightarrow |F = 2, m_F = -1\rangle$ is $2\pi \times 600\,\text{kHz}$. In this case the microwave is very far off resonance from all transitions connecting to $|b\rangle$. The potential $U^{(b)}_{\text{ext}}$ remains essentially unchanged. For the component a, the admixture with the auxiliary states is still small so that decoherence due to magnetic field noise has a small effect. After the preparation $\pi/2$-pulse, the microwave is switched on within $50\,\mu\text{s}$ which corresponds to a sudden displacement of the potential minimum for state $|a\rangle$ by $d_{\text{trap}} = 4.3\,\mu\text{m}$. The sudden displacement results in center of mass oscillation of the displaced component with the amplitude $\simeq 2d_{\text{trap}}$ and a frequency $\simeq \nu_x$, while the state $|b\rangle$ almost remains at rest, see Fig.6.4 (a). In Fig.6.4 (b) we show the result obtained from the numerical solutions of the coupled Gross-Pitaevskii equations (4.10) with $\bar{N}_a = \bar{N}_b = 200$. The small oscillations of the state $|b\rangle$ are due to the repulsive interactions between the atoms, which can be well explained in mean-field picture.

6.2.2 Small separation of the trapping potentials

As the auxiliary states used to create the state-dependent potentials do not have identical magnetic moments, the admixture of these states to the states $|a\rangle$ and $|b\rangle$ increases the sensitivity to the magnetic field noise. As a result, there is more phase noise when the microwave field is switched on, which is not favorable for achieving spin squeezing. The experimentalists then choose

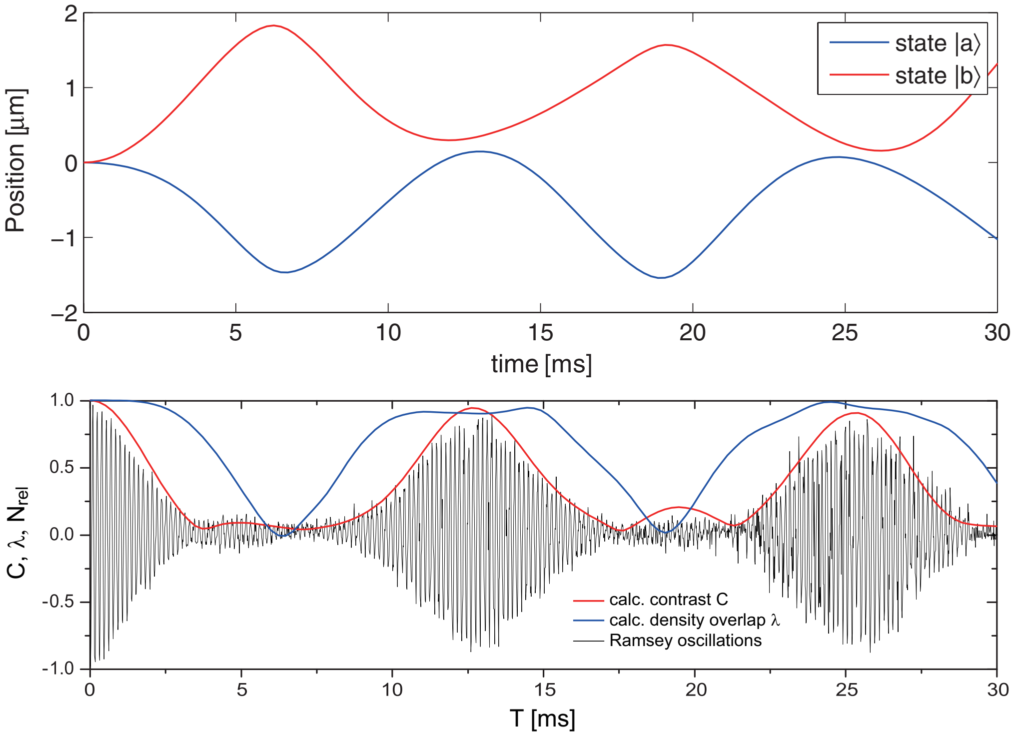

Figure 6.6: (Top) Simulated center of mass motion of the two states $|a\rangle$ (blue) and $|b\rangle$ (red) as a function of time. A slightly asymmetric splitting of the potentials (see the caption of Fig.6.5) results in an asymmetric oscillation. (Bottom) Measured Ramsey fringes in the normalized population difference N_{rel} after the second $\pi/2$-pulse and simulated contrast of the fringes C (red), which is modulated by the splitting and recombination of the BEC. The discrepancy between the measured contrast of the Ramsey fringes and the simulated contrast is probably due to the residual motion along the transverse direction which is not taken into account in the theoretical calculations. The simulated density overlap λ (blue) is shown for comparison. The parameters are the same as in Fig.6.5.

a larger detuning of the microwave near-field compared with the previous case, so that admixtures of other states to $|a\rangle$ and $|b\rangle$ are smaller and the states are more robust against magnetic field noise. In the spin squeezing experiment, the detuning of the microwave near-field is chosen as $2\pi \times 12\,\mathrm{MHz}$ from the transition $|F=1, m_F=0\rangle \leftrightarrow |F=2, m_F=0\rangle$. In this configuration, both states experience a microwave potential of opposite sign, and with different magnitude due to the different hyperfine transition strengths. When a microwave power of $P_{\mathrm{mw}} = 120\,\mathrm{mW}$ is launched into the chip, a splitting of the potential minima for the two states of $d_{\mathrm{trap}} = 0.52\,\mu\mathrm{m}$ results.

The mean-field effect becomes more important when the separation of the trap d_{trap} is small. In Fig.6.5 and 6.6, we show an example with trap separation $d_{\text{trap}} = 0.52\,\mu$m. The total number of atoms $N = 1250$. The trap frequencies are $\nu_x = 109\,$Hz, $\nu_\perp = 500\,$Hz. Note that in this case, the center of mass positions, Fig.6.6 (top), shows a maximum separation of about $3.0\,\mu$m $\gg 2d_{\text{trap}}$. The mean-field repulsion causes an almost complete separation of the two mode functions (see Fig.6.5 for the density distribution), even if their respective potentials are displaced by just a fraction of the Thomas-Fermi radius. Due to this effect, contrary to what one would first expect, the nonlinearity can be significantly increased with small trap separation. Another consequence of mean-field effect is that it takes 12.7 ms and not $1/\nu_x = 8.7\,$ms for the two components to overlap again.

6.3 Ramsey fringes and contrast

In the experiment for spin squeezing, besides reducing the fluctuation of one spin quadrature, it is also important to keep good phase coherence. The coherence can be deduced by measuring the contrast of Ramsey fringes. This is done by applying the following sequence: (i) prepare the initial state with the first $\pi/2$-pulse; (ii) switch on the microwave potentials to separate the two components for a duration time T; (iii) switch off the microwave potentials and apply the second $\pi/2$-pulse; (iv) measure the atom number difference between the two internal states as a function of T. In Fig.6.6 (bottom) we show the measured Ramsey fringes in the normalized population difference N_{rel}. The duration time T is changed from $0 \rightarrow 30\,$ms. The contrast of the fringes can be calculated with the quantum average of the field operators just before the second pulse [70],

$$C = \frac{2|\langle \int d^3r\, \hat{\Psi}_b^\dagger(\mathbf{r})\hat{\Psi}_a(\mathbf{r})\,\rangle|}{\sum_{\varepsilon=a,b}\langle \int d^3r\, \hat{\Psi}_\varepsilon^\dagger(\mathbf{r})\hat{\Psi}_\varepsilon(\mathbf{r})\,\rangle} \tag{6.7}$$

From the above equation, we can see that the contrast is influenced by two factors: (i) It is modulated by the splitting and recombination of the BEC. When the two components spatially overlap, the contrast reaches its maximum. (ii) It is also affected by the spin dynamics which causes the collapse of the relative phase at long times.

For an accurate description of our system, accounting for both the spatial and the spin dynamics, we use the dynamical theory presented in chapter 4. In Fig.6.6 (bottom) we show the corresponding contrast of the Ramsey fringes (red) calculated by Eq.(4.35) from the numerical simulation with dynamical modulus-phase approach. The good agreement with the measurement indicates that the simulation correctly accounts for the motion of the BEC in

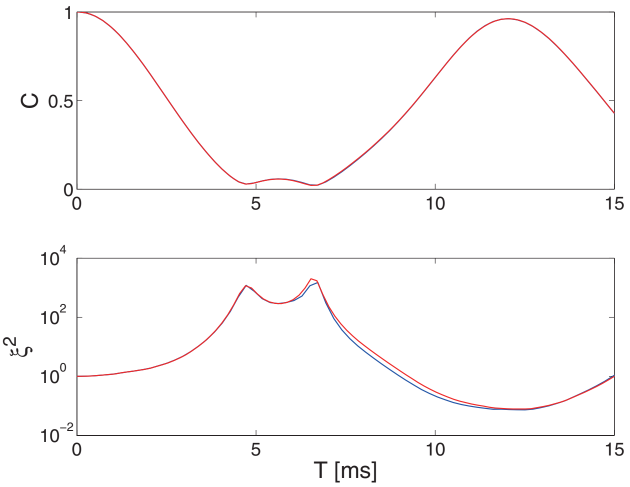

Figure 6.7: Comparison of full numerical simulation and the modulus-phase approach with the experimental trap configurations. (Top) The contrast of the fringes C as a function of trap separation time T. (Bottom) The squeezing parameter ξ^2 as a function of T. The total number of atoms $N = 640$. The trap frequencies: $\nu_x = 115\,\mathrm{Hz}$, $\nu_\perp = 515\,\mathrm{Hz}$. After the first $\pi/2$-pulse, the minimum of the trap for state $|a\rangle$ is displaced with $0.45\,\mu\mathrm{m}$ by ramping up the power in the microwave near-field within $50\,\mu\mathrm{s}$, while the minimum of the trap for state $|b\rangle$ remains unchanged. Red solid line: full numerical simulations with 192 Fock states. Blue solid line: modulus-phase approach.

the trap. In Fig.6.6 (bottom) we also show the density overlap λ (blue) as a function of time during the splitting for comparison.

To check the validity of our modulus-phase approach in the experimental trap configurations, we compare our calculations with a full numerical simulations (as described in section 4.1) carried out on a cluster machine for the number of atoms $N = 640$. In fig.6.7 we show the contrast of the Ramsey fringes C and the corresponding spin squeezing parameter ξ^2 as a function of the separation time T. Due to the reduction of the overlap, the squeezing parameter greatly increases when the contrast approaches 0. It decreases when the overlap increases again (contrast approaches 1). The good agreement confirms that both spatial and spin dynamics are correctly taken into account.

In order to optimize the squeezing, we shall tune the nonlinearity in such a way that the best squeezing is reached when the two components overlap again, and the contrast C approaches its maximum. The best squeezing time, which depends on the spin dynamics, can be estimated by calculating the two-mode model spin squeezing in presence of particle losses introduced

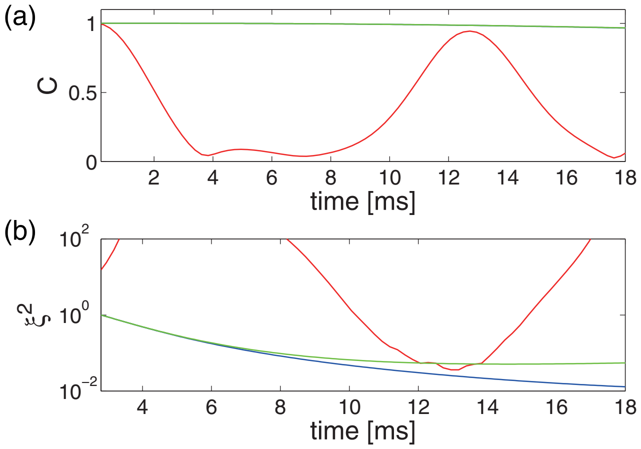

Figure 6.8: (a) Contrast of the Ramsey fringes calculated with the two-mode model with (green solid line) and without (blue solid line) losses, and calculated with the modulus-phase approach (red solid line). (b) Spin squeezing in modulus-phase approach (red solid line) and in two-mode model with (green solid line) and without losses (blue solid line). The parameters for the two-mode model are: $\chi_d^{2\mathrm{m}} = 0.49\,\mathrm{s}^{-1}$, $\chi_s^{2\mathrm{m}} = 0.04\,\mathrm{s}^{-1}$, $v = 55.03\,\mathrm{s}^{-1}$, calculated from the stationary solution (2.18). The rate constants for the losses are: $K_a^{(1)} = K_b^{(1)} = 0.2\,\mathrm{s}^{-1}$, $K_b^{(2)} = 119 \times 10^{-21}\,\mathrm{m}^3\mathrm{s}^{-1}$ [64], $K_{ab}^{(2)} = 78 \times 10^{-21}\,\mathrm{m}^3\mathrm{s}^{-1}$ [64], $K_a^{(3)} = 6 \times 10^{-42}\,\mathrm{m}^6\mathrm{s}^{-1}$ [65]. Other parameters are the same as in Fig.6.5.

in chapter 3. Here we give an example with the same parameters as in Fig.6.5. The nonlinear parameter, $\chi_d^{2\mathrm{m}} = 0.49\,\mathrm{s}^{-1}$, is calculated from the stationary solution of Gross-Pitaevskii equation (2.18) with the corresponding trap separation. In Fig.6.8 (b), we show the squeezing parameter as a function of time calculated from two-mode model in presence of losses (green solid line), and without losses (blue solid line). The squeezing parameter calculated from dynamical modulus-phase approach is also shown (red solid line). According to the figure, the dynamical squeezing parameter reaches its minimum at about 12.7 ms when the two components overlap again. This time is very close to the best squeezing time in presence of losses, although without losses it comes much later. Note that the two-mode curve obtained for stationary BEC in separated traps ($d_{\mathrm{trap}} = 0.52\,\mu\mathrm{m}$) is shifted by 2.8 ms in time in the figure, since before that the two components are not well separated and χ_d therefore is very small[1]. In Fig.6.8 (a) we show the contrast C calculated from the two-mode model with (blue solid line) and without (green solid line) losses. In this case, the contrast is not affected by the splitting and recombi-

---

[1] This can be further confirmed by comparing the two-mode model spin squeezing curve with the “extracted” spin squeezing which is indeed flat during the first 2.8 ms.

nation of the BEC. At 12.7 ms, the contrast $C = 98.6\,\%$. The slight reduction is due to the spin dynamics which causes phase spreading. The contrast calculated from the modulus-phase approach is also plotted (red solid line) for comparison. At the same time, $C = 94.4\,\%$. The small difference between the two approaches are due to the non perfect overlap.

6.4 Main results and data analysis

In this section we present the experiment sequence and the main result published in [40]. In order to explain the observed squeezing signals, besides the model we setup in chapter 3 and 4, taking into account the particle losses and spatial dynamics, we further introduce some technical noise in our theoretical model, such as fluctuations of the microwave power, the phase noise, etc. The observed spin squeezing can be well explained after taking into account these imperfections.

6.4.1 Experimental sequence

The experiment starts from a pure BEC of $N = 1250 \pm 45$ atoms in the state $|a\rangle$ in a harmonic trap with longitudinal (axial) trap frequency $\nu_x = 109\,\mathrm{Hz}$ ($\nu_\perp = 500\,\mathrm{Hz}$). Then the states $|a\rangle$ and $|b\rangle$ are coherently coupled with a resonant $\pi/2$-pulse, preparing a coherent spin state. The microwave near-field is turned on within $50\,\mu\mathrm{s}$, separating the two traps by $d_{\mathrm{trap}} \simeq 0.52\,\mu\mathrm{m}$ (for parameters of the microwave near-field see subsection 6.2.2). After 12.7 ms, the two BEC components perform one oscillation and recombine. The microwave potential is switched off, and the squeezing dynamics, as well as the relative atomic motion, stops. Then another pulse with variable durations is applied to rotate the state around the mean spin by an angle Θ. Finally, the number of atoms in both components N_a and N_b are detected, consequently the transverse spin components $S_\Theta = (\cos\Theta)S_z - (\sin\Theta)S_y$ before the final rotation are obtained. The whole scheme can be illustrated on the Bloch sphere as shown in Fig.6.9 (a)-(d). In (e) we plot the simulated center of mass motion of the two BEC components, and in (f) we show the simulated contrast of the Ramsey fringes and the experimental sequence corresponding to (a)-(d).

According to Fig.6.9 (e), after the two BEC components are recombined, there is still a small residual center of mass motion. However, the simulated contrast of the Ramsey fringes is about 94 %, predicting good phase coherence between the two components. As we discussed in the previous chapter, the reduction of the contrast is due to two effects. One comes from the overlap of

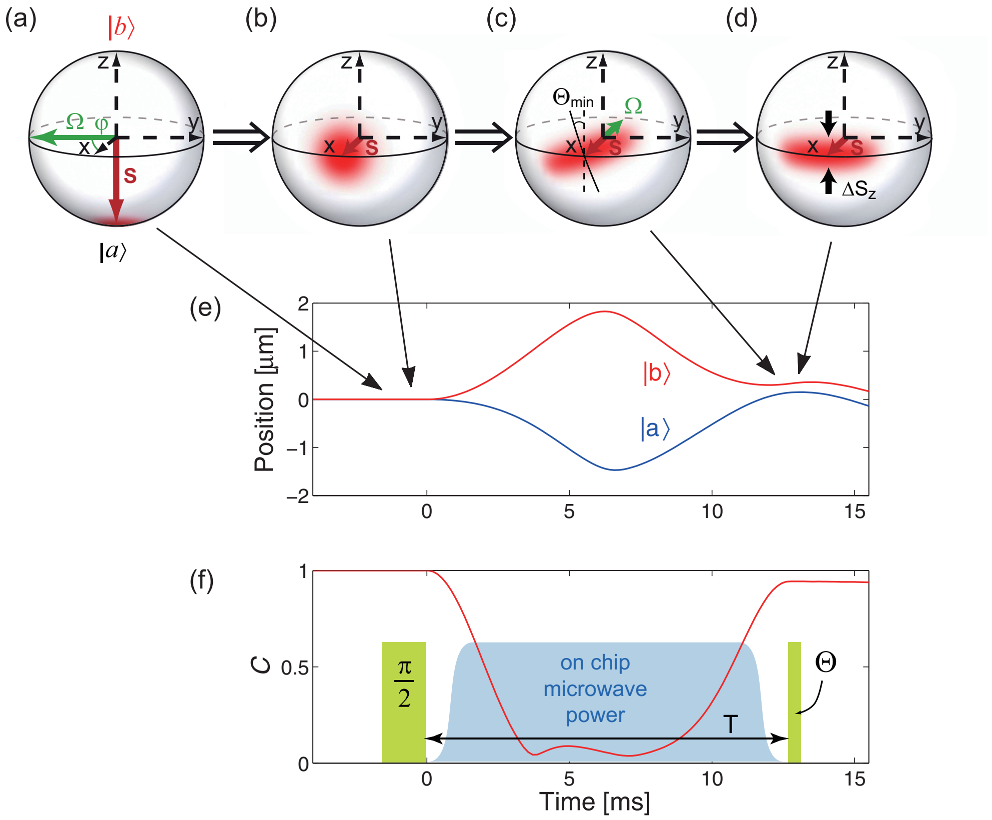

Figure 6.9: (a)-(d) Evolution of the BEC internal state on the Bloch sphere. Starting with all atoms in $|a\rangle$, a $\pi/2$-pulse prepares a coherent spin state with mean spin along x and isotropic quantum noise in the yz-plane (fuzzy red circle). Subsequent nonlinear evolution deforms the noise circle into an ellipse, creating a spin squeezed state with reduced noise at an angle Θ_{min}. A second pulse rotates the state around $-x$ by a variable angle Θ, followed by detection of S_z. (e) The simulated center of mass motion of the two states $|a\rangle$ (blue) and $|b\rangle$ (red) as a function of time. (f) The simulated contrast of the Ramsey fringes and the experiment sequence. In between the pulses for internal-state manipulation (green), a state-dependent microwave potential is turned on (blue; pulse durations and microwave ramp times exaggerated for clarity). It dynamically splits and recombines the two BEC components, so that nonlinearity parameter $\chi > 0$ during the time T.

the two BEC components, and the other comes from the phase spreading. In section 6.3 we calculated χ_d^{2m} corresponding to this trap configuration, which rules the phase dynamics and squeezing in a stationary two-mode model. $\chi_d^{\text{2m}} = 0.49\,\text{s}^{-1}$ results in $\sim 1.4\,\%$ of reduction of contrast at $t = 12.7\,\text{ms}$. A more accurate calculation accounting for the dynamical evolution of the condensate wave function, the “extracted spin squeezing” model, gives the

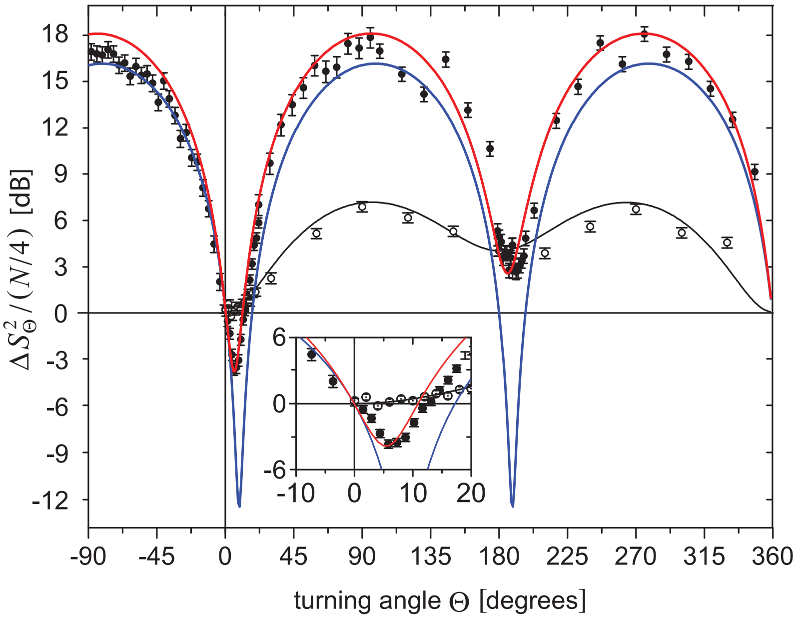

Figure 6.10: Observed spin noise for the spin squeezed state (solid circles) and for a coherent spin state (reference measurement, open circles). The normalized variance $\Delta_n S_\Theta^2 = 4\Delta S_\Theta^2/\langle N\rangle$ is shown as a function of the turning angle Θ in the yz-plane, with statistical error bars. The photon shot noise due to the imaging process has been removed. In the squeezed state, a spin noise reduction of $-3.7 \pm 0.4\,\mathrm{dB}$ is observed for $\Theta_{\mathrm{min}} = 6^\circ$, corresponding to $\xi^2 = -2.5{\pm}0.6\,\mathrm{dB}$ of metrologically useful squeezing for the Ramsey contrast of $C = (88{\pm}3)\%$. Solid lines are results from our dynamical simulation. Blue: squeezed state with losses but without technical noise; red: squeezed state with losses and technical noise; black: reference measurement with losses and technical noise.

same result ($C = 98.2\,\%$), implying that the reduction of the contrast is mainly due to non perfect overlap between the clouds.

6.4.2 Data analysis

The spin noise reduction obtained from our theoretical calculation is shown in Fig.6.10 along with the data measured in the experiment. The data for a coherent spin state where the traps were not separated during the sequence, so-called reference measurement, is also shown for comparison. We plot the normalized variance $\Delta_n S_\Theta^2 = 4\Delta S_\Theta^2/\langle N\rangle$, so that $\Delta_n S_\Theta^2 = 0\,\mathrm{dB}$ corresponds to the standard quantum limit.

In the figure, the circles represent the experiment data corresponding to the squeezing measurement (solid circles) and the reference measurement (open circles). In the squeezing measurement, the spin noise $\Delta_n S^2_\Theta$ falls significantly below the standard quantum limit, reaching a minimum of $\Delta S^2_\Theta = -3.7 \pm 0.4\,\mathrm{dB}$ at $\Theta_{\min} = 6°$. The corresponding measured interference contrast is $C = (88 \pm 3)\,\%$, which is in fact worse than the simulated one 94 %. The difference can most likely be explained by small motion in the transverse direction which is excited in the experiment but not modeled. The corresponding squeezing parameter $\xi^2 = -2.5 \pm 0.6\,\mathrm{dB}$, proving that the state is useful for quantum metrology and the condensate atoms are entangled. The reference measurement, by contrast, stays above the standard quantum limit for all values of Θ.

The solid lines are the theoretical calculations in which we add the effect of particle losses (one, two, three-body) as well as several technical noise sources, which will be discussed separately in the following.

Spin squeezing without technical noise

The blue line in Fig.6.10 shows the expected squeezing taking into account atom losses and spatial dynamics but no technical noise. In order to obtain accurate rate constants for the losses, the experimentalists measured the life times of the states a and b separately and in a 50/50 superposition in the trap without separation. In the theory, we calculate the number of atoms remaining in the trap with Monte-Carlo simulations, in which we adjust the rate constants $K_b^{(2)}$, $K_{ab}^{(2)}$, and $K_a^{(3)}$ to fit the measured data, while the other rate constants are referred to literatures (one-body losses are determined by measurement). A comparison between measurement and simulation results is shown in Fig.6.11. Then the rate constants determined in this way are used in all simulations related to particle losses.

The variance $\Delta S^2_{\Theta\,\mathrm{2m}}$, including the effect of atom losses, is calculated by Monte-Carlo simulations within the two-mode model. With the experimental parameters, $\chi_d^{\mathrm{2m}} = 0.49\,\mathrm{s}^{-1}$, $\chi_s^{\mathrm{2m}} = 0.04\,\mathrm{s}^{-1}$, $v = 55.03\,\mathrm{s}^{-1}$, at $t \simeq 12.7\,\mathrm{ms}$, the fraction of lost particles is less than 3 %. The final result ΔS^2_Θ, taking into account atom losses as well as the spatial dynamics is obtained by

$$\Delta S^2_\Theta = \Delta S^2_{\Theta\,\mathrm{SP}} + \Delta S^2_{\Theta\,\mathrm{LS}}\,, \tag{6.8}$$

where we have defined

$$\Delta S^2_{\Theta\,\mathrm{LS}} = \Delta S^2_{\Theta\,\mathrm{2m}}(\text{with losses}) - \Delta S^2_{\Theta\,\mathrm{2m}}(\text{without losses}) \tag{6.9}$$

as the variance due to losses, and $\Delta S^2_{\Theta\,\mathrm{SP}}$ is the variance calculated with the modulus-phase approach including the spatial dynamics. As shown in Fig.6.10, the maximum reduction in the normalized variance calculated in this way is $-12.8\,\mathrm{dB}$ at $\Theta \simeq 8°$, significantly larger than observed.

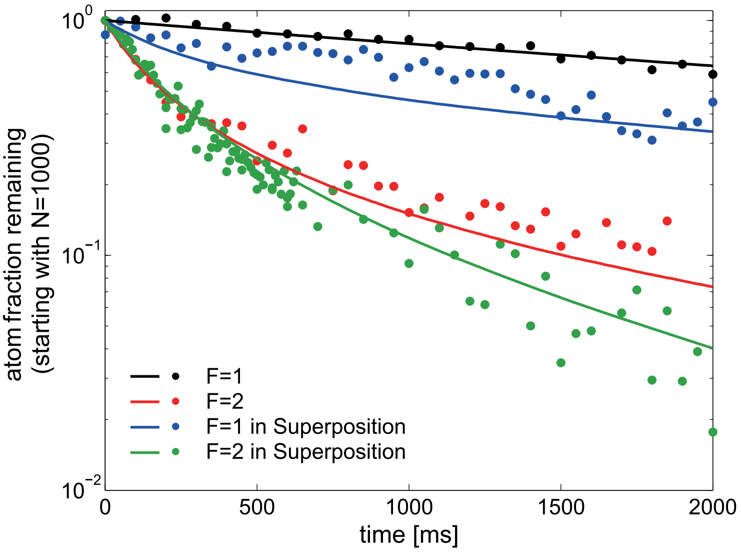

Figure 6.11: Measurements and simulations for atoms prepared in pure state $|a\rangle$ and $|b\rangle$ and in an even superposition $(|a\rangle + |b\rangle)/\sqrt{2}$. The solid lines are the results from the Monte-Carlo simulation with rate constants adjusted for a best fit to the experimental data. The fitted rate constant: $K_a^{(1)} = K_b^{(1)} = 0.2\,\mathrm{s}^{-1}$, $K_a^{(2)} = 0$, $K_b^{(2)} = 70\times 10^{-21}\,\mathrm{m}^3\mathrm{s}^{-1}$, $K_{ab}^{(2)} = 50\times 10^{-21}\,\mathrm{m}^3\mathrm{s}^{-1}$, $K_a^{(3)} = 6\times 10^{-42}\,\mathrm{m}^6\mathrm{s}^{-1}$, $K_b^{(3)} = 0$. The corresponding wave function needed to calculate the loss rate in Eqs.(3.3)-(3.4) can be obtained from the stationary solution (2.18), identical traps for both components. In the case of 50/50 superposition, one has $\chi_d^{2\mathrm{m}} = 1.73 \times 10^{-3}\,\mathrm{s}^{-1}$, $\chi_s^{2\mathrm{m}} = 4.57 \times 10^{-2}\,\mathrm{s}^{-1}$, $v = 45.04\,\mathrm{s}^{-1}$. The nonlinearity in this case is negligible.

Estimate the effect of technical noise

The red line Fig.6.10, which describes the measured data well, additionally includes the fluctuation of the total number of atoms N, fluctuations of the microwave power P_{mic} of 0.5 % r.m.s., and phase noise of $\Delta\varphi = 8^\circ$ r.m.s. All fluctuations are consistent with independent measurements.

- Fluctuations of total number of atoms

The standard deviation of the total number of atoms N in the experiment is 45. Only shots where the total atom number differs by no more than 150 from the mean atom number are used for the analysis. In our calculation with the modulus-phase approach, after the results obtained for well defined total number of atoms, we apply a further averaging of N for Eqs.(4.35)-(4.39) over a normal probability distribution

$$P(N) \propto \exp\left[-\frac{\left(N-\bar{N}\right)^2}{2\sigma_N^2}\right] \tag{6.10}$$

with $\sigma_N = 45$, $\bar{N} = 1250$, and N is taken from 1100 to 1400. We find that, with this standard deviation, the fluctuation of the total number of atoms has very limited effect to the squeezing. This is confirmed by the experiments, where it shows that a tighter (75 atoms) or wider (250 atoms) post-selection does not significantly change the data quality.

- Fluctuations of microwave power

Another source of technical noise comes from the fluctuations of the microwave power P_{mic} during the second coupling pulses. Due to fluctuating microwave level shifts, it results in the fluctuations of the detuning δ_{mw} in the two-photon drive, which makes the resonant pulse become non-resonant, implying that, on the Bloch sphere, the axis around which we turn the noise ellipse drifts from the equator, and becomes misaligned with the mean spin (see the green Rabi vector $\vec{\Omega}$ in Fig.6.12 (a)). Assume that $\Delta\vartheta$ is the drifting angle between $\vec{\Omega}$ and the equatorial plane. The biggest effect to S_z component for a given $\vec{\Omega}$ will appear when the rotation approaches to 180°, i.e. $\Theta = 180°$. This is the reason why the second dip in Fig.6.10 does not go down below the value for $\Theta = 0$ (also for the reference measurement). The first dip at $\Theta \simeq 6°$ is weakly affected.

The energy level shifts due to the microwave in pulse are 7.6 kHz. Together with the Rabi frequency of the two-photon drive $\Omega_R = 2.1\,\mathrm{kHz}$, this results in the drifting angle $\Delta\vartheta$ as a function of fluctuations of the microwave power

$$\Delta\vartheta = \frac{7.6}{2.1}\frac{\Delta P_{\mathrm{mic}}}{P_{\mathrm{mic}}}\,. \tag{6.11}$$

The measured fluctuation of the pulse power is $\Delta P_{\mathrm{mic}}/P_{\mathrm{mic}} = 0.5\,\%$ r.m.s., resulting the standard deviation of the fluctuation of ϑ about 1°.

The other effect brought by the fluctuation of the microwave power is that the angle Θ by which we turn the noise ellipse fluctuates from shot to shot. Since the Rabi frequency $\Omega_R \propto \sqrt{P_{\mathrm{mic}}}$, the dependence of the $\Delta\Theta$ (see Fig.6.12 (b)) on the fluctuation of the pulse can be formulated as

$$\frac{\Delta\Theta}{\Theta} = \frac{\Delta\Omega_R}{\Omega_R} = \frac{1}{2}\frac{\Delta P_{\mathrm{mic}}}{P_{\mathrm{mic}}}\,. \tag{6.12}$$

For the largest rotation where $\Theta = 360°$, this results in the standard deviation of the fluctuation of Θ about 0.9°. In the experiment, the measured variance

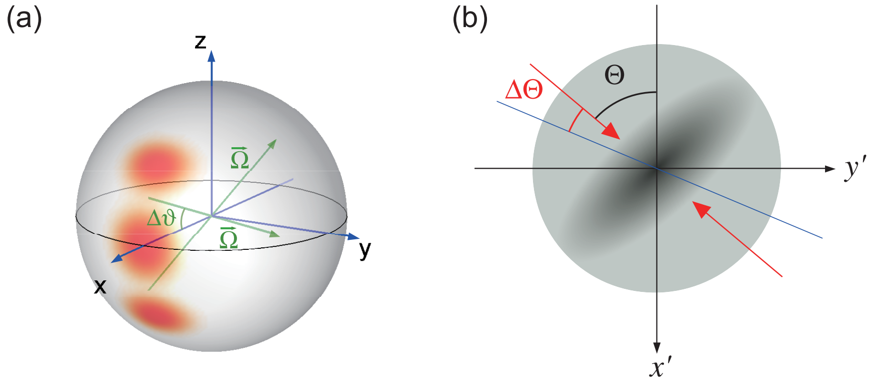

Figure 6.12: (a) Illustration of the fluctuation of Rabi vector $\vec{\Omega}$ on the Bloch sphere. The mean spin $\vec{S}$ is aligned with axis-x, and the second pulse applies a rotation around $\vec{\Omega}$ (green) by an angle Θ. Assume that $\vec{\Omega}$ is drifted above (below) the equatorial plane by an angle $\Delta\vartheta$ due to the fluctuation of the microwave power. After rotating 180°, the mean spin will shift $\pm 2\Delta\vartheta$ from the equatorial plane. (b) Illustration of the fluctuation of Θ in the plane orthogonal to the mean spin, where Θ is the angle between the minor axis of the noise ellipse (red arrow) and axis-x'. Due to the fluctuation of the pulse power, the noise ellipse is over-rotated (scantly-rotated) by an angle $\Delta\Theta$ (blue line). Here $\Delta\vartheta$ and $\Delta\Theta$ are exaggerated for clarity.

of spin ΔS_z^2 coming back to shot noise at $\Theta = 360°$ implies that the effect of $\Delta\Theta$ within this level is very limited.

In order to take into account these technical noise in our theoretical model, we apply a further averaging of ϑ and Θ for the quantum averages obtained from Eqs.(2.41)-(2.43) over a normal probability distributions $P(\vartheta)$ and $P(\Theta)$. Since these fluctuations are determined by the microwave power fluctuation (6.11) and (6.12), we choose

$$P(\vartheta) \propto \exp\left[-\frac{\left(\vartheta - \bar{\vartheta}\right)^2}{2\sigma_\vartheta^2}\right], \tag{6.13}$$

where $\sigma_\vartheta = 0.018$ obtained from Eq.(6.11) with $\Delta P_{\mathrm{mic}}/P_{\mathrm{mic}} = 0.5\,\%$ r.m.s., and $\bar{\vartheta} = \pi/2$ is the angle between the mean spin and the axis-z. When $\vartheta = \bar{\vartheta}$, the Rabi vector is perfectly aligned with the mean spin. Then for each ϑ, linked $\Delta\Theta/\Theta$ with $\Delta\vartheta$ via Eq.(6.11) and (6.12), the angle Θ is given by

$$\frac{\Theta - \bar{\Theta}}{\bar{\Theta}} = 0.138\left(\vartheta - \bar{\vartheta}\right). \tag{6.14}$$

Therefore, the fluctuation of ϑ and the fluctuation of Θ are correlated.

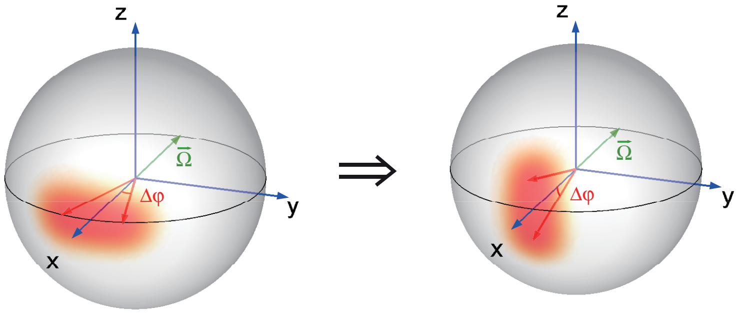

Figure 6.13: (a) Illustration of the phase noise which spreads the noise ellipse (fuzzy red) along the equator. Due to the phase noise, the mean spin has an uncertainty $[-\Delta\varphi, \Delta\varphi]$. (b) After rotating around the Rabi vector $\vec{\Omega}$ (green vector) by 90° or 270°, the phase noise is transferred to the fluctuation of S_z.

- Phase noise

The phase noise is the main reason why the maximum achieved squeezing is smaller than the theoretically predicted value. As it always spreads the noise ellipse along the equator, as shown in Fig.6.13, the impact of phase noise on ΔS_Θ^2 reaches its maximum when the angle Θ approaches 90° and 270°. It is the case for both reference measurements and squeezing measurements.

A likely explanation of the phase noise are fluctuations of the magnetic trap position in the inhomogeneous microwave near-field caused by a fluctuating current or by mechanical vibrations. Consequently, the phase noise in the reference sequence is smaller compared with that in the squeezing measurement. Other sources of technical noise, such as the fluctuation of the microwave power in the coplanar waveguide, fluctuations of the external magnetic field, power fluctuations and phase instabilities of the radio frequency and microwave generators and amplifiers for the two-photon drive, and fluctuations of the on-chip currents together contribute a phase noise of about 2°, as determined in various measurements in the experiment (see Supplementary Information of [40]).

In our theoretical model, we take into account the phase noise by applying an average of φ over a normal probability distribution for Eqs.(2.41)-(2.43),

$$P(\varphi) \propto \exp\left[-\frac{(\varphi-\bar{\varphi})^2}{2\sigma_\varphi^2}\right], \tag{6.15}$$

with $\sigma_\varphi = 3°$ for the reference measurement and $\sigma_\varphi = 8°$ for the squeezing measurement. Here $\bar{\varphi}$ is the azimuthal angle for the mean spin.

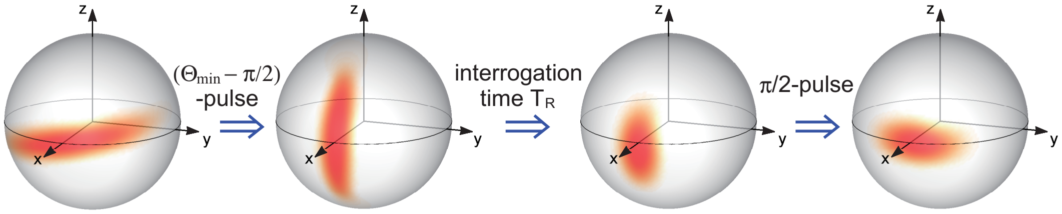

Figure 6.14: The illustrated scheme of using the spin squeezed state for interferometric measurement. Starting with a spin squeezed state, a $(\Theta - \pi/2)$-pulse rotate the state so that its squeezed axis is oriented along the equator of the Bloch sphere. During the interrogation time, the interferometer phase is accumulated along the squeezed direction. Finally a $\pi/2$-pulse is applied to read out the interferometer.

Note that here we model three kinds of technical noise and take them into account in the red curve of Fig.6.10. Only for phase noise we put different values for squeezing measurement and reference measurement. Due to the presence of microwave near-field, the phase noise cannot be estimated consistently in the two measurements, as discussed before. This makes σ_φ as a fitting parameter of the model. It also implies that any other technical noise which is not modeled will be treated as phase noise. Consequently, to fit the data in the dips, we might have overestimated the phase noise. This explains why the red curve at $-90°$ does not fit perfectly the measured data.

6.5 Using the squeezed state in an atomic clock

In order to use the squeezed state to improve the sensitivity of an interferometric measurement such as an atomic clock, it is important that the squeezing can be kept for long interrogation times. Indeed, apart from thermal effects, the two fundamental limitations of the squeezed state's lifetime are (i) particle loss and (ii) quantum phase spreading which occurs after the production of the squeezed state, i.e. during the interrogation time. One can significantly reduce the influence of these effects by transferring the atoms into a shallow trap with reduced atom density after the squeezing sequence. Also, since during the interrogation time no microwave near-field is present, technical phase noise can be suppressed to the extremely low level.

Following the treatment of section 3.3, we performed Monte-Carlo simulations to see how long the squeezing remain after creation when performing a Ramsey sequence in a shallow trap. The simulated sequence works as follows: we produce a spin squeezed state assuming no technical fluctuations.

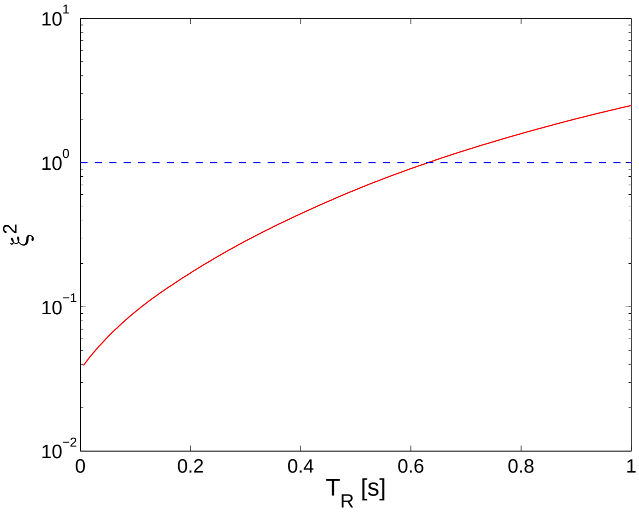

Figure 6.15: Squeezing lifetime in a clock sequence. Results of a Monte-Carlo simulation on how the squeezing evolves under particle losses and residual nonlinearity in a shallow trap which could be used in a clock experiment. The spin squeezed state is created with the scheme presented in subsection 6.4. Before the Ramsey sequence, the atoms are transferred to a shallow trap with the frequencies $f_x = 10\,\mathrm{Hz}$, $f_\perp = 50\,\mathrm{Hz}$. The residual nonlinearity is $\chi_d^{2\mathrm{m}} = 5.2 \times 10^{-5}\,\mathrm{s}^{-1}$. The dashed line indicates the standard quantum limit. The state remains squeezed for Ramsey interrogation time T_R of up to 0.6 s in this trap.

The trap configuration is the same as in section 6.4, resulting the two-mode nonlinearity $\chi_d^{2\mathrm{m}} = 0.49\,\mathrm{s}^{-1}$. The state is then transferred into the weaker trap without separation ($f_x = 10\,\mathrm{Hz}$, $f_\perp = 50\,\mathrm{Hz}$) after 12.7 ms. The residual nonlinearity in this trap is $\chi_d^{2\mathrm{m}} = 5 \times 10^{-5}\,\mathrm{s}^{-1}$, quantum phase spreading can therefore be neglected. We then rotate the state by $(\Theta_{\mathrm{min}} - \pi/2)$ so that its squeezed axis is oriented along the equator of the Bloch sphere, realizing a phase-squeezed state. In this case, squeezing is more fragile to the phase noise, as well as to the losses. After a variable Ramsey time T_R, during which the interferometer phase is accumulated along the squeezed direction, a $\pi/2$-pulse is applied to read out the interferometer. The whole scheme is illustrated in Fig.6.14. The rate constants for particle losses are the same throughout the process, as shown in the caption of Fig.6.11. However, after transferring to the shallow trap, the loss rate is decreased as the atom density is reduced.

Fig.6.15 shows ξ^2 as a function of T_R. The use of the squeezed state in such a trap would improve the sensitivity for T_R of up to 0.6 s compared to a classical interferometer with a coherent spin state as input. Compared with Fig.3.7 where the state is not rotated by $(\Theta_{\mathrm{min}} - \pi/2)$ at the beginning of Ramsey time, the spin squeezing in the Ramsey sequence is more fragile to the losses. This is because, as described in chapter 3, each loss event will cause a random phase shift of the state. If the squeezed axis is aligned along the equator, the state will suffer much more from these random phase shift. This explains why in Fig.6.15 at the end of 1.0 s there is completely no squeezing, while in Fig.3.7 the state remains squeezed.

Chapter 7

Condensate in a double-well: Paris experiment

In the previous chapters, our studies are mainly focused on a BEC with two internal states. However, our model can also be applied to two external modes of BEC, for example a condensate coherently split in a double well potential, provided a term describing a coherent coupling between the two components included in the Hamiltonian. In this case, two effects nontrivial contribute to the system: (i) the repulsive interactions between the atoms reduces the fluctuations of the atom number difference, consequently increasing the uncertainty of the relative phase; (ii) the coherent coupling between the two components due to tunneling tends to reestablish the relative phase. The analogies in the system with internal states, considered before, would be to keep the coherent coupling during the squeezing.

In the experiment carried out in Paris, a ^{87}Rb Bose-Einstein condensate created on an atom chip was split into two parts by raising a barrier in the middle of the trap, deforming the trap from a single well to a double well. At low enough temperature, number squeezed states with relative population fluctuations -4.9 dB below shot-noise were observed. In section 7.1, we briefly summarize the experiment results obtained by the experimentalists. In section 7.2 we describe our theoretical calculations within the framework of the two-mode model, and compare our result with the experimental data obtained at low temperature. This part of work is published in [43]. In section 7.3 we extend our studies to finite temperature, where the two-mode model is no longer valid, and we show results based on a thermal equilibrium approach [82].

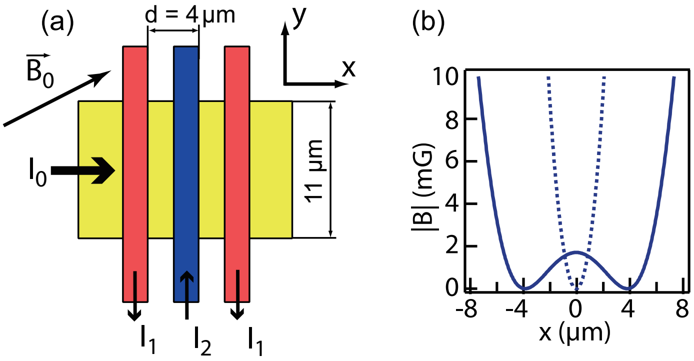

Figure 7.1: (a) Illustration of chip geometry (b) Profile of the trapping potential along the splitting axis x for $I_2 = 0\,\mathrm{mA}$ (dashed line) and $I_2 = 2.4\,\mathrm{mA}$ (solid line).

7.1 Summary of the experimental results

In the experiment, the double well potential is created by a two-layer atom chip. It is a static magnetic potential with adjustable barrier height and well spacing, in which the ^{87}Rb atoms in the Zeeman state $|F = 2, m_F = 2\rangle$ are trapped. In the transverse directions, the trap is approximately harmonic with frequencies $\nu_{y,z} \sim 1\,\mathrm{kHz}$. The trap is split along the slow axis by changing the wire current I_2 on the chip (see Fig.7.1), allowing for double wells consisting of two approximately spherical traps. A thermal gas or a condensate is split in this double well, and the fluctuations of the atom number difference $N_l - N_r$ between the left and the right well after the splitting are measured.

In the first experiment, by increasing the current I_2 from 0 to 3.9 mA, an almost pure BEC of 1300 atoms is split within different ramping time τ_r. The experimentalists observe a decrease of fluctuations below the shot-noise limit with increasing τ_r up to 50 ms, followed by a slow increase for longer times, see Fig.7.4 in section 7.2.

In the second experiment, the effect of the temperature on the squeezing is investigated. A gas of ^{87}Rb is split with fix total ramping time $\tau_r = 50\,\mathrm{ms}$. The initial temperature is varied by changing the final frequency of the evaporative cooling ramp. The measured squeezing is plotted in Fig.7.6. Total atom number and condensed fraction are also shown. According to the figure, a number squeezing down to -4.9 dB is observed at low temperature. On the other hand, when the condensed fraction roughly equals the thermal fraction, super-Poissonian fluctuations with a maximum of $+3.8\,\mathrm{dB}$ are observed. Poissonian fluctuations are recovered above the critical temperature.

7.2 Dynamical two-mode model

In this section, we describe our theoretical calculations within the framework of two-mode model, in which we assume that only the lowest two energy modes of the system are relevant to the dynamics, and we neglect the other modes orthogonal to these two modes. This is valid at very low temperature $T \ll T_c$ where the population in the higher lying energy modes is negligible.

An intuitive choice of the two modes would be the condensate wave functions localized in each well. Here we are interested in the regime where these two BECs are weakly linked by tunneling effect, so-called Josephson regime [83]. In this case, the wave functions can be expressed in terms of stationary symmetric and antisymmetric eigenstates of the GPE [84].

7.2.1 Construction of the two-mode model

We consider a symmetric double well potential along axis-x, and harmonic along axis-y, z. The many-body Hamiltonian can be written as

$$\mathcal{H} = \int d^3r\, \hat{\Psi}^\dagger(\mathbf{r}) \left[-\frac{\hbar^2\nabla^2}{2M} + U(\mathbf{r}) \right] \hat{\Psi}(\mathbf{r}) + \frac{g}{2} \int d^3r\, \hat{\Psi}^\dagger(\mathbf{r})\hat{\Psi}^\dagger(\mathbf{r})\hat{\Psi}(\mathbf{r})\hat{\Psi}(\mathbf{r}) \tag{7.1}$$

where $U(\mathbf{r})$ is the external double well trap potential, $g = 4\pi\hbar^2 a/M$, a is the s-wave scattering length. At very low temperature $T \ll T_c$, we can assume that only two lowest energy states are macroscopically populated. As we did in the two-mode model for spin squeezing, the field operators can be approximated as

$$\hat{\Psi}(\mathbf{r}) = c_l\phi_l(\mathbf{r}) + c_r\phi_r(\mathbf{r}), \tag{7.2}$$

where c_l and c_r are annihilation operators for the two modes, and $\phi_{l,r}(\mathbf{r})$ are the condensate wave functions localized in each well (left and right). They can be constructed by the symmetric $\phi_S(\mathbf{r})$ and antisymmetric $\phi_A(\mathbf{r})$ stationary eigenstates of the GPE [84, 85]

$$\phi_l(\mathbf{r}) = \frac{\phi_S(\mathbf{r}) - \phi_A(\mathbf{r})}{\sqrt{2}}, \quad \phi_r(\mathbf{r}) = \frac{\phi_S(\mathbf{r}) + \phi_A(\mathbf{r})}{\sqrt{2}}. \tag{7.3}$$

where $\phi_{S,A}(\mathbf{r})$ satisfy

$$\mu_{S,A}\phi_{S,A}(\mathbf{r}) = \left[-\frac{\hbar^2}{2M}\nabla^2 + U(\mathbf{r}) + Ng|\phi_{S,A}(\mathbf{r})|^2 \right] \phi_{S,A}(\mathbf{r}), \tag{7.4}$$

with $\mu_{S,A}$ being the corresponding chemical potential. $\phi_S(\mathbf{r})$ and $\phi_A(\mathbf{r})$ are the ground state and first excitation state of the Gross-Pitaevskii Hamiltonian. The advantage of expressing the two modes wave functions in terms of $\phi_{S,A}(\mathbf{r})$ is that these two eigenstates are the local nonlinear modes of the entire double well trap that can be found exactly for any given trap separation [86]. Indeed, one should note that the two-mode model has a limited validity in the case of low barrier, when in principle one is not allowed to neglect higher excited modes. However, it becomes more and more accurate the higher the barrier gets, since in this case the two lower lying modes move closer together in energy compared to the higher ones. Hence it should allow a good description of the splitting process [87].

By using the atom-number states in the left and right well, Eq.(7.2), as the basis of the Hilbert space of the system, the two-mode Hamiltonian can be written as [85, 88],

$$\begin{aligned}\mathcal{H}_{2M} &= \frac{E_c}{8}(c_l^\dagger c_l - c_r^\dagger c_r)^2 - \frac{E_j}{N}(c_l^\dagger c_r + c_r^\dagger c_l) + \frac{\delta E_c}{4}(c_l^\dagger c_r + c_r^\dagger c_l)^2 \\ &= \frac{E_c}{2}S_z^2 - \frac{2E_j}{N}S_x + \delta E_c S_x^2\end{aligned} \tag{7.5}$$

where the terms proportional to the total atom number have been ignored, and in the second line of (7.5) we have used the definition of the spin operators given by (2.28)-(2.30). E_j and E_c are so-called the Josephson coupling energy and the charging energy respectively, both of which can be calculated by solving the stationary solution of the Gross-Pitaevskii equation (7.4) [88],

$$E_c = 8k_{SA}\ , \tag{7.6}$$

$$E_j = \frac{N}{2}(\mu_A - \mu_S) - \frac{N(N+1)}{2}(k_{AA} - k_{SS})\ , \tag{7.7}$$

$$\delta E_c = \frac{1}{4}(k_{SS} + k_{AA} - k_{SA})\ , \tag{7.8}$$

with

$$k_{ij} = \frac{g}{2}\int d^3r\, |\phi_i(\mathbf{r})|^2 |\phi_j(\mathbf{r})|^2 \quad (\text{with}\ \ i,j = S,A). \tag{7.9}$$

The first term in the Hamiltonian (7.5) describes the local interaction within the two wells. The second term corresponds to the tunneling of particles from one well to the other. The last term takes additional two-particle processes like two-particle tunneling into account [88]. We verified by simulation that with our experimental parameter this term is small compared with other two terms (less than $10^{-4}E_j/N$ and $10^{-2}Ec/8$ for barrier height $V_b \simeq 0$, and less than $10^{-7}E_j/N$ and $10^{-12}Ec/8$ for high barrier height). We thus will neglected it for the following discussions.

We calculate numerically the two basis for the two-mode model, i.e. the stationary solution of Gross-Pitaevskii equation $\phi_S(\mathbf{r})$ and $\phi_A(\mathbf{r})$ in Eq.(7.4)

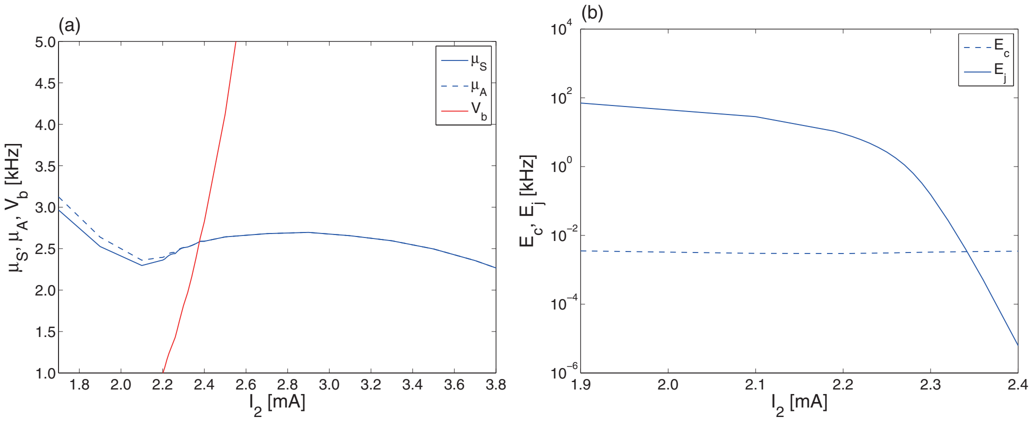

Figure 7.2: (a) Chemical potential for the symmetric and antisymmetric state (blue) and the height of the barrier (red) versus the current I_2. (b) The Josephson coupling energy E_j and the charging energy E_c versus the current I_2. The total atom number $N = 1300$. The scattering length $a = 100\, r_\mathrm{B}$, where r_B is the Bohr radius. The 3D double well trap configuration is given by another simulation developed for the atom chip by the experimentalists.

in 3D, by using the conjugate gradient method (see appendix D). In experiment, the trap is deformed into a double well within a time τ_r by changing the wire current I_2 on the chip. In the simulation, we calculate $\phi_S(\mathbf{r})$ and $\phi_A(\mathbf{r})$ for each trap configuration corresponding to a given I_2 (20 points) with the ^{87}Rb atoms in state $|F = 2, m_F = 2\rangle$. Since I_2 depends on time (see Eq.(7.10) and (7.11) in the next subsection), finally E_j and E_c can be interpolated as a function of time.

In Fig.7.2 (a) we plot the chemical potential for the ground state (symmetric) and first excitation state (antisymmetric) as a function of the current I_2 for 1300 atoms. The height of the barrier V_b is also plotted for comparison. μ_A approaches μ_S, and V_b exceeds the chemical potential when the current is about 2.3 mA. In Fig.7.2 (b) we show the Josephson coupling energy E_j and the charging energy E_c versus the current. For a 1300 atom BEC, E_c is typically 3.5 Hz, weakly dependent on the barrier height, and E_j is about 100 kHz for the barrier $V_b \simeq 0$. There is an exponential decay of E_j after the current reaches about 2.25 mA, which corresponds to $V_b \simeq 1.3$ kHz. When the current is larger than 2.5 mA, the barrier is much higher than the chemical potential, and E_j almost vanishes.

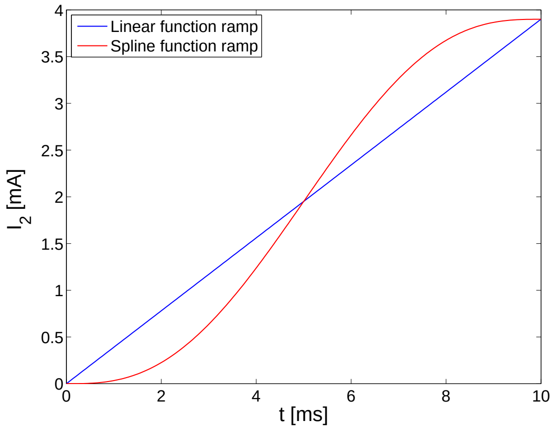

Figure 7.3: The current used for raising the barrier as a function of time. Blue line: linear function ramp. Red line: spline function ramp. The total ramping time $\tau_r = 10\,\text{ms}$.

7.2.2 Dynamical evolution: influence of the barrier ramping time

The barrier is raised by continuously increasing the current I_2 from 0 to 3.9 mA, corresponding to a barrier height well above the chemical potential, see Fig.7.2 (a). The current ramp as a function of time is shown in Fig.7.3, where two ramping schemes are plotted: a linear function ramp

$$I_2(t) = \left(\frac{t}{\tau_r}\right) I^{\text{final}} \tag{7.10}$$

and a spline function ramp with zero derivative at initial and final times

$$I_2(t) = \left[6\left(\frac{t}{\tau_r}\right)^5 - 15\left(\frac{t}{\tau_r}\right)^4 + 10\left(\frac{t}{\tau_r}\right)^3\right] I^{\text{final}} \tag{7.11}$$

where τ_r is total ramping time, and the final current $I^{\text{final}} = 3.9\,\text{mA}$.

We perform a dynamical simulation with the two-mode model Hamiltonian (7.5), where the two relevant parameters E_c and E_j are obtained by solving the 3D Gross-Pitaevskii equation for the experimental trap with different I_2 [85]. In the simulations, the initial state is described by a thermal density matrix,

$$\rho(t_0) \sim \exp\left[-\epsilon_j(t_0)/k_B T\right] |j\rangle\langle j| \,, \tag{7.12}$$

where $\epsilon_j(t_0)$ is the eigenvalue of the Hamiltonian (7.5) at time t_0, and $|j\rangle$ is

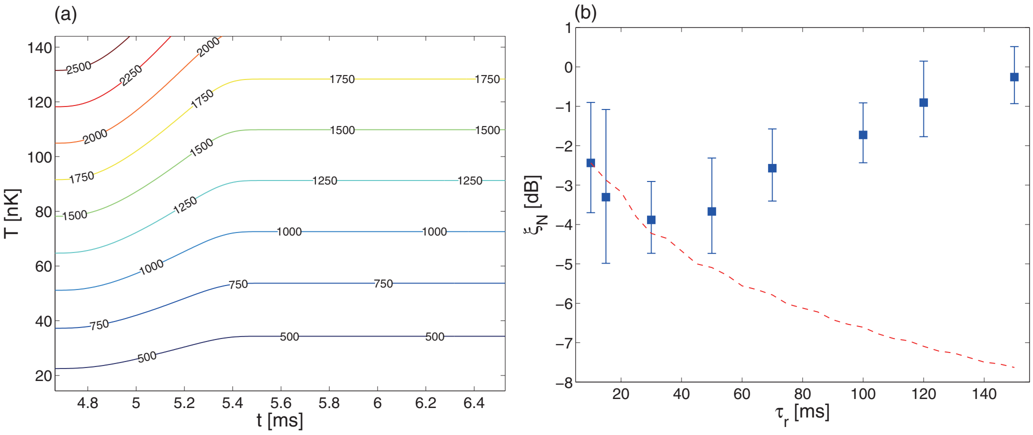

Figure 7.4: (a) Contour plot of the variance of the relative atom number calculated from Eq.(7.14). Spline function ramp with the total ramp time $\tau_r = 10\,\text{ms}$. The initial temperature is varied from 20 nK to 140 nK. (b) Measured (blue squares)and calculated (red dashed line) number squeezing factor ξ_N as a function of ramping time τ_r of the barrier. The initial temperature for the two-mode calculation is 53 nK, fit with the experiment data for $\tau_r = 10\,\text{ms}$. The total number of atoms $N = 1300$.

the corresponding eigenstate[1], T is the temperature, and k_B is the Boltzmann constant. Then the state evolves according to the Von Neumann equation up to the end of the ramp,

$$i\hbar\frac{d\rho}{dt} = [\mathcal{H}, \rho] \tag{7.13}$$

The variance of the relative atom number between the two wells can be calculated as

$$\text{Var}\,(N_l - N_r)(t) = \text{Tr}\,[\,\rho(t)(N_l - N_r)^2\,] \tag{7.14}$$

where we have assumed that the two wells are symmetric such that the average of the relative atom number between the two wells is zero.

During the splitting the dynamics is initially adiabatic: the population of each eigenstate $|j\rangle$ does not change, i.e. the entropy of the system is conserved, which results in effective cooling [42]. The system is expected to remain adiabatic if the barrier is raised slowly enough compared with the time scale needed by the atoms to tunnel from one well to another [89], which is approximately proportional to $1/\sqrt{E_c E_j}$. The adiabaticity will break down at a large separation of the two condensates, in the very weak tunneling regime when E_j approaches to zero, resulting in a frozen value of $\text{Var}(N_l -$

---

[1] ϵ_j can be obtained by diagonalizing the Hamiltonian (7.5) in the Fock basis.

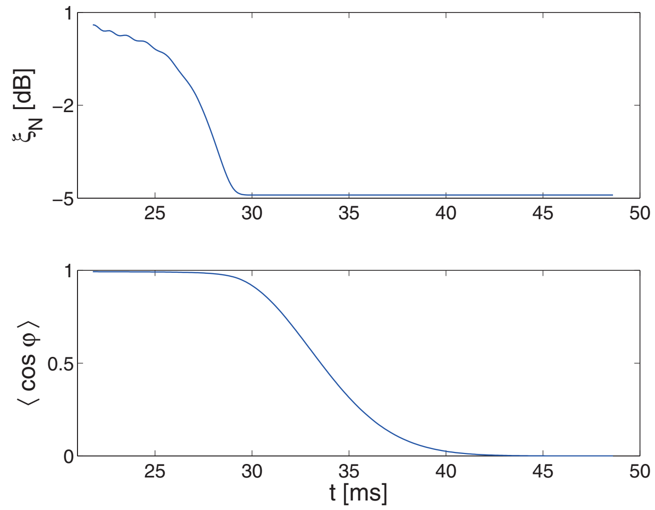

Figure 7.5: The number squeezing factor ξ_N and phase coherence as a function of time during the splitting using linear ramp described by Eq.(7.10). The total ramp time $\tau_r = 50\,\mathrm{ms}$, and the number of atoms $N = 1300$.

N_r). The time at which the adiabaticity breaks down depends on the ramping time τ_r, the parameters E_c and E_j, and the initial condition $\rho(t_0)$ [89]. In Fig.7.4 (a) we show the variance of the relative atom number as a function of time for different initial temperature T calculated evolving the density matrix $\rho(t)$ with Eq.(7.13). A spline function ramp sequence (7.11) is chosen with a fixed total ramp time $\tau_r = 10\,\mathrm{ms}$.

Comparing Var $(N_l - N_r)$ at the end of the ramp obtained from our calculation with the experiment data with the same τ_r, we find that an initial temperature of $53\,\mathrm{nK}$ at $t_0 = 4.66\,\mathrm{ms}$ reproduces the measured fluctuations for $\tau_r = 10\,\mathrm{ms}$. We then use this temperature as the initial condition for the other ramps $\tau_r = 20 \sim 150\,\mathrm{ms}$. By varying the ramp time τ_r we obtain the number squeezing factor

$$\xi_N^2(\tau_r) = \frac{\mathrm{Var}(N_l - N_r)(\tau_r)}{N} \tag{7.15}$$

as shown in Fig.7.4 (b). For short ramp time (up to 50 ms ramp), the fluctuation of the atom number obtained from our simulation (red dashed line) are consistent with the experiment measurement (blue squares). However, for longer ramp time, the fluctuations increase with τ_r in experiment. Experimentalists think that this is due to technical heating of the BEC, which is not included in the two-mode model simulations.

In another experiment, the atoms are split by ramping I_2 linearly, as shown in Eq.(7.10), with a fixed ramping time 50 ms. At low temperature

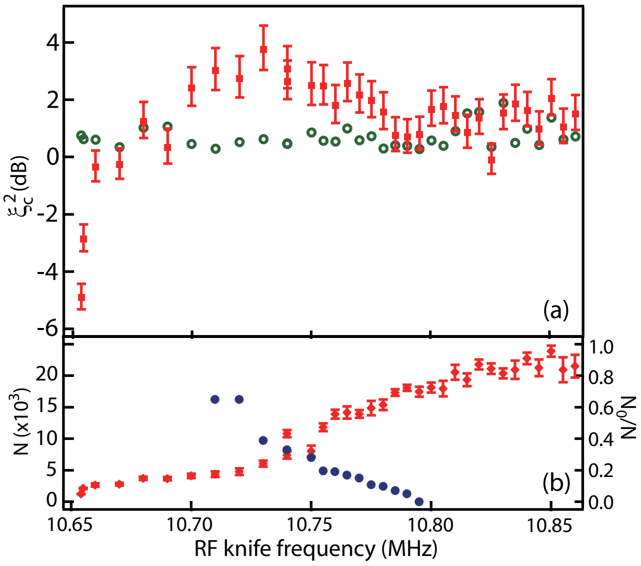

Figure 7.6: (a) Effect of the temperature on the number squeezing. The final frequency of the RF ramp of evaporative cooling is varied before splitting the cloud. Red squares: number squeezing factor. Green circles: estimated atomic shot-noise level which takes into account technical noise. (b) Total atom number N (red diamonds) and condensed fraction N_0/N prior to the splitting (blue circles).

when most of the atoms are in the condensate, the best measured number squeezing factor is $\xi_N = -4.9\,\text{dB}$. Using our two-mode model calculation, in Fig.7.5 (a), we plot the number squeezing factor ξ_N as a function of time. According to the figures, $\text{Var}(N_l - N_r)$ does not evolve anymore after 30 ms. In Fig.7.5 (b), we show the phase coherence as a function of time,

$$\langle \cos\varphi \rangle (t) = \frac{2\langle S_x(t) \rangle}{N} \tag{7.16}$$

where φ is the relative phase between the two modes. At $t \simeq 30\,\text{ms}$, the phase coherence is $\langle \cos\varphi \rangle \sim 0.93$, implying that this is a spin squeezed state which can be used to get a possible metrology gain of -4.4 dB below the standard quantum limit. However at the end of the 50 ms ramp, the phase coherence approaches to zero. This is due to the nonlinearity introduced by the atomic interactions that makes the relative phase collapse.

For 1300 atoms, the thermal fraction is so small that it is very difficult to measured the temperature with the standard time-of-flight expansion method in the experiment. It is proposed in [90] that in this case, the temperature of the system can be deduced from the variance of the relative phase if the parameters of the system, E_j and E_c, are known. Here we obtain the temperature from the variance of the relative atom number. To check the validity of this method for our system, we compare the deduced temperature directly with the experiment data for larger number of atoms. By changing the final frequency of the evaporate cooling ramp, the smallest thermal fraction that could be measured in the experiment is 0.65, for a total number of atoms $N \simeq 4.3 \times 10^3$ (see Fig.7.6 (b)). The corresponding temperature deduced by using the ideal Bose formula is 460 nK. In order to compare this measured temperature with our model, we have to "improve it" including the fluctuations of the thermal fractions. To this aim, here we assume that only condensate contributes to the squeezing, while thermal atoms always have shot noise fluctuations:

$$\mathrm{Var}\,(N_l - N_r) = \mathrm{Var}\,(N_l - N_r)_{\mathrm{BEC}} + N_{\mathrm{th}} \tag{7.17}$$

where N_{th} is the number of thermal atoms. We then calculate the total squeezing factor

$$\xi_N^2 = \xi_{N_0}^2 \frac{N_0}{N} + \frac{N - N_0}{N} \tag{7.18}$$

as a function of initial temperature, where N_0 is the number of atoms in the condensate. We then compare ξ_N^2 with the experiment result, and find $T \simeq 470$ nK, which is in good agreement with the result obtained from condensed fraction measurements.

7.3 Thermal equilibrium multi-mode approach

In the experiment, finite temperature plays a very important role in the fluctuations of the atom number difference $N_l - N_r$. As shown in Fig.7.6, well below the critical temperature T_c, reduced fluctuations down to -4.9 dB below the shot-noise level is observed. Fluctuations rise to more than +3.8 dB below to T_c, before reaching the shot-noise level for higher temperatures. The observed sub- and super-Poinssonian fluctuations of the atom number difference $N_l - N_r$ indeed originate from the interplay between interactions and quantum statistics. To study the effect of finite temperature $T \gtrsim T_c$, the two-mode is no longer valid. In this section we study this problem in the grand canonical ensemble[2]. Although the trap used here is a three-dimensional harmonic potential instead of a double well potential, the result that we obtained is very similar to those in the double well. We will show that the peak of fluctuations for $T < T_c$ is in fact a general feature, which

---

[2] Since the signal we are interested in is the atom number difference between two wells, the non-physical fluctuations of the total number of condensate particles due to the use of grand canonical ensemble will not affect the results.

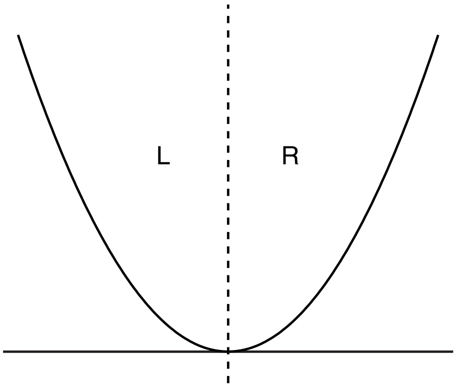

Figure 7.7: We consider fluctuations of the particle number difference $N_l - N_r$ between the left and the right halves of a three-dimensional harmonic potential.

already appears in a single harmonic well and, even more surprisingly, for an ideal gas.

In subsection 7.3.1 we address the ideal gas case for which we find the complete analytical solution in the grand canonical ensemble. In subsection 7.3.2 we give some physical interpretations of our result got for the ideal gas, and in the end of this subsection, we briefly discuss the interacting case. This part of work is published in [82], in which I carried out the analytical calculations for ideal gas.

7.3.1 Ideal gas: exact solution

We consider an ideal gas of bosons in a three-dimensional harmonic potential. The signal we are interested in is the particle number difference $N_l - N_r$ between the left and right halves of the harmonic potential along one direction, as shown in Fig.7.7. In terms of the atomic field operators:

$$N_l - N_r = \int_{\mathbf{r}\in L} \hat{\Psi}^\dagger(\mathbf{r})\hat{\Psi}(\mathbf{r}) - \int_{\mathbf{r}\in R} \hat{\Psi}^\dagger(\mathbf{r})\hat{\Psi}(\mathbf{r}) \tag{7.19}$$

Due to the symmetry of the problem, $N_l - N_r$ has a zero mean value. It is convenient to express its variance in terms of the unnormalized pair correlation function

$$g^{(2)}(\mathbf{r},\mathbf{r}') = \langle \hat{\Psi}^\dagger(\mathbf{r})\hat{\Psi}^\dagger(\mathbf{r}')\hat{\Psi}(\mathbf{r}')\hat{\Psi}(\mathbf{r}) \rangle \tag{7.20}$$

By using the bosonic commutation relation for the field operators, one has

$$\mathrm{Var}(N_l - N_r) = \langle N \rangle + 2\left[\int_{\mathbf{r}\in L}\int_{\mathbf{r}'\in L} g^{(2)}(\mathbf{r},\mathbf{r}') - \int_{\mathbf{r}\in L}\int_{\mathbf{r}'\in R} g^{(2)}(\mathbf{r},\mathbf{r}')\right] \tag{7.21}$$

We assume that the system is in thermal equilibrium in the grand canonical ensemble with $\beta = 1/k_B T$ the inverse temperature and μ the chemical potential. For an ideal gas, the density operator is Gaussian. We can then use Wick's theorem and express $g^{(2)}(\mathbf{r}, \mathbf{r}')$ in terms of the first-order coherence function $g^{(1)}(\mathbf{r}, \mathbf{r}') = \langle \hat{\Psi}^\dagger(\mathbf{r})\hat{\Psi}(\mathbf{r}')\rangle$:

$$g^{(2)}(\mathbf{r}, \mathbf{r}') = g^{(1)}(\mathbf{r}, \mathbf{r}')g^{(1)}(\mathbf{r}', \mathbf{r}) + g^{(1)}(\mathbf{r}, \mathbf{r})g^{(1)}(\mathbf{r}', \mathbf{r}') \tag{7.22}$$

The $g^{(1)}(\mathbf{r}, \mathbf{r}')$ is a matrix element of the one-body density operator

$$g^{(1)}(\mathbf{r}, \mathbf{r}') = \langle \mathbf{r}'|\frac{1}{z^{-1}e^{\beta h_1} - 1}|\mathbf{r}\rangle \tag{7.23}$$

where h_1 is the one-particle Hamiltonian

$$h_1 = \frac{\mathbf{p}^2}{2M} + \sum_{\alpha=x,y,z} \frac{1}{2}M\omega_\alpha^2 r_\alpha^2 \,. \tag{7.24}$$

To compute $g^{(1)}$, it is convenient to expand the one-body density operator in powers of the fugacity $z = e^{\beta\mu}$ [25]:

$$g^{(1)}(\mathbf{r}, \mathbf{r}') = \langle \mathbf{r}'|\sum_{l=1}^{\infty} z^l e^{-l\beta h_1}|\mathbf{r}\rangle \tag{7.25}$$

On the other hand for a harmonic potential the matrix elements of $e^{-\beta h_1}$ are know [91]. We then have

$$\begin{aligned} g^{(1)}(\mathbf{r}, \mathbf{r}') = \sum_{l=1}^{\infty} z^l \left(\frac{M\bar{\omega}}{2\pi\hbar}\right)^{3/2} \prod_{\alpha=x,y,z} \left[\sinh\left(l\eta_\alpha\right)\right]^{-1/2} \exp\left\{-\frac{M\omega_\alpha}{4\hbar}\right. \\ \left. \cdot \left[(r_\alpha + r'_\alpha)^2 \tanh\left(\frac{l\eta_\alpha}{2}\right) + (r_\alpha - r'_\alpha)^2 \coth\left(\frac{l\eta_\alpha}{2}\right)\right]\right\} \end{aligned} \tag{7.26}$$

where we introduce the geometrical mean of the oscillation frequencies $\bar{\omega} = (\omega_x\omega_y\omega_z)^{1/3}$ and

$$\eta_\alpha = \beta\hbar\omega_\alpha \,. \tag{7.27}$$

It is convenient to renormalize the fugacity introducing

$$\tilde{z} = z \exp\left(-\sum_\alpha \eta_\alpha/2\right) \tag{7.28}$$

that spans the interval $(0, 1)$. After some algebra (see appendix E), the variance of $N_l - N_r$ is expressed as a double sum that we reorder as

$$\mathrm{Var}\,(N_l - N_r) = \langle N\rangle + \sum_{s=1}^{\infty} c_s \tilde{z}^s \tag{7.29}$$

and

$$c_s = \sum_{l=1}^{s-1} \frac{1 - \frac{4}{\pi}\arctan\sqrt{\tanh\left(\frac{1}{2}l\eta_x\right)\tanh\left[\frac{1}{2}(s-l)\eta_x\right]}}{\prod\limits_{\alpha=x,y,z}\left[1 - e^{-\eta_\alpha s}\right]} \tag{7.30}$$

with $c_1 = 0$. Correspondingly, the mean atom number is expressed as

$$\begin{aligned} \langle N\rangle &= \int d^3r\, g^{(1)}(\mathbf{r}, \mathbf{r}') \\ &= \sum_{l=1}^{\infty} \tilde{z}^l \prod_{\alpha=x,y,z} \left[e^{-l\eta_\alpha}\sinh\left(l\eta_\alpha\right)\right]^{-1/2}\left[8\coth\left(\frac{l\eta_\alpha}{2}\right)\right]^{1/2} \\ &= \sum_{l=1}^{\infty} \tilde{z}^l \prod_{\alpha=x,y,z} \frac{1+\coth(l\eta_\alpha/2)}{2} \end{aligned} \tag{7.31}$$

This constitutes our analytical solution of the problem in the grand canonical ensemble. In Fig.7.8 we show an example of fluctuation of the particle number difference for realistic parameters of an atom-chip experiment. In the following, we perform some approximations or transformations in order to obtain explicit formulas and get some physical insight. We consider the limit of a large atom number and a high temperature $k_BT \gg \hbar\omega_\alpha$ for all α. We will give the approximated result in two different regimes: Non-condensed regime and Bose-condensed regime.

Non-condensed regime

Taking the limit $\eta_\alpha \ll 1$ in Eq.(7.31) we get

$$\langle N\rangle \simeq \left(\frac{k_BT}{\hbar\bar{\omega}}\right)^3 g_3(\tilde{z}) \tag{7.32}$$

where $g_\alpha(z) = \sum_{l=1}^{\infty} z^l/l^\alpha$ is the Bose function. From this equation we recover the usual definition of the critical temperature T_c:

$$k_BT_c = \left[\frac{N}{\zeta(3)}\right]^{1/3}\hbar\bar{\omega}\,, \tag{7.33}$$

where $\zeta(3) = g_3(1)$ with ζ the Riemann function. Taking the same limit in (7.29) gives

$$\mathrm{Var}(N_l - N_r) \simeq \langle N\rangle\left[1 + \frac{g_2(\tilde{z}) - g_3(\tilde{z})}{\zeta(3)}\frac{T^3}{T_c^3}\right]\,. \tag{7.34}$$

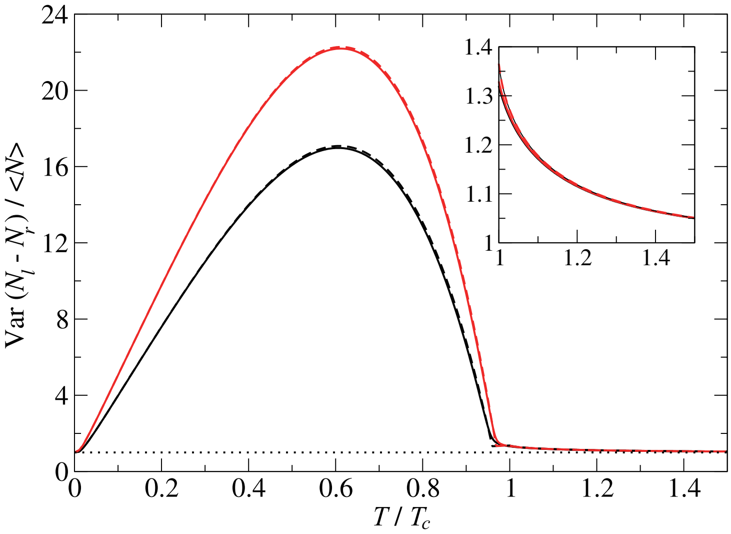

Figure 7.8: Normalized variance of the particle number difference $N_l - N_r$ as a function of temperature in a cigar-shaped trap with $\omega_y = \omega_z = 2\omega_x$. The number of particles is $\langle N\rangle = 6000$ (black lines) and $\langle N\rangle = 13000$ (red lines). The inset is a magnification of the $T > T_c$ region. Solid lines: exact result (7.29) together with (7.31). Dashed line for $T > T_c$: approximate result (7.34) together with (7.32). Dashed line for $T < T_c$: approximate result resulting from the improved estimates (7.47) and (7.48). The temperature T is expressed in units of the critical temperature T_c defined in Eq.(7.33).

At $T = T_c$ this leads to

$$\mathrm{Var}(N_l - N_r)(T_c) \simeq \langle N\rangle \frac{\zeta(2)}{\zeta(3)} \simeq 1.37\langle N\rangle \tag{7.35}$$

showing that the non-condensed gas is weakly super-Poissonian, as already observed in Fig.7.8. Alternatively, one may directly take the limit $\eta_\alpha \to 0$ in Eq.(7.26), yielding

$$g^{(1)}(\mathbf{r}, \mathbf{r}') = \sum_{l=1}^{\infty} \frac{z^l}{l^{3/2}\lambda_{dB}^3} \prod_{\alpha=x,y,z} \exp\left[-\frac{lM\omega_\alpha^2}{2k_BT}\left(\frac{r_\alpha + r'_\alpha}{2}\right)^2 - \frac{\pi}{l\lambda_{dB}^2}\left(r_\alpha - r'_\alpha\right)^2\right]. \tag{7.36}$$

This semiclassical approximation coincides with the widely used local density approximation, in which one can replace the chemical potential $\mu = \ln z/\beta$ in the $g^{(1)}$ function for a spatially uniform condensate

$$g^{(1)}(\mathbf{r}, \mathbf{r}') = \sum_{l=1}^{\infty} \frac{z^l}{l^{3/2}\lambda_{dB}^3} \prod_{\alpha=x,y,z} \exp\left[-\frac{\pi}{l\lambda_{dB}^2}\left(r_\alpha - r'_\alpha\right)^2\right] \tag{7.37}$$

by $\mu - U(\mathbf{r})$, where $U(\mathbf{r})$ is the $\mathbf{r}$ dependent external potential. By using Eq.(7.36), one recovers (7.32) and (7.33).

Bose-condensed regime

In this degenerate regime $\tilde{z} \to 1$, therefore the series (7.29) and (7.31) converge very slowly. In particular, when $\tilde{z} = 1$ summation diverges. A useful exact rewriting is obtained by pulling out the asymptotic behaviors of the summands. For Eq.(7.29),

$$\mathrm{Var}\,(N_l - N_r) = \langle N \rangle + c_\infty \langle N_0 \rangle + \sum_{s=1}^{\infty} (c_s - c_\infty) \tilde{z}^s \tag{7.38}$$

where

$$c_\infty = \lim_{s\to\infty} c_s = 2 \sum_{l=1}^{\infty} \left[1 - \frac{4}{\pi} \arctan \sqrt{\tanh\left(\frac{l\eta_x}{2}\right)} \right] \tag{7.39}$$

obtained by using

$$\lim_{s\to\infty} \sum_{l=1}^{s-1} = \lim_{s\to\infty} \sum_{l=1}^{s/2-1} + \lim_{s\to\infty} \sum_{l=s/2}^{s-1}, \tag{7.40}$$

and $\langle N_0 \rangle = \tilde{z}/(1-\tilde{z})$ is the mean number of condensate particles. The mean atom number is rewritten as

$$\langle N \rangle = \langle N_0 \rangle + \sum_{l=1}^{\infty} \tilde{z}^l \left[-1 + \prod_{\alpha=x,y,z} \frac{1 + \coth\left(l\eta_\alpha/2\right)}{2} \right]. \tag{7.41}$$

Taking the limit $\eta_\alpha \to 0$ in each term of the sum over l in (7.41), and taking the first order of η_α in the expansion, we obtain the usual condensate fraction

$$\frac{\langle N_0 \rangle}{\langle N \rangle} \simeq 1 - \frac{T^3}{T_c^3} \tag{7.42}$$

where we have used the critical temperature defined in (7.33). The same procedure may be applied to the sum over s in (7.38). The calculation of the small-η limit of c_∞ requires a different technique: Contrarily to the previous case, the sum in (7.39) is not dominated by values of the summation index $l \ll 1/\eta_\alpha$ and explores high values of $l \sim 1/\eta_x$. As a remarkable consequence, the local-density approximation fails in this case. We find that one rather has to replace the sum over l by an integral in (7.39):

$$c_\infty \simeq \int_0^{+\infty} dl \left[2 - \frac{8}{\pi} \arctan \sqrt{\tanh\left(\frac{l\eta_x}{2}\right)} \right] = \frac{2\ln 2}{\eta_x} \tag{7.43}$$

This leads to the dimple formula for $T < T_c$:

$$\mathrm{Var}\,(N_l - N_r) \simeq \langle N\rangle \left[1 + \frac{\zeta(2)-\zeta(3)}{\zeta(3)}\frac{T^3}{T_c^3} + 2\ln 2\left(\frac{k_B T_c}{\hbar\bar{\omega}}\right)\frac{T}{T_c}\left(1-\frac{T^3}{T_c^3}\right)\right] \tag{7.44}$$

where we have used expression (7.42) for $\langle N_0\rangle$. Comparing with Eq.(7.34) we find that the last term in Eq.(7.44) is a new contribution involving the macroscopic value of $\langle N_0\rangle$ below in critical temperature. Since $k_B T_c \gg \hbar\omega_x$ here, it is the dominant contribution to the fluctuations of the particle number difference. It clearly leads to the occurrence of a maximum of these fluctuations, at a temperature which remarkably is independent of the trap anisotropy:

$$\left(\frac{T}{T_c}\right)_{\max} \simeq 2^{-2/3} \simeq 0.63\,. \tag{7.45}$$

The corresponding variance is strongly super-Poissonian in the large atom-number limit:

$$[\mathrm{Var}\,(N_l - N_r)]_{\max} \simeq \langle N\rangle \left[1 + \frac{3}{4}\ln 2\left(\frac{2\langle N\rangle}{\zeta(3)}\right)^{1/3}\frac{\bar{\omega}}{\omega_x}\right]\,. \tag{7.46}$$

For the parameters of the upper curve in Fig.7.8, these approximate formulas lead to a maximal variance over $\langle N\rangle$ equal to $\simeq 27.5$, whereas the exact result is $\simeq 22.2$, located at $T/T_c \simeq 0.61$. We thus see that finite size corrections remain important even for the large atom number $\langle N\rangle = 13000$. Fortunately, it is straightforward to calculate the next order correction. For the condensate atom number, we simply expand the summand in (7.41) up to the next order, we recover the known result [92]:

$$\frac{\langle N_0\rangle}{\langle N\rangle} \simeq 1 - \frac{T^3}{T_c^3} - \frac{T^2}{T_c^2}\frac{3\zeta(2)}{2\zeta(3)}\frac{\hbar\omega_m}{k_B T_c} \tag{7.47}$$

with the arithmetic mean $\omega_m = \sum_\alpha \omega_\alpha/3$. For c_∞ we use the Euler-Mac Laurin summation formula, applied to the previously integrated function in (7.43) over the interval $(1, +\infty)$, and we obtain

$$c_\infty = \frac{2\ln 2}{\eta_x} - 1 + A\eta_x^{1/2} + O\left(\eta_x^{3/2}\right) \tag{7.48}$$

with $A = -2^{5/2}\zeta(-1/2)/\pi \simeq 0.374$ [82]. Using these more accurate formulas for $\langle N_0\rangle$ and c_∞ in the second term of the right-hand side of (7.39) leads to an excellent agreement with the exact result, see the dashed lines in Fig.7.8 practically indistinguishable from the solid lines. Not that the effect of the -1 correction in (7.48) is to change the shot noise term 1 in the square brackets (7.44) and (7.46) into $1 - \langle N_0\rangle/\langle N\rangle$.

7.3.2 A brief physical analysis

Here we make a brief analysis of the result obtained in the previous subsection. I refer to [82] for more detailed calculations. To investigate the contribution of different physical effects on our observable, one can split the field operator into the condensate and the non-condensed part,

$$\hat{\Psi}(\mathbf{r}) = \phi(\mathbf{r})a_0 + \delta\hat{\Psi}(\mathbf{r})\,, \tag{7.49}$$

where $\phi(\mathbf{r})$ is the ground mode wave function of the harmonic potential. Then the correlation function $g^{(2)}$ can be expressed in terms of three contributions: one originates from the condensate mode, one originates from the non-condensed gas only, and the other originates from a beating between the condensate and the non-condensed fields.

It is found that the first two terms have very limited contributions to $\mathrm{Var}(N_l - N_r)$. Indeed in equilibrium, the first term gives no contribution, and the non-condensed gas makes the fluctuations of $N_l - N_r$ weakly super-Poissonian when $T = T_c$. On the other hand, below T_c, the third term has an important contribution. The variance originated from this term can be finally written as

$$\mathrm{Var}(N_l - N_r)_{\mathrm{bt}} \simeq \langle N_0\rangle c_\infty\,. \tag{7.50}$$

This gives a physical meaning to the mathematical splitting (7.38) for $T < T_c$: the second term and the sum over s in the right-hand side of Eq.(7.38) respectively correspond to the condensate-non-condensed beating contribution and to the purely non-condensed contribution.

Note that the obtained super-Poissonian behavior has a close quantum optics analogue: the measurement of the fluctuation can be seen in a pictorial way as a balanced homodyne detection of the non-condensed field where the condensate field acts as a local oscillator. Since one or the other of these two fields vanishes for T tending to 0 or T_c, the beating effect, and thus $\mathrm{Var}(N_l - N_r)$, are obviously maximal at some intermediate temperature. On the other hand, in the regime where only one kind of field is present: for the coherent Bose condensate without interactions ($T \ll T_c$), as well as for thermal particles ($T \gg T_c$), Poissonian fluctuations are expected. The weakly super-Poissonian fluctuations originated from non-condensed particles (7.35) for $T \to T_c$ are analogous to the bunching effect in quantum optics.

Now we consider the interacting case. For the condensate, it is expected that the fluctuations of $N_l - N_r$ are sub-Poissonian instead of Poissonian due to the atomic interactions. When T approaches T_c from the side of low temperature, the appearance of the thermal fraction would greatly enhance the fluctuation. However due to interactions which tends to lower the fluctuations, the enhancement is not as large as in the case of without interactions.

And this is confirmed by the classical field simulations in [82]. Another difference with respect to the non-interacting case is that under the Thomas-Fermi approximation, we find very weak dependence of the enhancement of $[\mathrm{Var}(N_l - N_r)]_{\mathrm{max}}$ on the atom number, scaling as $\langle N \rangle^{-1/15}$.

Chapter 8

Conclusions and outlook

In this thesis, we studied theoretically realistic schemes for the production of spin squeezed states in Bose-Einstein condensates. These states are multi-particle entangled states that have practical interest in atomic interferometry, and in high precision spectroscopy. As it was proposed in the literature, a large amount of spin squeezing can be obtained by coherent interactions between cold atoms in a bimodal BEC. In real experiments, this scheme however will be limited by the effect of decoherence given by particle losses, and also by the spatial dynamics of the condensate wave functions.

Using an analytical Monte-Carlo wave functions approach, we obtained the maximum spin squeezing reachable in presence of decoherence (losses) unavoidably accompanying the elastic interactions among atoms. Our calculations showed how squeezing is degraded by this effect of decoherence: during the evolution each loss event causes an random phase shift between the two BEC components that depends on the kind of the loss event and on the time at which the loss takes place, which in the end degrades the squeezing. We also found that the effect of losses cannot be neglected as soon as the lost fraction of particles is of the order of the squeezing parameter. The more squeezed the state is, the more sensitive to the losses. The analytical solution that we found also allows us to perform an optimization for the spin squeezing. Once the experimental parameters are optimized, the best squeezing is obtained for an atom number $N \to \infty$ and not for a finite value of N, which is important for applications such as spectroscopy where large number of atoms will be favorable.

On the other hand, we developed a method to study the entangled spatial and spin dynamics of interacting bimodal BEC, which allows a full analytical treatment in some cases and can be used in the general case to investigate *a priori* complicated situations in 3D without the need of heavy numerics. Our treatment also gave a physical insight into the effect of spatial dynamics: the oscillations of the squeezing parameter during the evolution indeed originate from the excitations of hydrodynamics modes in the condensates, which have different frequencies depending on the number of atoms in the two BEC components. We showed that disentanglement of the spin and the spatial dynamics occurs at particular times and the spin squeezing at these points can be predicted by a simple two-mode model.

These studies give a more complete description of the scheme of achieving spin squeezing using interactions in a realistic situations on the one hand, and enabled us to compare the theoretical predictions with the spin squeezing achievable in experiment on the other hand. As an application, we considered two spin squeezing schemes: overlapping Na condensates or Rb condensates with the scattering length tuned by Feshbach resonance, and Rb condensates spatially separated with state-dependent potentials. We found more than $-10\,\mathrm{dB}$ squeezing can be obtained, despite of particle losses and spatial dynamics.

During our thesis, spin squeezing relying on atomic interactions has been demonstrated experimentally in both schemes that we have considered. We participated to one of them, realizing the spin squeezed state with state-dependent potentials on an atom chip. In experiment, with 1250 ± 45 Rb atoms, $-2.5\pm0.6\,\mathrm{dB}$ spin squeezing was achieved. The data show good agreement with our theoretical model which also takes into account the technical imperfections in the experiment.

In parallel, we studied the spin squeezing in a related but different system of a BEC with two external modes coherently coupled by the tunnel effect. Our study corresponds to the experiment of splitting a gas of ultracold ^{87}Rb atoms in a double-well potential created on an atom chip. In the low temperature regime ($T \ll T_c$), the observed reduction in spin noise in the experiment is $-4.9\,\mathrm{dB}$. By using a two-mode model, we predicted that $-4.4\,\mathrm{dB}$ spin squeezing, combining noise reduction and phase coherence, can be achieved. In the regime across T_c, we study the occurrence of important super-Poissonian fluctuations, which are also observed in experiment. With a thermal equilibrium approach in a grand canonical ensemble, we found that the fluctuations are weakly super-Poissonian for $T > T_c$. And if one lowers the temperature from T_c down to zeros, fluctuations increase, reach a maximum, and then decrease again as the non-condensed fraction vanishes.

To go further in the future, it would be interesting to use these non-classical states to improve the precision of quantum metrology. Using non-condensed atoms, an atomic clock improved by spin squeezed input state beyond the projection noise limit has been demonstrated experimentally [60, 37]. The interrogation time in those experiments goes from dozens to hundreds of μs. In [41], it is also demonstrated that an atomic interferometer with an accuracy exceeding the normal quantum limit for unentangled atoms can be achieved with the spin squeezed state created in BEC. Our theoretical calculations show that, by transferring the atoms into a shallow trap, the spin squeezed states created in [40] can survive more than 0.5 second under the influence of particle losses, which implies that an atomic clock beyond the standard quantum limit is reachable with these states. In this case we found that the main limit imposed to the life time of squeezing is the high two-body losses in $F = 2$ state. Suppressing this effect would be helpful to keep the squeezing.

On the other hand, when larger number of atoms is used in the spectroscopy, more attentions should be paid to spatial dynamics, as the sudden change in the mean-field after the mixing pulse will become larger. Nevertheless, at the time when spatial and spin dynamics disentangle, large amount of spin squeezing unaffected by spatial dynamics can still be obtained.

There also remain some open questions in this scheme. For example, in addition to losses of particles, which we have already studied, there is another source of decoherence inevitable in an experiment of cold atoms, the effect of finite temperature. Recently we are generalizing our study of spin squeezing in a Bose-Einstein condensate to a non-zero temperature, i.e. when several atomic modes of the field are initially occupied. By using Bogoliubov theory in [71], it was shown that within the order of $\sqrt{\delta N/N}$ (where δN is the number of non-condensed particles), the spin squeezing obtainable are independent of the temperature of the condensate. However, with the modulus-phase approach, we can take into account higher order corrections with the same approach. As we did in the case of loss of particles, the goal is to determine the ultimate limitation imposed by this source of decoherence.

Appendix A

Quantum averages related to squeezing parameter

In this appendix, we derive the expressions of ΔS_j^2 and Δ_{ij} $(i, j = x, y, z)$, which are needed to calculate the minimum variance of the spin component orthogonal to the mean spin $\Delta S_{\perp,\mathrm{min}}^2$ in Eq.(2.44). Using the collective spin operators, ΔS_j^2 and Δ_{ij} can be written as

$$\Delta S_j^2 = \langle S_j^2 \rangle - \langle S_j \rangle^2 \,, \tag{A.1}$$

$$\Delta_{ij} = \langle S_i S_j + S_j S_i \rangle - 2\langle S_i \rangle \langle S_j \rangle \,. \tag{A.2}$$

We then express $\langle S_j \rangle$, $\langle S_j^2 \rangle$ and $\langle S_i S_j \rangle$ in terms of the quantum averages of the field operators $\hat{\Psi}_a(\mathbf{r})$ and $\hat{\Psi}_b(\mathbf{r})$ (or the two-mode operators a and b). According to the definitions (4.13)-(4.15) and (2.28)-(2.30), the averages of the spin operators are given by

$$\langle S_x \rangle = \frac{1}{2} \int d^3r \, \langle \hat{\Psi}_b^\dagger(\mathbf{r}\,) \hat{\Psi}_a(\mathbf{r}\,) + \hat{\Psi}_a^\dagger(\mathbf{r}\,) \hat{\Psi}_b(\mathbf{r}\,) \rangle, \tag{A.3}$$

$$\langle S_y \rangle = \frac{i}{2} \int d^3r \, \langle \hat{\Psi}_b^\dagger(\mathbf{r}\,) \hat{\Psi}_a(\mathbf{r}\,) - \hat{\Psi}_a^\dagger(\mathbf{r}\,) \hat{\Psi}_b(\mathbf{r}\,) \rangle, \tag{A.4}$$

$$\langle S_z \rangle = \frac{1}{2} \int d^3r \, \langle \hat{\Psi}_a^\dagger(\mathbf{r}\,) \hat{\Psi}_a(\mathbf{r}\,) - \hat{\Psi}_b^\dagger(\mathbf{r}) \hat{\Psi}_b(\mathbf{r}) \rangle, \tag{A.5}$$

or

$$\langle S_x \rangle = \frac{1}{2} \langle b^\dagger a + a^\dagger b \rangle, \tag{A.6}$$

$$\langle S_y \rangle = \frac{i}{2} \langle b^\dagger a - a^\dagger b \rangle, \tag{A.7}$$

$$\langle S_z \rangle = \frac{1}{2} \langle a^\dagger a - b^\dagger b \rangle. \tag{A.8}$$

Using the bosonic commutation relations

$$[\hat{\Psi}_\varepsilon(\mathbf{r}), \hat{\Psi}^\dagger_{\varepsilon'}(\mathbf{r}')] = \delta_{\varepsilon\varepsilon'}\,\delta\left(\mathbf{r}-\mathbf{r}'\right)\ , \quad [\hat{\Psi}_\varepsilon(\mathbf{r}), \hat{\Psi}_{\varepsilon'}(\mathbf{r}')] = 0 \tag{A.9}$$

$$[a, a^\dagger] = 1\,, \quad [a,a] = [a,b] = [a,b^\dagger] = 0\,, \tag{A.10}$$

one obtains

$$\begin{aligned}
\langle S_x^2\rangle &= \frac{1}{2}\mathrm{Re}\int d^3r\, d^3r'\, \langle \hat{\Psi}^\dagger_b(\mathbf{r})\hat{\Psi}^\dagger_a(\mathbf{r}')\hat{\Psi}_a(\mathbf{r})\hat{\Psi}_b(\mathbf{r}') + \hat{\Psi}^\dagger_b(\mathbf{r})\hat{\Psi}^\dagger_b(\mathbf{r}')\hat{\Psi}_a(\mathbf{r})\hat{\Psi}_a(\mathbf{r}')\rangle \\
&\quad + \frac{1}{4}\int d^3r\, \langle \hat{\Psi}^\dagger_a(\mathbf{r})\hat{\Psi}_a(\mathbf{r}) + \hat{\Psi}^\dagger_b(\mathbf{r})\hat{\Psi}_b(\mathbf{r})\rangle\,, && \text{(A.11)}\\
\langle S_y^2\rangle &= \frac{1}{2}\mathrm{Re}\int d^3r\, d^3r'\, \langle \hat{\Psi}^\dagger_b(\mathbf{r})\hat{\Psi}^\dagger_a(\mathbf{r}')\hat{\Psi}_a(\mathbf{r})\hat{\Psi}_b(\mathbf{r}') - \hat{\Psi}^\dagger_b(\mathbf{r})\hat{\Psi}^\dagger_b(\mathbf{r}')\hat{\Psi}_a(\mathbf{r})\hat{\Psi}_a(\mathbf{r}')\rangle \\
&\quad + \frac{1}{4}\int d^3r\, \langle \hat{\Psi}^\dagger_a(\mathbf{r})\hat{\Psi}_a(\mathbf{r}) + \hat{\Psi}^\dagger_b(\mathbf{r})\hat{\Psi}_b(\mathbf{r})\rangle\,, && \text{(A.12)}\\
\langle S_z^2\rangle &= \frac{1}{4}\int d^3r\, d^3r'\, \langle \hat{\Psi}^\dagger_a(\mathbf{r})\hat{\Psi}^\dagger_a(\mathbf{r}')\hat{\Psi}_a(\mathbf{r})\hat{\Psi}_a(\mathbf{r}') + \hat{\Psi}^\dagger_b(\mathbf{r})\hat{\Psi}^\dagger_b(\mathbf{r}')\hat{\Psi}_b(\mathbf{r})\hat{\Psi}_b(\mathbf{r}')\rangle \\
&\quad - \frac{1}{2}\int d^3r\, d^3r'\, \langle \hat{\Psi}^\dagger_b(\mathbf{r})\hat{\Psi}^\dagger_a(\mathbf{r}')\hat{\Psi}_b(\mathbf{r})\hat{\Psi}_a(\mathbf{r}')\rangle \\
&\quad + \frac{1}{4}\int d^3r\, \langle \hat{\Psi}^\dagger_a(\mathbf{r})\hat{\Psi}_a(\mathbf{r}) + \hat{\Psi}^\dagger_b(\mathbf{r})\hat{\Psi}_b(\mathbf{r})\rangle\,, && \text{(A.13)}
\end{aligned}$$

or

$$\begin{aligned}
\langle S_x^2\rangle &= \frac{1}{2}\mathrm{Re}\langle b^\dagger a^\dagger ab + b^\dagger b^\dagger aa\rangle + \frac{1}{4}\langle a^\dagger a + b^\dagger b\rangle\,, && \text{(A.14)}\\
\langle S_y^2\rangle &= \frac{1}{2}\mathrm{Re}\langle b^\dagger a^\dagger ab - b^\dagger b^\dagger aa\rangle + \frac{1}{4}\langle a^\dagger a + b^\dagger b\rangle\,, && \text{(A.15)}\\
\langle S_z^2\rangle &= \frac{1}{4}\langle a^\dagger a^\dagger aa + b^\dagger b^\dagger bb\rangle - \frac{1}{2}\langle b^\dagger a^\dagger ab\rangle + \frac{1}{4}\langle a^\dagger a + b^\dagger b\rangle\,. && \text{(A.16)}
\end{aligned}$$

Similarly the quantum averages of operators $S_iS_j + S_jS_i$ can be written as

$$\begin{aligned}
\langle S_xS_y + S_yS_x\rangle &= -\mathrm{Im}\int d^3r\, d^3r'\, \langle \hat{\Psi}^\dagger_b(\mathbf{r})\hat{\Psi}^\dagger_b(\mathbf{r}')\hat{\Psi}_a(\mathbf{r})\hat{\Psi}_a(\mathbf{r}')\rangle\,, && \text{(A.17)}\\
\langle S_yS_z + S_zS_y\rangle &= \mathrm{Im}\int d^3r\, d^3r' \langle \hat{\Psi}^\dagger_a(\mathbf{r})\hat{\Psi}^\dagger_a(\mathbf{r}')\hat{\Psi}_a(\mathbf{r})\hat{\Psi}_b(\mathbf{r}') \\
&\qquad + \hat{\Psi}^\dagger_b(\mathbf{r})\hat{\Psi}^\dagger_b(\mathbf{r}')\hat{\Psi}_b(\mathbf{r})\hat{\Psi}_a(\mathbf{r}')\rangle\,, && \text{(A.18)}\\
\langle S_zS_x + S_xS_z\rangle &= \mathrm{Re}\int d^3r\, d^3r'\, \langle \hat{\Psi}^\dagger_a(\mathbf{r})\hat{\Psi}^\dagger_a(\mathbf{r}')\hat{\Psi}_a(\mathbf{r})\hat{\Psi}_b(\mathbf{r}') \\
&\qquad - \hat{\Psi}^\dagger_b(\mathbf{r})\hat{\Psi}^\dagger_b(\mathbf{r}')\hat{\Psi}_b(\mathbf{r})\hat{\Psi}_a(\mathbf{r}')\rangle\,, && \text{(A.19)}
\end{aligned}$$

or

$$\langle S_xS_y + S_yS_x\rangle = -\mathrm{Im}\langle b^\dagger b^\dagger aa\rangle\,, \tag{A.20}$$

$$\langle S_yS_z + S_zS_y\rangle = \mathrm{Im}\langle a^\dagger a^\dagger ab + b^\dagger b^\dagger ba\rangle\,, \tag{A.21}$$

$$\langle S_zS_x + S_xS_z\rangle = \mathrm{Re}\langle a^\dagger a^\dagger ab - b^\dagger b^\dagger ba\rangle\,. \tag{A.22}$$

Therefore to calculate the squeezing parameters, finally one needs to calculate ten quantum averages of the field operators as shown above, and nine of the two-mode operators since the space independent operator $b^\dagger a^\dagger ba$ is equivalent to $b^\dagger a^\dagger ab$. An example of these nine quantum averages is given by Eqs.(3.21)-(3.29) in chapter 3, where particle losses are taken into account. In particular, when there are no particle losses, the total number of atoms N is conserved. One then has

$$\int d^3r\,\langle\hat{\Psi}_a^\dagger(\mathbf{r})\hat{\Psi}_a(\mathbf{r})\rangle = \langle a^\dagger a\rangle = N|C_a|^2\,, \tag{A.23}$$

$$\int d^3r\,\langle\hat{\Psi}_b^\dagger(\mathbf{r})\hat{\Psi}_b(\mathbf{r})\rangle = \langle b^\dagger b\rangle = N|C_b|^2\,, \tag{A.24}$$

$$\int d^3r\,d^3r'\,\langle\hat{\Psi}_a^\dagger(\mathbf{r})\hat{\Psi}_a^\dagger(\mathbf{r}')\hat{\Psi}_a(\mathbf{r})\hat{\Psi}_a(\mathbf{r}')\rangle = \langle a^\dagger a^\dagger aa\rangle = N(N-1)|C_a|^4\,, \tag{A.25}$$

$$\int d^3r\,d^3r'\,\langle\hat{\Psi}_b^\dagger(\mathbf{r})\hat{\Psi}_b^\dagger(\mathbf{r}')\hat{\Psi}_b(\mathbf{r})\hat{\Psi}_b(\mathbf{r}')\rangle = \langle b^\dagger b^\dagger bb\rangle = N(N-1)|C_b|^4\,, \tag{A.26}$$

$$\int d^3r\,d^3r'\,\langle\hat{\Psi}_b^\dagger(\mathbf{r})\hat{\Psi}_a^\dagger(\mathbf{r}')\hat{\Psi}_b(\mathbf{r})\hat{\Psi}_a(\mathbf{r}')\rangle = \langle b^\dagger a^\dagger ab\rangle = N(N-1)|C_a|^2|C_b|^2\,. \tag{A.27}$$

In this case, the squeezing parameter can be obtained with five quantum averages of the field operators, as shown in Eqs.(4.18)-(4.22) after spatial integration, or four quantum averages of the two-mode operators, as shown in Eqs.(2.48)-(2.51).

Appendix B

Rotation of a state on the Bloch sphere

On the Bloch sphere, rotating a state $|\psi\rangle$ by an angle ϕ around an axis-j, where $j = x, y, z$, can be described by a unitary transformation

$$U_j = e^{-i\phi S_j} \tag{B.1}$$

where S_j is the collective spin operators defined in (2.28)-(2.30). The state after the rotation $|\psi'\rangle$, and the corresponding expectation value of spin components S_k $(k = x, y, z)$ can be written as follows,

$$|\psi'\rangle = e^{-i\phi S_j}|\psi\rangle \tag{B.2}$$

$$\langle\psi'|S_k|\psi'\rangle = \langle\psi|e^{i\phi S_j}\, S_k\, e^{-i\phi S_j}|\psi\rangle = \langle\psi|S'_k|\psi\rangle\,. \tag{B.3}$$

The measurement of S_k after the rotation is equivalent to the measurement of S'_k before the rotation. Let us define the ladder operators

$$S_{x\pm} = S_y \pm iS_z\,, \tag{B.4}$$

$$S_{y\pm} = S_z \pm iS_x\,, \tag{B.5}$$

$$S_{z\pm} = S_x \pm iS_y\,. \tag{B.6}$$

According to the commutation relations $[S_j, S_{j\pm}] = \pm S_{j\pm}$, one has

$$S_j^n S_{j\pm} = S^{n-1} S_{j\pm}(S_j \pm 1) = \cdots = S_{j\pm}\,(S_j \pm 1)^n\,. \tag{B.7}$$

We assume that $F(S_j)$ is a function of the operator S_j which can be expanded in series

$$F(S_j) = \sum_n \frac{F^{(n)}(0)}{n!}\, S_j^n \tag{B.8}$$

where $F^{(n)}(0)$ is the n-th order derivative of F in $S_j = 0$. By using Eq.(B.7), one finds

$$\exp\left[iF(S_j)\right] S_{j\pm} \exp\left[-iF(S_j)\right] = S_{j\pm} \exp\left[iF(S_j \pm 1) - iF(S_j)\right] \tag{B.9}$$

Choosing $F(S_j) = \phi S_j$, one concludes that

$$e^{i\phi S_j}\, S_{j\pm}\, e^{-i\phi S_j} = S_{j\pm}\, e^{\pm i\phi}\,. \tag{B.10}$$

Now we consider the unitary transformation (2.9) rewritten as follows,

$$U = e^{-i\theta S_y} e^{-i\phi S_z} e^{i\varphi S_y}\,. \tag{B.11}$$

Using Eq.(B.10), the measurement of the operator S_z after the transformation is equivalent to the measurement of the operator

$$\begin{aligned} U^\dagger S_z U = S_z' = S_x \left(\sin\varphi\cos\theta - \cos\varphi\cos\phi\sin\theta\right) + S_y \sin\phi\sin\theta \\ + S_z \left(\sin\varphi\cos\phi\sin\theta + \cos\varphi\cos\theta\right) \end{aligned} \tag{B.12}$$

where S_x, S_y and S_z are the operators before the transformation.

Appendix C

Evolution of the phase factor A

Assume that at time t the state vector can be written as

$$|\psi(t)\rangle = e^{-iA(t)/\hbar}|N_a : \phi_a(t),\, N_b : \phi_b(t)\,\rangle \tag{C.1}$$

N_ε is the number of particles in component ε conserved during the evolution. The state evolution, according to Schrödinger equation, reads

$$i\hbar\frac{d}{dt}|\psi\rangle = \mathcal{H}|\psi\rangle \tag{C.2}$$

where $\mathcal{H}$ is the Hamiltonian in the Hartree-Fock approximation, whose quantum average is

$$\begin{aligned}\langle\mathcal{H}\,\rangle = \sum_{\varepsilon=a,b}&\left[N_\varepsilon\langle\phi_\varepsilon|h_\varepsilon|\phi_\varepsilon\rangle + \frac{g_{\varepsilon\varepsilon}}{2}N_\varepsilon\left(N_\varepsilon-1\right)\int d^3r|\phi_\varepsilon|^4\right]\\ &+ N_aN_bg_{ab}\int d^3r|\phi_a|^2|\phi_b|^2\,.\end{aligned} \tag{C.3}$$

In Eq.(C.3) h_ε is the one-particle Hamiltonian (4.2), and the evolution of ϕ_ε are described by coupled Gross-Pitaevskii equation (4.10). Inserting Eq.(C.1) into the Schrödinger equation (C.2), and then multiply by $\langle N_a : \phi_a,\, N_b : \phi_b\,|\, e^{iA(t)/\hbar}$ on both sides, one gets

$$\begin{aligned}\dot{A} + i\hbar\langle N_a : \phi_a,\, N_b : \phi_b\,|&\frac{d}{dt}|N_a : \phi_a,\, N_b : \phi_b\,\rangle\\ &= \langle N_a : \phi_a,\, N_b : \phi_b\,|\mathcal{H}|N_a : \phi_a,\, N_b : \phi_b\,\rangle\end{aligned} \tag{C.4}$$

By using the Gross-Pitaevskii equation (4.10) for the derivative of the wave function ϕ_ε and the average of the Hamiltonian (C.3), we obtain the evolution of the phase factor A,

$$\dot{A} = -\sum_{\varepsilon=a,b}N_\varepsilon(N_\varepsilon-1)\frac{g_{\varepsilon\varepsilon}}{2}\int d^3r|\phi_\varepsilon|^4 - N_aN_bg_{ab}\int d^3r|\phi_a|^2|\phi_b|^2\,. \tag{C.5}$$

Appendix D

Numerical solution of GPE

In this appendix, we show the method to calculate the stationary solution of Gross-Pitaevskii equation

$$i\hbar\frac{\phi(\mathbf{r})}{dt}=\left[-\frac{\hbar^2}{2M}\nabla^2+U(\mathbf{r})+Ng|\phi(\mathbf{r})|^2\right]\phi(\mathbf{r}), \tag{D.1}$$

where $U(\mathbf{r})$ is the external trapping potential, g is the strength of the interaction, and N is total the number of atoms.

In chapter 4, one needs to calculate the ground state of Eq.(D.1) to obtain the wave function $\phi_0(\mathbf{r})$ as the initial condition for the dynamical spin squeezing model Eq.(4.11). In chapter 7, both ground state and first excitation state of Eq.(D.1), $\phi_S(\mathbf{r})$ and $\phi_A(\mathbf{r})$, are needed in order to calculate the double-well system parameters E_c (Eq.7.6) and E_j (Eq.7.7). Furthermore, the method presented here can be extended to the coupled Gross-Pitaevskii equation (2.17), by which we calculate the ground states $\phi_a(\mathbf{r})$ and $\phi_b(\mathbf{r})$ with the correspond number of atoms $N_a=\bar{N}_a$ and $N_b=\bar{N}_b$. These states will be needed in the two-mode model for spin squeezing described in chapter 2 and chapter 3.

The main idea of our method is to find the local minimum of the energy functional

$$E[\phi,\phi^*]=\int d^3r\left[N\phi^*(\mathbf{r})h_0\phi(\mathbf{r})+\frac{N^2g}{2}|\phi(\mathbf{r})|^4\right], \tag{D.2}$$

where $h_0=-\hbar^2\nabla^2/(2M)+U(\mathbf{r})$, by varying the wave function ϕ under the constraint that ϕ is normalized to unity, i.e.

$$\int d^3r\,|\phi(\mathbf{r})|^2=1\,. \tag{D.3}$$

To do this, we first assume that, in the next time step, the wave function can be written as

$$\phi = \phi_1 + \lambda\,\delta\phi_1\,. \tag{D.4}$$

where ϕ_1 is the wave function in the present step. Rewriting the energy functional (D.2), taking into account the constrain, one gets

$$E[\phi,\phi^*] = \frac{N\int \phi^* h_0 \phi}{\int \phi^*\phi} + \frac{N^2 g \int \phi^*\phi^*\phi\phi}{2\int \phi^*\phi}\,. \tag{D.5}$$

Inserting Eq.(D.4) into Eq.(D.5) allows ont to implement a line minimization of $E[\phi,\phi^*]$ with respect to λ. By defining the following functions,

$$T_n(0) = \int \phi_1^*\,\phi_1\,, \tag{D.6}$$

$$T_n(1) = 2\mathrm{Re}\int \phi_1^*\,\delta\phi_1\,, \tag{D.7}$$

$$T_n(2) = \int \delta\phi_1^*\,\delta\phi_1\,, \tag{D.8}$$

$$T_c(0) = N\int \phi_1^*\,h_0\,\phi_1\,, \tag{D.9}$$

$$T_c(1) = 2\mathrm{Re}\,N\int \phi_1^*\,h_0\,\delta\phi_1\,, \tag{D.10}$$

$$T_c(2) = N\int \delta\phi_1^*\,\delta\phi_1\,, \tag{D.11}$$

$$T_i(0) = \frac{N^2 g}{2}\int |\phi_1|^4\,, \tag{D.12}$$

$$T_i(1) = 2\mathrm{Re}\,N^2 g\int |\phi_1|^2\,\phi_1^*\,\delta\phi_1\,, \tag{D.13}$$

$$T_i(2) = N^2 g\left[2\int (\mathrm{Re}\,\phi_1^*\,\delta\phi_1)^2 + \int |\phi_1|^2|\delta\phi_1|^2\right]\,, \tag{D.14}$$

$$T_i(3) = 2\mathrm{Re}\,N^2 g\int |\delta\phi_1|^2\,\phi_1^*\,\delta\phi_1\,, \tag{D.15}$$

$$T_i(4) = \frac{N^2 g}{2}\int |\delta\phi_1|^4\,, \tag{D.16}$$

where the terms such as $h_0\,\phi_1$ are calculated by splitting Fourier spectral method [93], the energy (D.5) can be written as a function of λ,

$$E(\lambda) = \frac{\sum_{k=0}^{2} T_c(k)\lambda^k}{\sum_{k=0}^{2} T_n(k)\lambda^k} + \frac{\sum_{k=0}^{4} T_i(k)\lambda^k}{\left[\sum_{k=0}^{2} T_n(k)\lambda^k\right]^2} = \frac{\sum_{k=0}^{4} p(k)\lambda^k}{\sum_{k=0}^{4} q(k)\lambda^k}\,, \tag{D.17}$$

with

$$p(0) = T_i(0) + T_c(0) \cdot T_n(0)\,, \tag{D.18}$$

$$p(1) = T_c(1) \cdot T_n(1) + T_i(1) + T_c(1) \cdot T_n(0)\,, \tag{D.19}$$

$$p(2) = T_c(0) \cdot T_n(2) + T_c(2) \cdot T_n(0) + T_i(2) \cdot T_c(1) \cdot T_n(1)\,, \tag{D.20}$$

$$p(3) = T_c(1) \cdot T_n(2) + T_c(2) \cdot T_n(1) + T_i(3)\,, \tag{D.21}$$

$$p(4) = T_i(4) + T_c(2) \cdot T_n(2)\,, \tag{D.22}$$

$$q(0) = T_n^2(0)\,, \tag{D.23}$$

$$q(1) = 2T_n(0) \cdot T_n(1)\,, \tag{D.24}$$

$$q(2) = 2T_n(0) \cdot T_n(2) + T_n^2(1)\,, \tag{D.25}$$

$$q(3) = 2T_n(1) \cdot T_n(2)\,, \tag{D.26}$$

$$q(4) = T_n^2(2)\,. \tag{D.27}$$

Solving the equation numerically for λ

$$\frac{dE(\lambda)}{d\lambda} = 0\,, \tag{D.28}$$

we obtain $\lambda_{\min}$ which brings the energy $E[\phi, \phi^*]$ in the next step to a minimum along the direction $\delta\phi_1$. After several iterations, $E[\phi, \phi^*]$ is moved to a place, corresponding to the final wave function ϕ, very close to its local minimum.

A key point of this method is how to chose the direction $\delta\phi_1$. An intuitive choice would be the gradient direction, which results in

$$\delta\phi_1 = -\frac{\delta E[\phi_1, \phi_1^*]}{\delta\phi_1} \propto -\left[h_0\phi_1 + U(\mathbf{r})\phi_1 + Ng|\phi_1|^2\phi_1\right]. \tag{D.29}$$

However, this choice, leading to the algorithm *Steepest Descent Method*, is not very efficient for our case. The algorithm used here is is so-called *Conjugate Gradient Methods* [94], in which the direction $\delta\phi_1$ is constructed to be *conjugate* to the old gradient, insofar as possible to all previous directions traversed. This results in the real direction $\widetilde{\delta\phi_1}$ along which we perform the energy diminishing,

$$\widetilde{\delta\phi_1} = \delta\phi_1 - \frac{\int \delta\phi_1^* \left(\widetilde{\delta\phi_0} - \delta\phi_1\right)}{\int |\widetilde{\delta\phi_0}|^2}\, \widetilde{\delta\phi_0}\,, \tag{D.30}$$

where $\delta\widetilde{\phi}_0$ is the direction used in the previous step, and $\delta\phi_1$ is calculated from Eq.(D.29). For the first step, we choose $\delta\widetilde{\phi}_1 = \delta\phi_1$. Replacing $\delta\phi_1$ by $\delta\widetilde{\phi}_1$ in Eq.(D.4), we finally get the wave function in the next step

$$\phi = \phi_1 + \lambda_{\min}\,\delta\widetilde{\phi}_1\,. \tag{D.31}$$

After each iteration, the wave function ϕ should be renormalized.

Since the final wave function $\phi(\mathbf{r})$ is obtained by looking for the local minimum of the energy functional $E[\phi, \phi^*]$, choosing the trial wave function properly can simplify the calculation. For example in the calculations for the double-well, the trial wave function for the ground state is the 3D Thomas-Fermi profile centered in the minimum of each well, and for the first excitation state, we choose the trial wave function as

$$\phi_A^{\text{trial}}(\mathbf{r}) = \tanh(x)\cdot\phi_S(\mathbf{r})\,, \tag{D.32}$$

where $\phi_S(\mathbf{r})$ is the ground state obtained from the same trap configuration, and the double-well is split along the x direction. The method will fail when Eq.(D.28) does not have a real solution for λ, implying that there does not exist a minimum along $\delta\widetilde{\phi}_1$. It rarely happens in the calculations of the ground states, but appears sometimes when calculate the first excitation states with a very low barrier height ($V_b \simeq 0$). In this case, using more points in the spatial grid, which means increasing the dimension of E, could help. Another solution is to change the trail wave function to avoid reaching ϕ_1 which will abort the calculation. Indeed, we find that Eq.(D.32) is a very good trail wave function for the first excitation states.

Our method is very efficient that a complete 3D trap configuration can be used in the simulation. In the calculations for double-well, the spatial grid is chosen as 256 × 100 × 64. With the above trial wave functions, both the ground state and the first excitation can be found within 30 minutes (using single processor of Intel Xeon CPU 3.00 GHz). In Fig.D.1 and Fig.D.2 we give an example, the ground states and the first excitation states calculated for double-well. As described in chapter 7, the 3D trapping potential is given by another simulation developed by the experimentalists, based on current configuration on the atom chip. The trap approximately has a banana shape, and the atom chip lies in the plane perpendicular to the z direction. We show the density profile integrated along axis-y. The corresponding current are $I_2 = 2.02 : 0.04 : 2.30\,\text{mA}$.

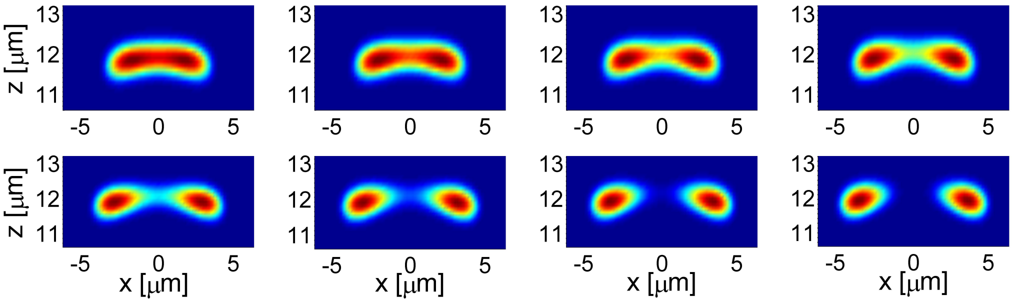

Figure D.1: Density profile of the ground states in the double-well, integrated along axis-y. The total number of atoms is $N = 1300$. The corresponding current are $I_2 = 2.02 : 0.04 : 2.30\,\mathrm{mA}$.

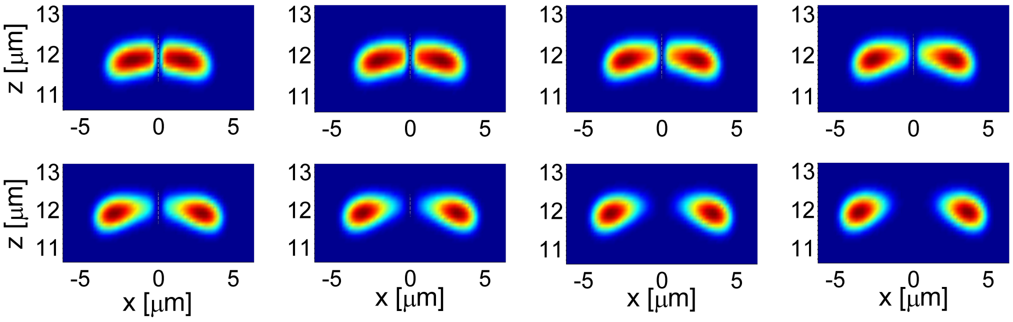

Figure D.2: Density profile of the first excitation states in the double-well, integrated along axis-y. The total number of atoms is $N = 1300$. The corresponding current are $I_2 = 2.02 : 0.04 : 2.30\,\mathrm{mA}$.

Appendix E

$\mathrm{Var}(N_l - N_r)$ calculated from the $g^{(1)}$ function

To calculate the variance of $N_l - N_r$ in Eq.(7.21), one needs to calculate

$$\mathcal{I} = 2\left\{\int_{\mathbf{r}\in L}\int_{\mathbf{r}'\in L}\left[g^{(1)}(\mathbf{r},\mathbf{r}')\right]^2 - \int_{\mathbf{r}\in L}\int_{\mathbf{r}'\in R}\left[g^{(1)}(\mathbf{r},\mathbf{r}')\right]^2\right\} \tag{E.1}$$

By using the $g^{(1)}$ function given in Eq.(7.26), we find

$$\begin{aligned}\left[g^{(1)}(\mathbf{r},\mathbf{r}')\right]^2 &= \sum_{s=1}^{\infty}\sum_{l=1}^{s-1}\tilde{z}^s\left(\frac{M\bar{\omega}}{2\pi\hbar}\right)^3\prod_{\alpha=x,y,z}\left(e^{-s\eta_\alpha}C_\alpha\right)^{-1/2} \\ &\cdot\exp\left\{-\frac{M\omega_\alpha}{4\hbar}\left[A_\alpha\left(r_\alpha+r'_\alpha\right)^2 - B_\alpha\left(r_\alpha-r'_\alpha\right)^2\right]\right\}\,, \end{aligned}\tag{E.2}$$

where we have defined

$$A_\alpha = \tanh\left(\frac{l\eta_\alpha}{2}\right) + \tanh\left[\frac{(s-l)\eta_\alpha}{2}\right], \tag{E.3}$$

$$B_\alpha = \coth\left(\frac{l\eta_\alpha}{2}\right) + \coth\left[\frac{(s-l)\eta_\alpha}{2}\right], \tag{E.4}$$

$$C_\alpha = \sinh\left(l\eta_\alpha\right)\sinh\left[(s-l)\eta_\alpha\right]. \tag{E.5}$$

For the function $f(x,x') = \exp[-\alpha(x+x')^2 - \beta(x-x')^2]$ and $\alpha,\beta > 0$, one has the integration relation

$$\int_{-\infty}^{+\infty}dx\int_{-\infty}^{+\infty}dx'\,f(x,x') = \frac{\pi}{2}\frac{1}{\sqrt{\alpha\beta}}\,. \tag{E.6}$$

Using Eq.(E.6), the integration of $\left[g^{(1)}(\mathbf{r},\mathbf{r}')\right]^2$ in y and z direction gives

$$\begin{aligned}
&\int_{-\infty}^{+\infty} dy\, dz \int_{-\infty}^{+\infty} dy'\, dz' \, \left[g^{(1)}(\mathbf{r},\mathbf{r}')\right]^2 \\
&= \sum_{s=1}^{\infty}\sum_{l=1}^{s-1} \tilde{z}^s \left(\frac{M\bar{\omega}}{2\pi\hbar}\right)^3 \left\{ \prod_{\alpha=y,z} \left(\frac{2\pi\hbar}{M\omega_\alpha}\right) \left[e^{-s\eta_\alpha/2} 2\sinh\left(\frac{s\eta_\alpha}{2}\right)\right]^{-1} \right\} \\
&\cdot \left(e^{-s\eta_x} C_x\right)^{-1/2} \exp\left\{ -\frac{M\omega_x}{4\hbar} \left[A_x\,(x+x')^2 - B_x\,(x-x')^2\right] \right\} ,
\end{aligned} \tag{E.7}$$

where we have used the fact that

$$A_\alpha B_\alpha = \frac{4}{C_\alpha} \sinh^2\left(\frac{s\eta_\alpha}{2}\right) . \tag{E.8}$$

Then it remains the integration along x direction. Again for the function $f(x,x')$, if $\beta > \alpha > 0$, one has

$$\begin{aligned}
&\int_{-\infty}^{0} dx \int_{-\infty}^{0} dx'\, f(x,x') - \int_{-\infty}^{0} dx \int_{0}^{+\infty} dx'\, f(x,x') \\
&= \frac{1}{\sqrt{\alpha\beta}} \left[\frac{\pi}{4} - \arctan\sqrt{\frac{\alpha}{\beta}}\right] .
\end{aligned} \tag{E.9}$$

Using Eq.(E.9), the integration of $\left[g^{(1)}(\mathbf{r},\mathbf{r}')\right]^2$ in Eq.(E.1) can be written as

$$\begin{aligned}
\mathcal{I} =& \sum_{s=1}^{\infty}\sum_{l=1}^{s-1} \tilde{z}^s \left\{ \prod_{\alpha=x,y,z} \left[e^{-s\eta_\alpha/2} 2\sinh\left(\frac{s\eta_\alpha}{2}\right)\right]^{-1} \right\} \\
&\cdot \left\{ 1 - \frac{4}{\pi} \arctan\sqrt{\tanh\left(\frac{l\eta_x}{2}\right) \tanh\left[\frac{(s-l)\eta_x}{2}\right]} \right\} ,
\end{aligned} \tag{E.10}$$

where we have used the fact that

$$\frac{A_\alpha}{B_\alpha} = \tanh\left(\frac{l\eta_\alpha}{2}\right) \tanh\left[\frac{(s-l)\eta_\alpha}{2}\right] . \tag{E.11}$$

Bibliography

[1] S. N Bose. Plancks Gesetz und Lichtquantenhypothese. *Z. Phys.*, 26(6):178, 1924.

[2] A. Einstein. Quantentheorie des einatomigen idealen Gases. *Sitzungsber. Preuss. Akad. Wiss.*, page 261, 1924.

[3] M. H. Anderson, J. R. Ensher, M. R. Matthews, C. E. Wieman, and E. A. Cornell. Observation of Bose-Einstein Condensation in a Dilute Atomic Vapor. *Science*, 269(5221):198–201, 1995.

[4] C. C. Bradley, C. A. Sackett, J. J. Tollett, and R. G. Hulet. Evidence of Bose-Einstein Condensation in an Atomic Gas with Attractive Interactions. *Phys. Rev. Lett.*, 75(9):1687–1690, 1995.

[5] K. B. Davis, M. O. Mewes, M. R. Andrews, N. J. van Druten, D. S. Durfee, D. M. Kurn, and W. Ketterle. Bose-Einstein Condensation in a Gas of Sodium Atoms. *Phys. Rev. Lett.*, 75(22):3969–3973, 1995.

[6] M. R. Andrews, C. G. Townsend, H.-J. Miesner, D. S. Durfee, D. M. Kurn, and W. Ketterle. Observation of Interference Between Two Bose Condensates. *Science*, 275(5300):637–641, 1997.

[7] B. P. Anderson and M. A. Kasevich. Macroscopic Quantum Interference from Atomic Tunnel Arrays. *Science*, 282(5394):1686–1689, 1998.

[8] M. Greiner, O. Mandel, T. Esslinger, T. W. Hänsch, and I. Bloch. Quantum phase transition from a superfluid to a Mott insulator in a gas of ultracold atoms. *Nature*, 415:39–44, 2002.

[9] L. Deng, E. W. Hagley, J. Wen, M. Trippenbach, Y. Band, P. S. Julienne, J. E. Simsarian, K. Helmerson, S. L. Rolston, and W. D. Phillips. Four-wave mixing with matter waves. *Nature*, 398:218–220, 1999.

[10] S. Inouye, A. P. Chikkatur, D. M. Stamper-Kurn, J. Stenger, D. E. Pritchard, and W. Ketterle. Superradiant Rayleigh Scattering from a Bose-Einstein Condensate. *Science*, 285(5427):571–574, 1999.

[11] M. Kozuma, Y. Suzuki, Y. Torii, T. Sugiura, T. Kuga, E. W. Hagley, and L. Deng. Phase-Coherent Amplification of Matter Waves. *Science*, 286(5448):2309–2312, 1999.

[12] S. Inouye, R. F. Löw, S. Gupta, T. Pfau, A. Görlitz, T. L. Gustavson, D. E. Pritchard, and W. Ketterle. Amplification of Light and Atoms in a Bose-Einstein Condensate. *Phys. Rev. Lett.*, 85(20):4225–4228, 2000.

[13] M.-O. Mewes, M. R. Andrews, D. M. Kurn, D. S. Durfee, C. G. Townsend, and W. Ketterle. Output Coupler for Bose-Einstein Condensed Atoms. *Phys. Rev. Lett.*, 78(4):582–585, 1997.

[14] I. Bloch, T. W. Hänsch, and T. Esslinger. Atom Laser with a cw Output Coupler. *Phys. Rev. Lett.*, 82(15):3008–3011, 1999.

[15] V. M. Pérez-García, H. Michinel, and H. Herrero. Bose-Einstein solitons in highly asymmetric traps. *Phys. Rev. A*, 57(5):3837–3842, 1998.

[16] S. Burger, K. Bongs, S. Dettmer, W. Ertmer, K. Sengstock, A. Sanpera, G. V. Shlyapnikov, and M. Lewenstein. Dark Solitons in Bose-Einstein Condensates. *Phys. Rev. Lett.*, 83(25):5198–5201, 1999.

[17] J. Denschlag, J. E. Simsarian, D. L. Feder, Charles W. Clark, L. A. Collins, J. Cubizolles, L. Deng, E. W. Hagley, K. Helmerson, W. P. Reinhardt, S. L. Rolston, B. I. Schneider, and W. D. Phillips. Generating Solitons by Phase Engineering of a Bose-Einstein Condensate. *Science*, 287(5450):97–101, 2000.

[18] L. Khaykovich, F. Schreck, G. Ferrari, T. Bourdel, J. Cubizolles, L. D. Carr, Y. Castin, and C. Salomon. Formation of a Matter-Wave Bright Soliton. *Science*, 296(5571):1290–1293, 2002.

[19] M. R. Matthews, B. P. Anderson, P. C. Haljan, D. S. Hall, C. E. Wieman, and E. A. Cornell. Vortices in a Bose-Einstein Condensate. *Phys. Rev. Lett.*, 83(13):2498–2501, 1999.

[20] K. W. Madison, F. Chevy, W. Wohlleben, and J. Dalibard. Vortex Formation in a Stirred Bose-Einstein Condensate. *Phys. Rev. Lett.*, 84(5):806–809, 2000.

[21] J. R. Abo-Shaeer, C. Raman, J. M. Vogels, and W. Ketterle. Observation of Vortex Lattices in Bose-Einstein Condensates. *Science*, 292(5516):476–479, 2001.

[22] I. Bloch, M. Köhl, M. Greiner, T. W. Hänsch, and T. Esslinger. Optics with an Atom Laser Beam. *Phys. Rev. Lett.*, 87(3):030401, 2001.

[23] A. Sørensen, L.-M. Duan, J. I. Cirac, and P. Zoller. Many-particle entanglement with Bose-Einstein condensates. *Nature*, 409:63–66, 2001.

[24] J. I. Cirac, M. Lewenstein, K. Mølmer, and P. Zoller. Quantum superposition states of Bose-Einstein condensates. *Phys. Rev. A*, 57(2):1208–1218, 1998.

[25] Y. Castin. Bose-Einstein condensates in atomic gases: simple theoretical results. *arXiv:cond-mat/0105058*, 2001.

[26] A. S. Sørensen and K. Mølmer. Entanglement and Extreme Spin Squeezing. *Phys. Rev. Lett.*, 86(20):4431–4434, 2001.

[27] A. D. Cronin, J. Schmiedmayer, and D. E. Pritchard. Optics and interferometry with atoms and molecules. *Rev. Mod. Phys.*, 81(3):1051–1129, 2009.

[28] D. J. Wineland, J. J. Bollinger, W. M. Itano, F. L. Moore, and D. J. Heinzen. Spin squeezing and reduced quantum noise in spectroscopy. *Phys. Rev. A*, 46(11):R6797–R6800, 1992.

[29] D. J. Wineland, J. J. Bollinger, W. M. Itano, and D. J. Heinzen. Squeezed atomic states and projection noise in spectroscopy. *Phys. Rev. A*, 50(1):67–88, 1994.

[30] J. M. Vogels, K. Xu, and W. Ketterle. Generation of Macroscopic Pair-Correlated Atomic Beams by Four-Wave Mixing in Bose-Einstein Condensates. *Phys. Rev. Lett.*, 89(2):020401, 2002.

[31] C. Orzel, A. K. Tuchman, M. L. Fenselau, M. Yasuda, and M. A. Kasevich. Squeezed States in a Bose-Einstein Condensate. *Science*, 291(5512):2386–2389, 2001.

[32] S. Inouye, M. R. Andrews, J. Stenger, H.-J. Miesner, D. M. Stamper-Kurn, and W. Ketterle. Observation of Feshbach resonances in a Bose-Einstein condensate. *Nature*, 392:151–154, 1998.

[33] D.S. Petrov, D.M. Gangardt, and G.V. Shlyapnikov. Low-dimensional trapped gases. *J. Phys. IV France*, 116:5–44, 2004.

[34] A. André, A. S. Sørensen, and M. D. Lukin. Stability of Atomic Clocks Based on Entangled Atoms. *Phys. Rev. Lett.*, 92(23):230801, 2004.

[35] Yun Li, Y. Castin, and A. Sinatra. Optimum Spin Squeezing in Bose-Einstein Condensates with Particle Losses. *Phys. Rev. Lett.*, 100(21):210401, 2008.

[36] Yun Li, P. Treutlein, J. Reichel, and A. Sinatra. Spin squeezing in a bimodal condensate: spatial dynamics and particle losses. *Eur. Phys. J. B*, 68(3):365–381, 2009.

[37] I. D. Leroux, M. H. Schleier-Smith, and V. Vuletić. Orientation-Dependent Entanglement Lifetime in a Squeezed Atomic Clock. *arXiv:quant-ph/1004.1725*, 2010.

[38] P. Treutlein, P. Hommelhoff, T. Steinmetz, T. W. Hänsch, and J. Reichel. Coherence in Microchip Traps. *Phys. Rev. Lett.*, 92(20):203005, 2004.

[39] P. Rosenbusch. Magnetically trapped atoms for compact atomic clocks. *Appl. Phys. B*, 95:227–235, 2009.

[40] M. F. Riedel, P. Böhi, Yun Li, T. W. Hänsch, A. Sinatra, and P. Treutlein. Atom-chip-based generation of entanglement for quantum metrology. *Nature*, 464:1170–1173, 2010.

[41] C. Gross, T. Zibold, E. Nicklas, J. Estève, and M. K. Oberthaler. Nonlinear atom interferometer surpasses classical precision limit. *Nature*, 464:1165–1169, 2010.

[42] J. Estève, C. Gross, A. Weller, S. Giovanazzi, and M.K. Oberthaler. Squeezing and entanglement in Bose-Einstein condensate. *Nature*, 455:1216, 2008.

[43] K. Maussang, G. E. Marti, T. Schneider, P. Treutlein, Yun. Li, A. Sinatra, R. Long, J. Estève, and J. Reichel. Enhanced and reduced atom number fluctuations in a BEC splitter. *arXiv:quant-ph/1005.1922*, 2010.

[44] M. Kitagawa and M. Ueda. Squeezed spin states. *Phys. Rev. A*, 47(6):5138–5143, 1993.

[45] Indeed, there are alternative definitions of spin squeezing as in [44, 26] (entanglement criterion) and in [29, 28] (criterion for metrologhical gain). Here we will only use on the later one as our squeezing measurement.

[46] G. Santarelli, Ph. Laurent, P. Lemonde, A. Clairon, A. G. Mann, S. Chang, A. N. Luiten, and C. Salomon. Quantum Projection Noise in an Atomic Fountain: A High Stability Cesium Frequency Standard. *Phys. Rev. Lett.*, 82(23):4619–4622, 1999.

[47] Q. A. Turchette, C. S. Wood, B. E. King, C. J. Myatt, D. Leibfried, W. M. Itano, C. Monroe, and D. J. Wineland. Deterministic Entanglement of Two Trapped Ions. *Phys. Rev. Lett.*, 81(17):3631–3634, 1998.

[48] V. Meyer, M. A. Rowe, D. Kielpinski, C. A. Sackett, W. M. Itano, C. Monroe, and D. J. Wineland. Experimental Demonstration of Entanglement-Enhanced Rotation Angle Estimation Using Trapped Ions. *Phys. Rev. Lett.*, 86(26):5870–5873, 2001.

[49] D. Leibfried, M. D. Barrett, T. Schaetz, J. Britton, J. Chiaverini, W. M. Itano, J. D. Jost, C. Langer, and D. J. Wineland. Toward Heisenberg-Limited Spectroscopy with Multiparticle Entangled States. *Science*, 304(5676):1476–1478, 2004.

[50] J. Hald, J. L. Sørensen, C. Schori, and E. S. Polzik. Spin Squeezed Atoms: A Macroscopic Entangled Ensemble Created by Light. *Phys. Rev. Lett.*, 83(7):1319–1322, 1999.

[51] A. E. Kozhekin, K. Mølmer, and E. Polzik. Quantum memory for light. *Phys. Rev. A*, 62(3):033809, 2000.

[52] A. Dantan and M. Pinard. Quantum-state transfer between fields and atoms in electromagnetically induced transparency. *Phys. Rev. A*, 69(4):043810, 2004.

[53] M. H. Schleier-Smith, I. D. Leroux, and V. Vuletić. Squeezing the collective spin of a dilute atomic ensemble by cavity feedback. *Phys. Rev. A*, 81(2):021804, 2010.

[54] I. D. Leroux, M. H. Schleier-Smith, and V. Vuletić. Implementation of Cavity Squeezing of a Collective Atomic Spin. *Phys. Rev. Lett.*, 104(7):073602, 2010.

[55] A. Kuzmich, L. Mandel, J. Janis, Y. E. Young, R. Ejnisman, and N. P. Bigelow. Quantum nondemolition measurements of collective atomic spin. *Phys. Rev. A*, 60(3):2346–2350, 1999.

[56] A. Kuzmich, L. Mandel, and N. P. Bigelow. Generation of Spin Squeezing via Continuous Quantum Nondemolition Measurement. *Phys. Rev. Lett.*, 85(8):1594–1597, 2000.

[57] JM Geremia, J. K. Stockton, and H. Mabuchi. Real-Time Quantum Feedback Control of Atomic Spin-Squeezing. *Science*, 304(5668):270–273, 2004.

[58] M. H. Schleier-Smith, I. D. Leroux, and V. Vuletić. States of an Ensemble of Two-Level Atoms with Reduced Quantum Uncertainty. *Phys. Rev. Lett.*, 104(7):073604, 2010.

[59] J. Appel, P. J. Windpassinger, D. Oblak, U. B. Hoff, N. Kjaergaard, and E. S. Polzik. Mesoscopic atomic entanglement for precision measurements beyond the standard quantum limit. *Proc. Natl. Acad. Sci.*, 106(27):10960–10965, 2009.

[60] A. Louchet-Chauvet, J. Appel, J. J. Renema, D. Oblak, N. Kjærgaard, and E. S. Polzik. Entanglement-assisted atomic clock beyond the projection noise limit. *arXiv:quant-ph/0912.3895*, 2009.

[61] K. Mølmer, Y. Castin, and J. Dalibard. Monte Carlo wave-function method in quantum optics. *J. Opt. Soc. Am. B*, 10(3):524–538, 1993.

[62] H.J Carmichael. *An Open Systems Approach to Quantum Optics.* Springer-Verlag Berlin. Heidelberg, 2nd edition, 1993.

[63] A. Sinatra and Y. Castin. Phase dynamics of Bose-Einstein condensates: Losses versus revivals. *Eur. Phys. J. D*, 4(3):247–260, 1998.

[64] K. M. Mertes, J. W. Merrill, R. Carretero-González, D. J. Frantzeskakis, P. G. Kevrekidis, and D. S. Hall. Nonequilibrium Dynamics and Superfluid Ring Excitations in Binary Bose-Einstein Condensates. *Phys. Rev. Lett.*, 99(19):190402, 2007.

[65] E. A. Burt, R. W. Ghrist, C. J. Myatt, M. J. Holland, E. A. Cornell, and C. E. Wieman. Coherence, Correlations, and Collisions: What One Learns about Bose-Einstein Condensates from Their Decay. *Phys. Rev. Lett.*, 79(3):337–340, 1997.

[66] S. Thanvanthri and Z. Dutton. Spatial dynamics and spin squeezing in Bose-Einstein condensates. *Phys. Rev. A*, 75(2):023618, 2007.

[67] M. Erhard, H. Schmaljohann, J. Kronjäger, K. Bongs, and K. Sengstock. Measurement of a mixed-spin-channel Feshbach resonance in Rb87. *Phys. Rev. A*, 69(3):032705, 2004.

[68] A. Widera, S. Trotzky, P. Cheinet, S. Fölling, F. Gerbier, I. Bloch, V. Gritsev, M. D. Lukin, and E. Demler. Quantum Spin Dynamics of Mode-Squeezed Luttinger Liquids in Two-Component Atomic Gases. *Phys. Rev. Lett.*, 100(14):140401, 2008.

[69] G. Smirne, R. M. Godun, D. Cassettari, V. Boyer, C. J. Foot, T. Volz, N. Syassen, S. Dürr, G. Rempe, M. D. Lee, K. Góral, and T. Köhler. Collisional relaxation of Feshbach molecules and three-body recombination in Rb87 Bose-Einstein condensates. *Phys. Rev. A*, 75(2):020702, 2007.

[70] A. Sinatra and Y. Castin. Binary mixtures of Bose-Einstein condensates: Phase dynamics and spatial dynamics. *Eur. Phys. J. D*, 8(3):319–332, 2000.

[71] A. S. Sørensen. Bogoliubov theory of entanglement in a Bose-Einstein condensate. *Phys. Rev. A*, 65(4):043610, 2002.

[72] D. S. Hall, M. R. Matthews, J. R. Ensher, C. E. Wieman, and E. A. Cornell. Dynamics of Component Separation in a Binary Mixture of Bose-Einstein Condensates. *Phys. Rev. Lett.*, 81(8):1539–1542, 1998.

[73] Yu. Kagan, E. L. Surkov, and G. V. Shlyapnikov. Evolution of a Bose-condensed gas under variations of the confining potential. *Phys. Rev. A*, 54(3):R1753–R1756, 1996.

[74] Y. Castin and R. Dum. Bose-Einstein Condensates in Time Dependent Traps. *Phys. Rev. Lett.*, 77(27):5315–5319, 1996.

[75] S. Stringari. Collective Excitations of a Trapped Bose-Condensed Gas. *Phys. Rev. Lett.*, 77(12):2360–2363, 1996.

[76] As we are pretty far from the Feshbach resonance, we assume for the crossed *ab* two-body loss rate the same value measured in [64] for the $|F=1, m_F=-1\rangle$, $|F=2, m_F=1\rangle$ state.

[77] D. M. Stamper-Kurn, M. R. Andrews, A. P. Chikkatur, S. Inouye, H.-J. Miesner, J. Stenger, and W. Ketterle. Optical Confinement of a Bose-Einstein Condensate. *Phys. Rev. Lett.*, 80(10):2027–2030, 1998.

[78] P. Treutlein, T. W. Hänsch, J. Reichel, A. Negretti, M. A. Cirone, and T. Calarco. Microwave potentials and optimal control for robust quantum gates on an atom chip. *Phys. Rev. A*, 74(2):022312, 2006.

[79] P. Böhi, M. F. Riedel, J. Hoffrogge, J. Reichel, T. W. Hänsch, and P. Treutlein. Coherent manipulation of Bose-Einstein condensates with state-dependent microwave potentials on an atom chip. *Nat. Phys.*, 5(8):592, 2009.

[80] U. V. Poulsen and K. Mølmer. Quantum beam splitter for atoms. *Phys. Rev. A*, 65(3):033613, 2002.

[81] A. Couvert, T. Kawalec, G. Reinaudi, and D. Guery-Odelin. Optimal transport of ultracold atoms in the non-adiabatic regime. *Eur. Phys. Lett.*, 83(1):13001–13005, 2008.

[82] A. Sinatra, Y. Castin, and Yun LI. Particle number fluctuations in a cloven trapped Bose gas at finite temperature. *Phys. Rev. A*, 2010 (accepted).

[83] A.J Leggett. *in Proceedings of the 16th International Conference on Atomic Physics*, pages 154–169. AIP Conf. Proc. No. 477, (AIP, Woodbury, New York), Aug 1998.

[84] S. Raghavan, A. Smerzi, S. Fantoni, and S. R. Shenoy. Coherent oscillations between two weakly coupled Bose-Einstein condensates: Josephson effects, π oscillations, and macroscopic quantum self-trapping. *Phys. Rev. A*, 59(1):620–633, 1999.

[85] D. Ananikian and T. Bergeman. Gross-Pitaevskii equation for Bose particles in a double-well potential: Two-mode models and beyond. *Phys. Rev. A*, 73(1):013604, 2006.

[86] E. A. Ostrovskaya, Y. S. Kivshar, M. Lisak, B. Hall, F. Cattani, and D. Anderson. Coupled-mode theory for Bose-Einstein condensates. *Phys. Rev. A*, 61(3):031601, 2000.

[87] C. Menotti, J. R. Anglin, J. I. Cirac, and P. Zoller. Dynamic splitting of a Bose-Einstein condensate. *Phys. Rev. A*, 63(2):023601, 2001.

[88] R. Gati, J. Esteve, B. Hemmerling, T. B. Ottenstein, J. Appmeier, A. Weller, and M. K. Oberthaler. A primary noise thermometer for ultracold Bose gases. *New Journal of Physics*, 8(9):189, 2006.

[89] L. Pezzé, A. Smerzi, G. P. Berman, A. R. Bishop, and L. A. Collins. Dephasing and breakdown of adiabaticity in the splitting of Bose-Einstein condensates. *New Journal of Physics*, 7(1):85, 2005.

[90] R. Gati, B. Hemmerling, J. Fölling, M. Albiez, and M. K. Oberthaler. Noise Thermometry with Two Weakly Coupled Bose-Einstein Condensates. *Phys. Rev. Lett.*, 96(13):130404, 2006.

[91] L. Landau and E. Lifchitz. *Physique théorique, Tome V : Physique Statistique*, pages 103–104. Academic Press, 4th edition, 1994.

[92] S. Grossmann and M. Holthaus. On Bose-Einstein condensation in harmonic traps. *Physics Letters A*, 208(3):188 – 192, 1995.

[93] W. Bao, D. Jaksch, and P. A. Markowich. Numerical solution of the Gross-Pitaevskii equation for Bose-Einstein condensation. *Journal of Computational Physics*, 187(1):318 – 342, 2003.

[94] W. H. Press, S. A. Teukolsky, W. T. Vetterling, and B. P. Flannery. *Numerical Recipes in Fortran 77 : the art of scientific computing*, pages 413–418. Cambridge University Press, 2nd edition, 1992.

Acknowledgments

This thesis, joint between Université Pierre et Marie Curie (UPMC) and East China Normal University (ECNU), would not have been possible without the help and support of many people, whom I would like to thank here.

First of all I would like to acknowledge Alice Sinatra and Weiping Zhang for their guidance in France and in China. I'm always grateful to Weiping for leading me into the field of cold atoms and for his trust, as this is completely a new subject for me and I didn't have any experience on it before. I would like to express my gratitude to Alice, not only for giving me the opportunity to come to France, and to be able to work in this very active research group, but also for her patience and her support throughout the years. I learned a lot from numerous discussions with her. Many ideas and results of this thesis originate from these discussions. And I always remember the great time spent with her.

I would also like to thank Yvan Castin for all the discussions from which I gained some deep insights into the fundament of physics. And I believe that I will continuously benefit from them in the following years. Particularly, I thank him for proposing a numerical method to calculate the ground state of Gross-Pitaevskii equation, which I find incredibly efficient.

I'm deeply grateful to the whole atom chip group in Laboratoire Kastler Brossel, Jakob Reichel, Romain Long, Jérôme Estève, Yves Colombe, Tobias Schneider, Jürgen Volz, Tilo Steinmetz, Guilhem Dubois, Kenneth Maussang, Friedemann Reinhard, Roger Gehr, Christian Deutsch, Florian Haas, Vincent Dugrain, Benjamin Besga, and Edward Marti, for the great atmosphere and all the discussion, supports and help. Particularly, I thank Jakob for deciding to have a coffee machine in our group, and as a theoretician this is my favorite equipment in the lab.

My special thanks go to the members of the group in Munich, Philipp Treutlein, Max Riedel, Pascal Böhi, Maria Korppi, David Hunger and Stephan Camerer. The ten days I spent there are unforgettable. We discussed all day long in order to explain what had been observed from the experiment. Philipp demonstrated how to extract as much information as possible from the data

measured, which impressed me a lot. The questions raised by Max, Pascal and Philipp often pushed me to think deeper. The frequent communications via email and phone afterwards also contribute a lot to our work.

Without the support from Francis Hulin-Hubbard, our numerical simulations wouldn't have been carried out successfully. Romain Pierrat helped me a lot with the cluster machine. I would also like to thank those who provide me good working conditions, the secretaries of Institut Francilien des Atomes Froids Françoise Tarquis, Viviane Tia, as well as all the administrative staff of our lab. I also had a very enjoyable time with Mauro Antezza who shared the office with me during the last two years.

I'm grateful to the jury and the referees of the thesis, Markus Oberthaler, Li You, Claude Fabre, Isabelle Bouchoule, and Yanling Xue, for their interest of our work.

I also thank all my friends I got to know in Europe, especially many Chinese students I met in ENS, for their hospitality while working here. I would like to thank particularly Ding Fangyuan, Shan Peng, and Lü Zhengkai, for providing me kindly their apartment during the summer when the residence of ENS was closed. Likewise, I thank my colleges in ECNU who worked in office 1208, 1206, and 910 of the Science Building, for their discussion, suggestions and just being around.

I acknowledge the support of the program *Groupe des ENS-ECNU*. I also would like to mention Madame Yunhua Qian who devoted herself to this program for many years.

Finally, I would like to thank my parents for their support over the years. And I also thank my boyfriend Hang Chao for his understanding and encouragement.

List of publications

1. Yun Li, Y. Castin, and A. Sinatra, Optimum Spin Squeezing in Bose-Einstein Condensates with Particle Losses, **Phys. Rev. Lett.** 100, 210401 (2008).

2. Yun Li, Chao Hang, Lei Ma, Weiping Zhang, and Guoxiang Huang, Quantum random walks in a coherent atomic system via electromagnetically induced transparency, **J. Opt. Soc. Am. B** 25, C39 (2008).

3. Yun Li, P. Treutlein, J. Reichel, and A. Sinatra, Spin squeezing in a bimodal condensate: spatial dynamics and particle losses, **Eur. Phys. J. B** 68, 365 (2009).

4. M. F. Riedel, P. Böhi, Yun Li, T. W. Hänsch, A. Sinatra, and P. Treutlein, Atom-chip-based generation of entanglement for quantum metrology, **Nature** 464, 1170 (2010).

5. A. Sinatra, Y. Castin, Yun Li, Particle number fluctuations in a cloven trapped Bose gas at finite temperature, **Phys. Rev. A** 81, 053623 (2010).

6. K. Maussang, G. E. Marti, T. Schneider, P. Treutlein, Yun Li, A. Sinatra, R. Long, J. Estève, and J. Reichel, Enhanced and reduced atom number fluctuations in a BEC splitter, arXiv: quant-ph/1005.1922, (submitted to **Phys. Rev. Lett.**).